THÈSE DE DOCTORAT

DE L'UNIVERSITÉ PSL

Préparée à Laboratoire de Géologie de l'École normale supérieure de Paris

3D Quasi-dynamic Seismic Cycle Modeling Accelerated by Hierarchical Matrices: Role of Complex Fault Geometry

Soutenue par
Jinhui CHENG
Le 24 Septembre 2024

École doctorale nº560
Sciences de la Terre et de l'environnement et physique de l'Univers Paris

Spécialité
Sciences de la Terre

Composition du jury :

Romain JOLIVET Professeur des universités, ENS Paris	*Président*
Daniel FAULKNER Professor, Univ. Liverpool	*Rapporteur*
Yajing LIU Associate professor, McGill Univ.	*Rapporteure*
Laetitia LE POURHIET Professeur des universités, Sorbonne Université	*Examinatrice*
Manon DALAISON Maître de conférences, IPGP	*Examinatrice*
Brice LECAMPION Associate professor, EPFL	*Invité*
Michelle ALMAKARI	*Invitée*
Harsha S.BHAT Directeur de recherche, ENS Paris	*Directeur de thèse*

Abstract

Major fault systems are inherently complex in their geometrical properties, such as heterogeneous strike directions, discontinuities, and depth variations. The fault geometry can be effectively reconstructed using a variety of geologic, geodetic, and geophysical approaches; for instance, surface traces can be determined through field surveys, while depth variations can be quantified by monitoring the distribution of seismicity. Many geological and geophysical studies have shown that the geometrical complexity of fault systems in nature decisively influences the initiation, arrest, and recurrence of seismic and aseismic events. Nonplanar faults, with their multiscale roughness, introduce stress heterogeneity that determines earthquake size by controlling rupture termination. Rupture jumps across fault step-overs can significantly increase the size of earthquakes, heightening the risk and potential damage.

Therefore, to estimate earthquake magnitudes more accurately and unravel the complexities of the rupture process, it is imperative to develop an earthquake cycle model that can accurately capture the subtleties of fault geometry efficiently. However, such a refined fault model often requires huge computational costs, with problem size sometimes reaching up to a million degrees of freedom. Some previous models simplified the problem into two dimensions, unable to simultaneously account for variations in geometry from both strike and depth directions. However, in seismological observations study, Ross et al. (2020) revealed that the 3D variation in fault architecture significantly governs earthquake swarms, a critical factor overlooked in 2D models. Additionally, traditional accelerated approaches for 3D modeling are effective only for a single planar fault.

Here, we present an innovative 3D quasi-dynamic earthquake cycle model using the boundary element method accelerated by Hierarchical matrices. This approach allows us to account for elastic interactions among multiple fault segments and heterogeneous stress fields arising from nonplanar fault planes over multiple earthquake cycles. By using Hierarchical matrices, we reduce computational complexity from $O(N^2)$ to $O(N \log N)$, where N represents the number of discretized fault elements. For a fault discretized with 10^5 elements, the traditional algorithm requires 10^{10} resources. In contrast, H-matrices reduces this to 1.16×10^6.

We have cross-validated our code with analytical solutions for static cracks (such as the penny-shaped crack and cracks with a cohesive zone) and compared it with numerical solutions for planar fault dynamics from the Southern California Earthquake Center SEAS benchmark community.

We apply this method to a configuration with two parallel planar faults. For a single isolated fault under spatial uniform rate-weakening friction, regular earthquakes occur if the fault length exceeds the nucleation length. However, when considering the interaction between two faults, spatiotemporal complex slip events emerge due to the stress perturbation from the neighboring fault. Various slow slip events, as well as earthquakes having partial or full ruptures, are identified in the slip catalog. We systematically investigate how geometrical and frictional properties influence these complex seismic and aseismic sequences. By incorporating interactions from the third dimension, our model allows for a broader range of parameters that support the coexistence of earthquakes and slow slip events compared to 2D models. For moment-duration scaling of slow slip events, there has been an ongoing debate in observational studies regarding the cubic and linear scaling relations. Our numerical results suggest that this discrepancy may heavily depend on the chosen slip rate threshold for identifying slow slip events.

We further demonstrate the practical application of our model on a realistic fault system reactivated during the 2023 Kahramanmaraş doublet Turkey earthquakes. By incorporating actual fault geometry and applying a stress field smoothed by geometry, we can accurately reproduce the bilateral rupture on the Eastern Anatolian Fault and the delayed triggering on the Cardak fault. This real-world application of our model underscores its potential to enhance our understanding of seismic events and aid in earthquake risk assessment and mitigation strategies.

Remerciements

First, I would like to thank my supervisor, Harsha S. Bhat, for his scientific insights and encouragement, which have taught me how to be a research scientist.

I also thank Brice Lecampion for providing the essential computational tools for my PhD work and for giving me three opportunities to visit EPFL during my PhD. Special thanks to Carlo, Ankit, and Alexis for their helpful discussions during these visits.

I am grateful to Nadaya and Hideo, members of my thesis committee, for their excellent questions and advice, which greatly improved this thesis. I have also benefited from discussions with Jean-Philippe Avouac, Dan Faulkner, Satoshi Ide, and Pathikrit Bhattacharya.

I am grateful to my colleagues Michelle, Navid, Ankit, and Carlos for their support and suggestions. Special thanks to Michelle and Ankit for helping revise my thesis during its final stages. I also thank Marion for her suggestions in group meetings and Pierpaolo for his help with the computing cluster.

Special thanks to Dan Faulkner for his valuable discussions on lab experiments, which enriched my understanding of fluid fault interaction, and to Yajing Liu for her insightful career planning advice.

To my friends in the ENS geology lab, those I met at the 2021 Cargese summer school, and at various conferences, thank you for your support and friendship. To my friends in Paris, thank you for making my time here wonderful.

Finally, I want to thank my parents for their understanding and support, which has allowed me to pursue my dreams.

Contents

Liste des figures

List of Tables

Chapter 1

Introduction

1.1 The earthquake cycles

An earthquake occurs when there is a sudden movement between two blocks of the Earth's lithosphere. This movement is associated with the rapid release of energy accumulated in the Earth's crust. The interface along which the blocks slip is known as the fault plane. During an earthquake, energy radiates outward from the fault, causing ground shaking that can lead to significant loss of life and extensive property damage.

Grove Karl Gilbert first recognized that strain accumulates in the Earth's crust due to tectonic processes until the stress exceeds the frictional resistance along fault lines, prompting motion to relieve the strain (Gilbert, 1884). After a few decades, Harry Fielding Reid developed the more quantitative "elastic rebound theory" after analyzing displacement and geodetic data from the 1906 San Francisco earthquake (Reid, 1910).

According to this theory, the lithosphere is divided into tectonic plates that move slowly and build up stress along faults. This stress accumulates within the system until it is released. The faults remain locked until the accumulated stress overcomes this frictional resistance, releasing strain energy through earthquakes. This stress accumulating and releasing process repeats over a geologic time scale. Research indicates that the Earth's crust cannot sustain elastic strain levels much beyond 10^{-5} without failure (Kanamori, 1977). Additionally, Byerlee (1967) demonstrated that while friction along fault surfaces is generally consistent regardless of the type of rock, factors such as rock type, the presence of gouge, asperities, and fluid pressure can significantly influence the level of stress buildup before an earthquake. The released strain energy during an earthquake is utilized in heating, fracturing, and generating radiated seismic waves.

Reid's insights also led to predictive earthquake models, such as the characteristic earthquake model, which suggests that large earthquakes occur periodically and are predictable over time. This model has been observed in action along the Parkfield section of the San Andreas fault in California, which has experienced at least five earthquakes with magnitudes $M_w > 6$ since 1857, at an average recurrence interval of 22 years (Bakun and Lindh, 1985). However, due to the complex and heterogeneous nature of the Earth's crust, actual earthquake sequences are often more intricate than predicted by this model (Scholz, 2019).

In laboratory experiments, alternating locking and slipping between two surfaces in contact is known as stick-slip behavior, a recognized mechanism for earthquakes (Brace and Byerlee, 1966). The "stick" phase corresponds to the accumulation of stress, while the "slip" phase refers to the sudden release of stress. The temporal evolution of stress during an earthquake cycle includes four phases: preseismic, where stress builds up to the rupture threshold; coseismic, where the fault suddenly slips and releases energy; postseismic, where aftershocks occur, and stress is redistributed; and interseismic, where stress begins to accumulate once more until the next earthquake. This complete cycle has been observed in the Parkfield (Murray, 2006).

1.2 Fault geometrical complexities

Seismic hazard assessment is crucial for societal safety and infrastructure resilience, as it aims to quantify seismic risks for informed decision-making and preparedness. The maximum magnitude of earthquakes, influenced by the complexity of fault systems, is a critical aspect of this assessment. The geometrical complexity of fault systems in the natural environment decisively influences the initiation, propagation, and arrest of seismic events (King and Nábělek, 1985; Nakata et al., 1998; Wesnousky, 2006). With their multi-scale roughness, nonplanar faults introduce stress heterogeneity that can determine earthquake size by controlling rupture termination. Rupture jumps across fault step-overs can significantly increase the size of earthquakes, heightening the risk and potential damage. Therefore, considering fault geometry is essential for understanding fault dynamics and accurately assessing seismic hazards.

1.2.1 Refined fault structure

In order to more accurately estimate earthquake magnitudes and unravel the complexities of the rupture process, it is imperative to develop refined fault models that accurately capture the subtleties of fault geometry. The realistic fault system's geometry can be comprehensively reconstructed using various techniques. Field surveys directly observe surface ruptures, while satellite imagery offers a broad view
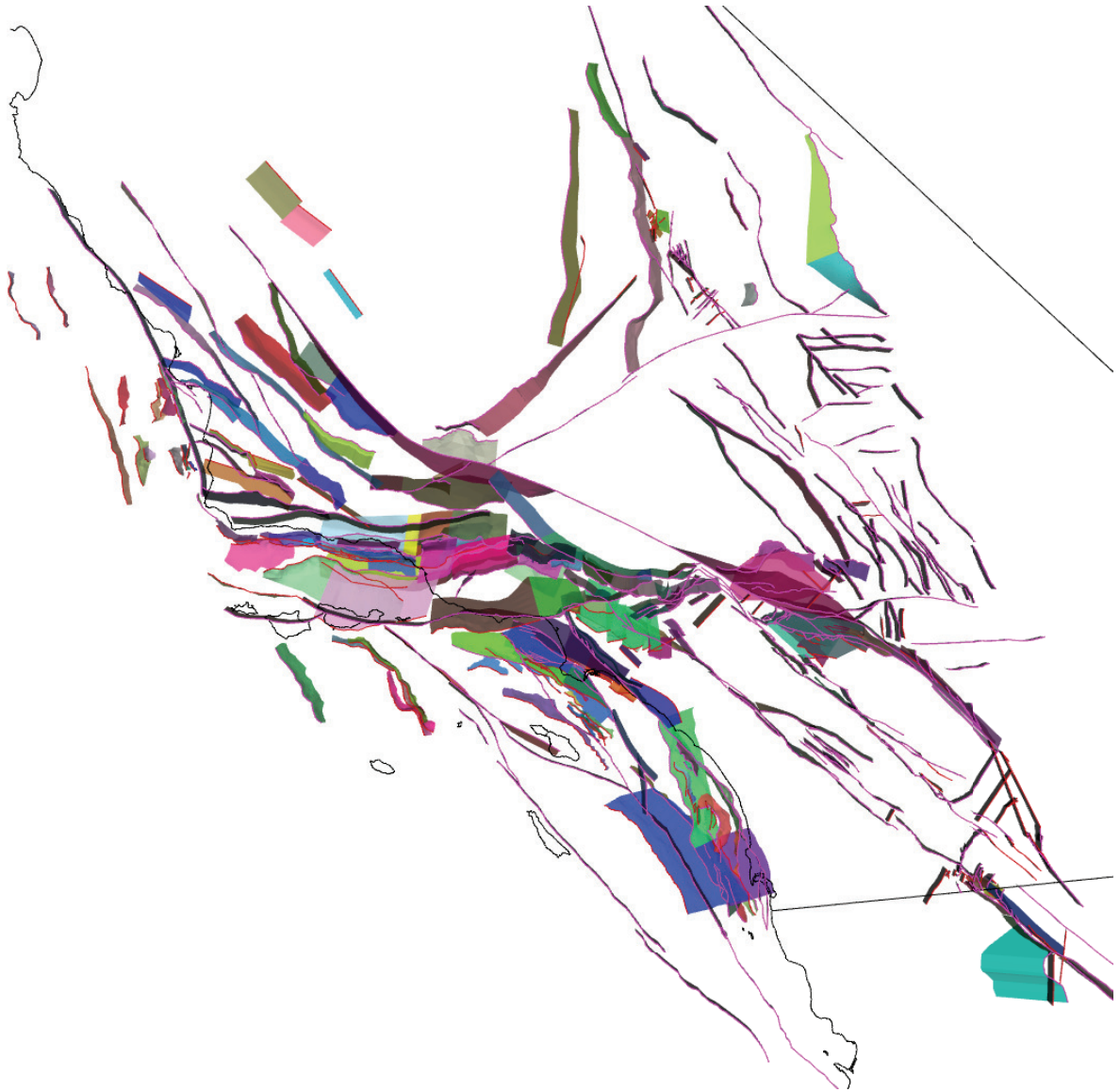
Figure 1.1: 3D representation of active faults in Southern California, plotted data from Southern California Earthquake Center (SCEC) Community Fault Model (CFM)(Plesch et al., 2007), color-coded by different fault segments.
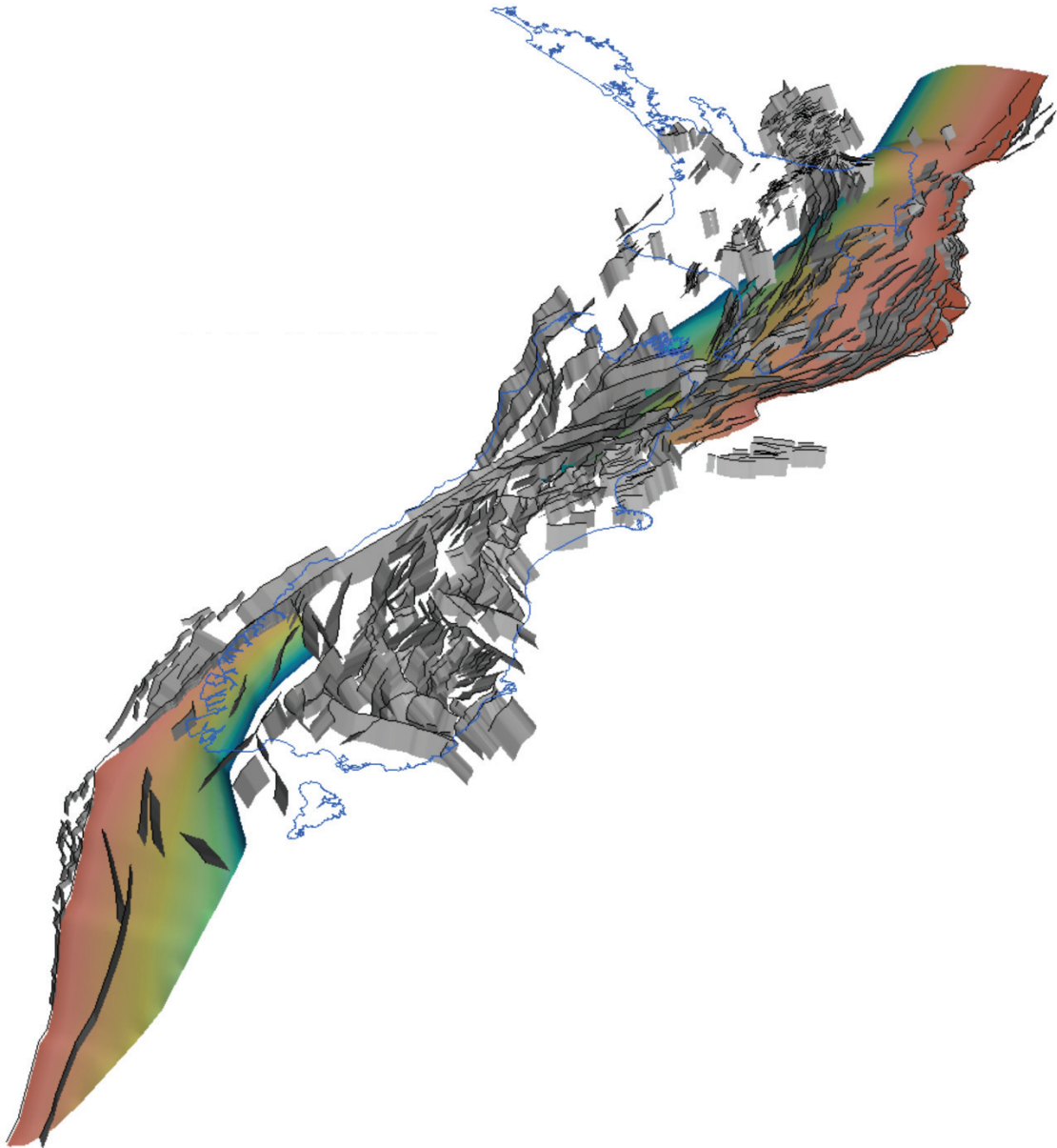
Figure 1.2: 3D representation of active fault zone in New Zealand from GNS science CFM. Color represents the depth of faults. From Seebeck et al. (2023).
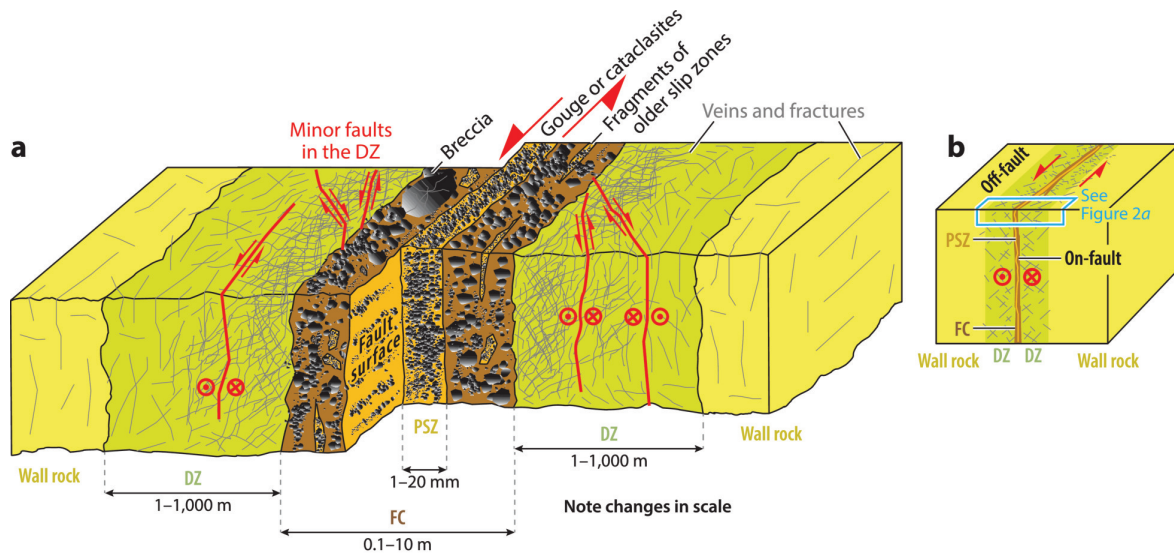
Figure 1.3: (a) A fault zone consists of a fault core, where strain is highly localized, surrounded by a fractured damage zone. The density of fractures decreases with distance from the fault core. (b) A global view of the conceptual structure of a fault zone. From Cocco et al. (2023).

of affected areas. Interferometric Synthetic Aperture Radar (InSAR) offers precise surface geometry mapping by detecting surface displacement discontinuities (Massonnet and Feigl, 1998; Bürgmann et al., 2000). Advanced technologies like 3D terrestrial laser scanning (TLS) and drones can give us detailed fault geometries (Wilkinson et al., 2010; Liu-Zeng et al., 2022). Fault depth information, which is difficult to measure from the surface, can be inferred from the distribution of seismicity with high resolution (Ross et al., 2020, 2022). Other approaches like Global Positioning System (GPS) and Interferometric Synthetic Aperture Radar (InSAR) inversion, seismic reflection profiles, and geological cross section can also help to constrain fault depth. By combining these approaches, we gain valuable insights into the geometry of fault systems. A combined approach has been successfully used in places such as Central Apennines (Faure Walker et al., 2021), Turkey (Emre et al., 2018), Southern California (Plesch et al., 2007), and New Zealand (Seebeck et al., 2023). The latter two regions, Southern California and New Zealand, are illustrated in Figure 1.1 and Figure 1.2, respectively.

The geological understanding of fault zones recognizes their inherent complexity rather than viewing them as a single fault plane. Typically, a fault zone consists of one or multiple fault cores surrounded by a fractured damage zone (Mitchell and Faulkner, 2009; Cocco et al., 2023). As illustrated in Figure 1.3, the damage zone is highly fractured, and the density of fractures decreases with distance from the fault core. Fault slips occur in the principal slip zone within the fault core, which is often simplified as a fault plane in earthquake modeling.
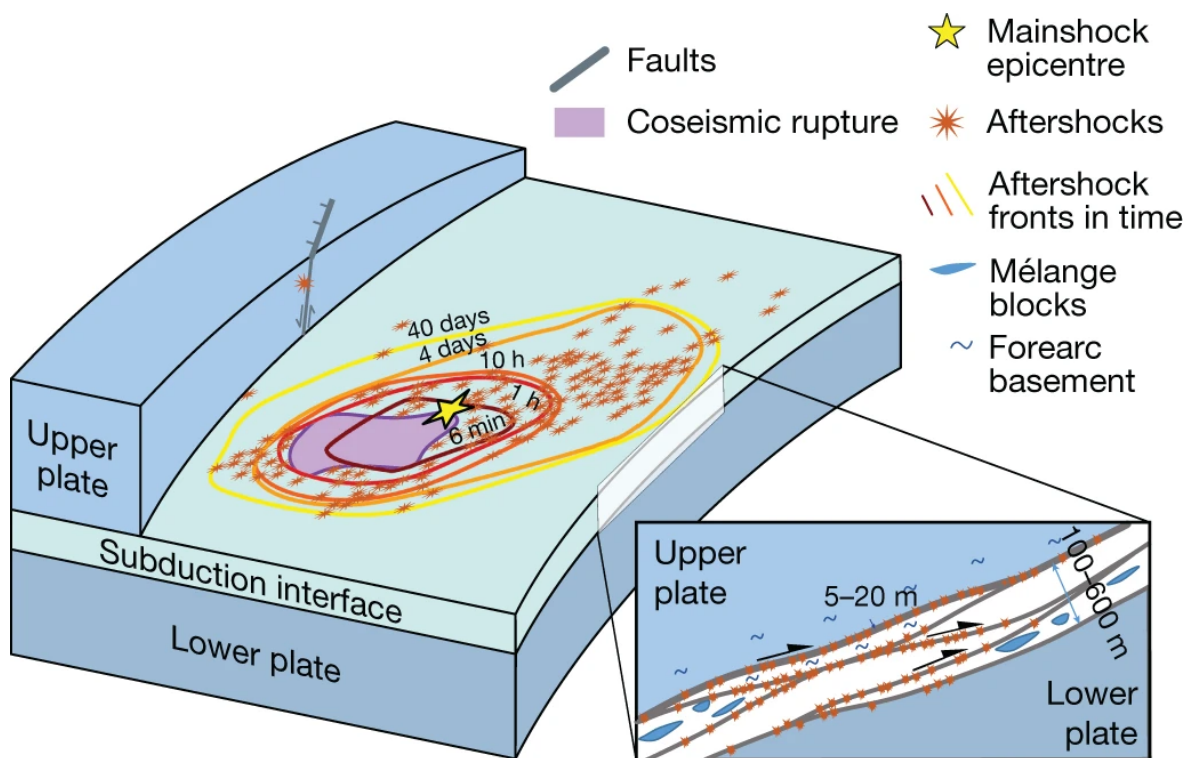
Figure 1.4: Summary of subduction zone structure inferred from seismicity. Earthquakes occur on a network of subparallel faults that are meters-thick. From Chalumeau et al. (2024).

Recent seismological studies in Ecuador have conceptualized the subduction zone as a network of meters-thick, subparallel, anastomosing faults at the plate interface (Chalumeau et al., 2024). With a double-difference algorithm, these studies have provided an unprecedentedly detailed image of the subduction interface seismicity in Ecuador, revealing that earthquakes occur on several meters-thick subparallel planes rather than a single planar fault. This geometrical complexity influences the spatiotemporal evolution of seismic and aseismic slip. Fluid diffusion cannot explain these observations, as the aftershock area expansion did not follow the fluid diffusion front. This finding is illustrated in Figure 1.4 and aligns with geological and geophysical estimates of the active plate interface thickness.

1.2.2 The role of complex fault geometry on earthquakes

Geological and geophysical investigations have highlighted the interconnected relationship between fault geometry and seismic behavior. Local geometrical features, such as bends and steps, have been studied through the analysis of surface rupture

traces from historical earthquakes (Biasi and Wesnousky, 2016, 2021). For strike-slip earthquakes, the probability of a rupture jumping across a jog is given by the formula $1.89 - 0.31 \times d_s$, where d_s is the jog width in kilometers. Large steps, defined as greater than 5 km for strike-slip faults and greater than 16 km for dip-slip faults, act as hard barriers to rupture propagation. Previous earthquakes create stress shadow barriers, which can terminate or decelerate the rupture process. Concurrently, mechanical analyses emphasizing elastic interaction underscore the pivotal role of geometry in fault mechanics (Segall and Pollard, 1980). In addition, observations from seismic events challenge the notion of isolated fault behavior. For instance, the 1992 Mw 7.3 Landers earthquake illustrated the phenomenon of multiple faults being activated simultaneously (Hauksson et al., 1993; Cohee and Beroza, 1994; Sieh et al., 1993). Similarly, the 2001 Mw 8.1 Kokoxili earthquake showed rupture propagation across two strike-slip segments via an extensional step-over, marked by a notable delay (Antolik et al., 2004). The Kunlun Fault has experienced multi-segment ruptures in over five historical earthquakes (Xu et al., 2002). The 2009 Mw 6.3 L'Aquila event in the Central Apennines, involving the L'Aquila segment and the Campotosto listric fault, serves as a case study for understanding the role of fault geometry, with the latter exhibiting dip variations with depth (Chiaraluce, 2012). The 2015 Mw7.8 Gorkha earthquake in Nepal occurred on a gently dipping section of the Main Himalayan Thrust (MHT), suggesting that fault geometry plays a primary role in controlling the magnitude and location of seismic events (Hubbard et al., 2016). In the 2016 Mw 7.8 Kaikoura earthquake, an array of faults ruptured simultaneously (Hamling et al., 2017; Cesca et al., 2017), underscoring the complex interactions within fault networks and reinforcing the idea that the structural characteristics of faults deeply influence seismic behavior.

Lee et al. (2024) investigates the impact of fault-network geometry on surface creep rates in California. The study finds that simpler fault geometries correlate with smooth fault creeping, whereas more complex geometries are prone to locking and exhibit stick-slip behavior, leading to earthquakes. Traditional models, which rely on laboratory-derived rate-and-state frictional parameters, often overlook the role of fault-system geometry. The results indicate that accommodating regional stress due to large-scale geometrical complexity is critical in determining faults' seismogenic nature. Moreover, unstable slip behavior is influenced by the entire fault system rather than just individual fault properties. See Figure 1.5. However, quantitatively determining the influence of fault geometry on slip behavior remains challenging.

a Fault-slip behaviours

Creeping

Slip

Stress

Time

Seismogenic

Slip

Stress

Time

b Rate-and-state friction law explanation for **a**

Creep

Velocity
strengthening
$a - b > 0$

+
Fault roughness?
Pore-fluid pressure?
Critical dimension?

Earthquake

Velocity
weakening
$a - b < 0$

c Fault-network-complexity explanation for **a**

Central San Andreas Fault
Small misalignment
Large creep

Large-scale geometrical locking
controls slip behaviour

Big Bend
Large misalignment
Seismogenic/locked

Figure 1.5: (a) Two different fault behaviors, creeping and seismogenic. (b) Traditional approach to explanation, rate and state friction law. (c) Fault network complexities explanation. From Lee et al. (2024).

1.3 Slip spectrum of faults in observations

1.3.1 Observation of slow slip events

It has long been recognized that earthquake-related slip accounts for only a fraction of the overall slip budgets within plate tectonics. As continuous geodetic networks have improved, researchers have discovered slow slip events (SSEs) in various tectonic environments, for example in subduction zone: Cascadia subduction zone (Hirose et al., 1999; Dragert et al., 2001), in continental strike-slip fault systems e.g., Haiyuan fault (Jolivet et al., 2013), San Andreas fault (Rousset et al., 2019). These events involve episodic, slow shear motion along faults (a few orders of magnitude faster than plate motion velocity) with no or minimal seismic activity. These events can range from small to large magnitudes, sometimes comparable to earthquakes of the same magnitude. Although SSEs generate little seismic radiation, large-magnitude events can still cause significant stress perturbations and accumulated slip on the fault, affecting its behavior. They are closely linked spatially and temporally with low-frequency earthquakes (LFEs), very low-frequency earthquakes (VLFEs), and tremors (Ito et al., 2007; Shelly et al., 2007; Michel et al., 2018), exhibiting a lower frequency of seismic radiation compared to regular earthquakes of same magnitudes. Therefore, seismological instruments can indirectly detect slow slip events by tracking the migration of tremors, repeating earthquakes, or LFEs (Kato et al., 2012; Bouchon et al., 2011; Uchida, 2019; Frank and Brodsky, 2019), which improve detection capabilities for slow slip events (Figure 1.6).

Slow slip events are ubiquitous in subduction zones and exhibit a diverse range of spatiotemporal complexities. Sometimes, they can be observed in shallow depths or below the seismogenic zone (Figure 1.7). In Nankai Trough, short-term SSEs are discovered with a duration spanning from days to weeks and 3-6 months recurrence time (Obara et al., 2004; Hirose and Obara, 2006) and long-term SSEs are observed in deep areas with around a 1-year duration and 6-year recurrence time (Ozawa et al., 2001). Shallow SSEs, locked areas, long-term SSEs, and short-term SSEs are observed from the shallow part to the down-dip extension. In Hikurangi, shallow SSEs are accompanied by microearthquakes, and deep SSEs are long-term with a duration of 2-3 months and a recurrence interval of 2 years with no tremors (Wallace and Eberhart-Phillips, 2013).

Slow slip events (SSEs) have a complex relationship with earthquakes in space and time. In the San Andreas fault, slow and fast rupture can coexist on the same section of the fault (Shelly, 2009; Veedu and Barbot, 2016). Tremor signals were observed 18 months prior to the 2004 Mw 6.0 Parkfield earthquake. There are also examples of SSEs that can occur before earthquakes (Bürgmann, 2018; Martínez-Garzón and Poli, 2024). Slow slip events can serve as a precursor to main earthquake (Bürgmann, 2018; Martínez-Garzón and Poli, 2024). The 1999 Mw7.6 Izmit earthquake was pre-
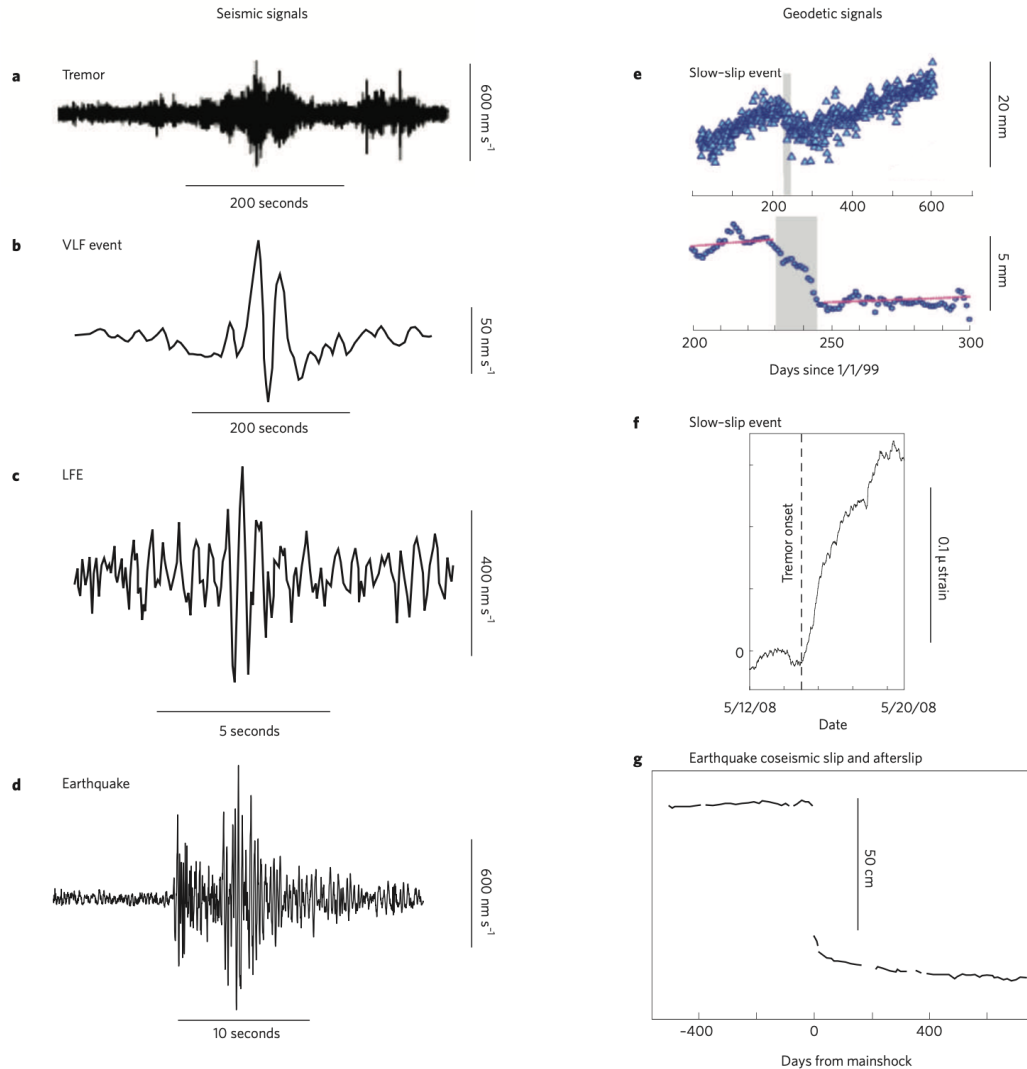
Figure 1.6: Seismic and geodetic observation of slow phenomenon and earthquakes. (a) Tremor in Japan. (b) Very low-frequency earthquake in Japan. (c) Low-frequency earthquakes from Japan. (d) Mw1.9 Earthquake in Western Washington. (e) A slow slip on Vancouver Island was observed on daily GPS. Slow slip is marked in a shaded area. (f) A slow slip in western Washington was observed from strain measurement (g) The 2001 Mw8.4 Peru earthquake was detected by GPS displacement. The large offset represents the coseismic slip. From Peng and Gomberg (2010).
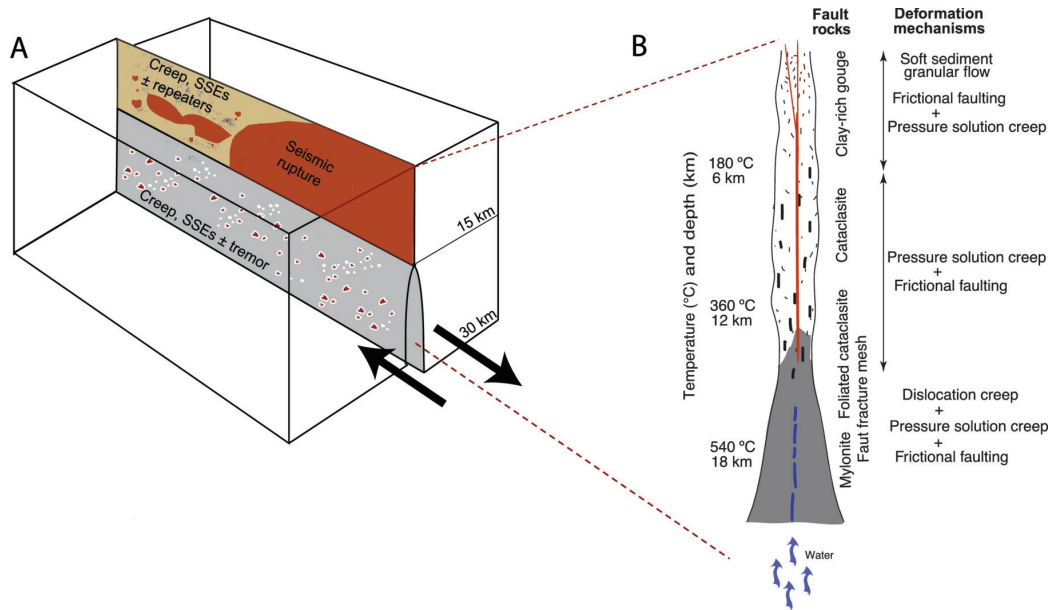
Figure 1.7: Slip behavior of strike-slip on a subduction thrust fault. (a) The schematic illustration depicts seismic and aseismic slip on the Parkfield section of the San Andreas Fault. Both slow and fast slip can occur in the lower crust, with aseismic slip predominantly occurring below the seismogenic zone. (b) A conceptual cross-section of the strike-slip fault, highlighting the depth variation of temperature, rock type, and deformation mechanisms, all of which influence different fault slip behaviors. From Bürgmann (2018).

ceded by a 44-minute slow slip (Bouchon et al., 2011). A slow slip event in Guerrero triggered the 2014 Mw 7.3 Papanoa earthquake (Radiguet et al., 2016). In the Cascadia subduction zone, GPS observations suggest that the merging of slow slip event fronts, potentially leading to a major earthquake, maybe a possible mechanism for earthquake occurrence (Bletery and Nocquet, 2020).

Earthquakes can also trigger SSEs. The 2016 Mw7.8 Kaikoura earthquake triggered a slow slip on the southern Hikurangi subduction zone (Wallace et al., 2018). The 2017 Chiapas earthquake in Mexico triggered a slow slip event on the southern San Andreas Fault, located 3000 km away from the earthquake's epicenter (Tymofyeyeva et al., 2019). SSEs can also occur periodically without earthquakes, like in Cascadia (Rogers and Dragert, 2003) and Hikurangi subduction zone (Wallace et al., 2016). The relationship between earthquakes and SSEs is still unclear and needs more studies and investigation.

Those slow phenomena significantly influence fault behavior by altering the stress field and having intricate relationships with earthquakes (Avouac, 2015; Bürgmann, 2018; Obara and Kato, 2016). Understanding slow slip events is crucial for gaining insights into earthquake mechanisms. There are several explanations for the mechanism of SSEs. SSEs can emerge from the transition of rate and state friction stability from velocity-weakening to velocity-strengthening (Liu and Rice, 2005; Rubin, 2008). Heterogeneous frictional properties, such as varying the proportions of velocity-weakening and velocity-strengthening patches, can produce stable, slow, or dynamic slip events along the fault (Skarbek et al., 2012; Luo and Ampuero, 2017; Nie and Barbot, 2021). Moreover, fault width plays a role in limiting rupture nucleation and stabilizing the faults (Liu and Rice, 2007). Mechanisms like dilatant strengthening (Segall et al., 2010; Liu and Rubin, 2010) or frictional restrengthening at high slip speeds (Kato, 2003; Shibazaki and Shimamoto, 2007; Im and Avouac, 2021) can modulate fault stabilization and instigate slow slip events. Additionally, thermal instabilities resulting from shear heating and temperature fluctuations can trigger SSEs (Wang and Barbot, 2020). Furthermore, the brittle-ductile (frictional and viscous deformation) transition (Nakata et al., 2011; Ando et al., 2023) and the presence of fluids (Bernaudin and Gueydan, 2018; Cruz-Atienza et al., 2018; Bhattacharya and Viesca, 2019; Gao and Wang, 2017) are factors that also contribute to the occurrence of slow slip events.

1.3.2 Scaling and statistical laws

Seismological observations have revealed various statistical laws governing earthquake behavior. This section introduces three universal laws: Moment-Duration scaling, Gutenberg-Richter's law, and Omori's law.

Moment-Duration Scaling

Moment-duration scaling relates the seismic moment M to the duration of the earth-quake. The seismic moment is given by:

$$M = \mu \delta A, \tag{1.1}$$

where μ is the shear modulus, δ is the slip, and A is the rupture area.

Assuming a circular crack model (Kostrov, 1964) with a constant stress drop and constant rupture velocity, the area A of the expanding circular crack is $\pi V T^2$, where V is rupture velocity, T is the duration, and the slip δ is proportional to T. Thus, the seismic moment scales as follows:

$$M \sim T^3. \tag{1.2}$$

Especially, for a 1D crack, where $A = VT$, the moment scales as $M \sim T^2$.

For pulse-like ruptures, where the rupture saturates the width of the fault, the area A is proportional to VT, and the slip δ remains constant. In this case, the moment scales as (Romanowicz and Rundle, 1993):

$$M \sim T. \tag{1.3}$$

Earthquakes typically adhere to the cubic scaling law (Kanamori and Anderson, 1975). However, the scaling relations for slow slip events (SSEs) remain a topic of debate in observational studies. See Figure 1.8. Some research supports the cubic law, such as the analysis of 10 years of GPS data from the Cascadia subduction zone (Michel et al., 2018) and the tracking of SSEs in Mexico through low-frequency earth-quakes (Frank and Brodsky, 2019). Conversely, other studies propose a linear scaling relation for slow earthquakes (Ide et al., 2007; Huang and Hawthorne, 2022; Ide and Beroza, 2023).

A limitation in current studies is the observational gap and the limited range of magnitudes covered by each study, making it challenging to resolve the scaling behavior across all earthquake sizes fully.

Guternberg-Richter law and Omori law

The Gutenberg-Richter Law is a fundamental empirical relationship that describes the frequency-magnitude distribution of earthquakes (Gutenberg and Richter, 1944). It states that in a region, the number of earthquakes N of a given magnitude M or greater is exponentially related to the magnitude:
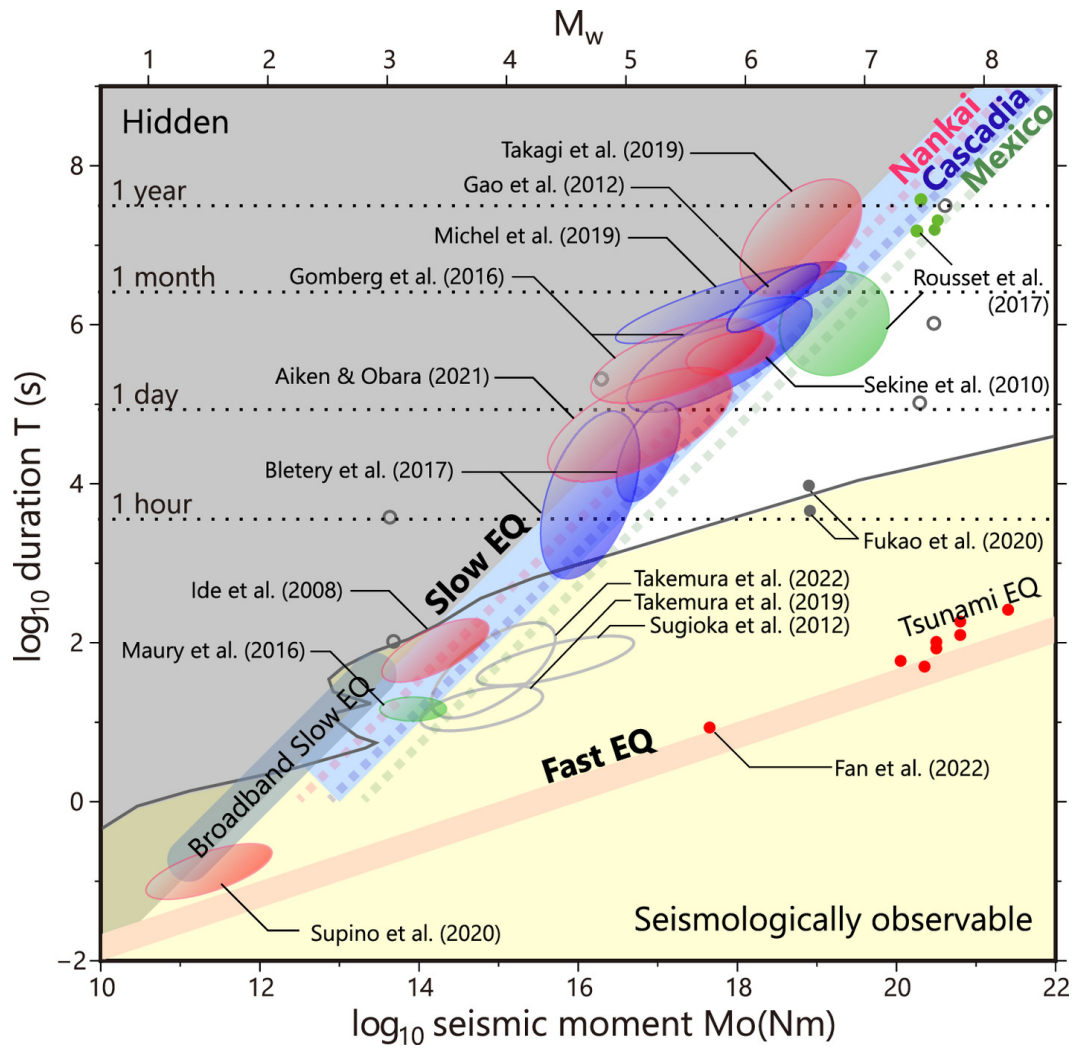
Figure 1.8: Summary of Moment-Duration scaling relations from various studies. "Hidden" indicates limitations due to detectability. The blue wide band shows the linear relationship between moment and duration. The red wide band shows the cubic relationship between moment and duration. From Ide and Beroza (2023).

$$N(M) = 10^{a-bM}, \tag{1.4}$$

where N is the number of earthquakes above a magnitude M, a is constant for a region, b is the decay exponent, and in most cases, the value is $0.9 \sim 1.5$. The statistics of slow slip events with tremors in the Cascadia subduction zone also follow the Gutenberg Richters law (Michel et al., 2019). This law indicates that small earthquakes are far more common than large ones. for seismic hazard assessments. A lower b-value suggests a higher probability of larger, potentially more damaging earthquakes. In comparison, a higher b-value suggests that the seismic activity is dominated by smaller, less destructive events.

The Omori Law describes the decay of aftershock activity following a main earthquake. It states that the rate of aftershocks N decreases over time t following the main shock (Omori, 1894; Utsu et al., 1995):

$$N(t) = \frac{k}{(c+t)^p}, \tag{1.5}$$

where t is the time from mainshock, k, c are constant and p is the decay exponent, ranging from 0.9 to 1.5 (Utsu et al., 1995). This law demonstrates that the frequency of aftershocks decreases inversely with time after the mainshock.

These laws help seismologists understand and predict earthquake behavior, contributing to hazard assessment and mitigation efforts.

1.4 Modelling of earthquakes

As discussed in the previous section, earthquakes occur when the shear stress accumulated along a fault reaches the frictional resistance at the fault interface. Understanding the mechanisms of fault friction is fundamental to comprehending the various physical processes underlying earthquakes.

1.4.1 Fault friction in earthquake physics

Historical Development of Friction Laws

The concept of friction was first explored by Leonardo da Vinci in 1493 through his experiments, though his findings were not published at the time. Approximately 200 years later, Guillaume Amonton formulated two foundational laws of friction: friction is proportional to the applied load and independent of the contact area between two surfaces. In 1785, Charles-Augustin de Coulomb expanded on this by
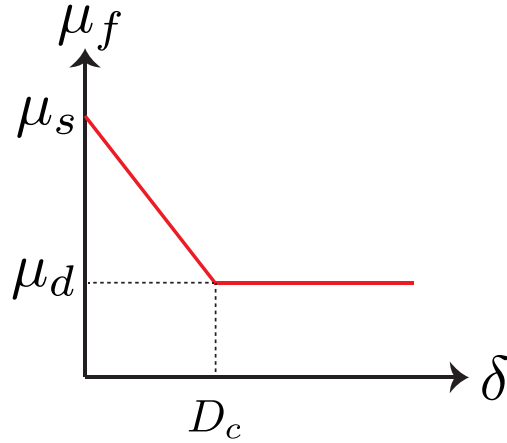
Figure 1.9: Illustration of the slip weakening friction law. After slip initiates, friction coefficient μ_f decreases as slip increases, over a characteristic slip distance D_s, until it reaches dynamic friction μ_d.

distinguishing between static and dynamic friction, noting that dynamic friction is independent of the sliding velocity and is typically lower than static friction. The Amonton-Coulomb model calculates frictional force as follows:

$$\tau = f\sigma_n, \tag{1.6}$$

where f is the friction coefficient and σ_n is the normal stress.

Rabinowicz (1958) experimentally distinguished static friction from dynamic friction and introduced the concept of critical slip distance. Later, the slip-weakening model, developed by Ida (1972), Palmer and Rice (1973), and Andrews (1976), became widely used in modeling single earthquake rupture processes. When the fault starts to slip, as the slip δ increases, the friction coefficient decreases linearly with slip over a characteristic slip distance D_c until it reaches a lower steady-state value dynamic friction μ_d and then keeps constant (Figure 1.9). The slip-weakening friction law is given as

$$\mu_f = \begin{cases} \mu_s - (\mu_s - \mu_d) \cdot \frac{\delta}{D_c} & \delta < D_c \\ \mu_d & \delta \geq D_c \end{cases}, \tag{1.7}$$

where μ_s is static friction coefficient, μ_d is dynamic friction coefficient and D_c is characteristic slip distance.

The slip-weakening law can not describe the repeating stick-slip behavior and models multiple earthquake cycles. Dieterich (1972) showed that with a slide-hold-slide experiment, the static friction increases with the logarithm of the contact time
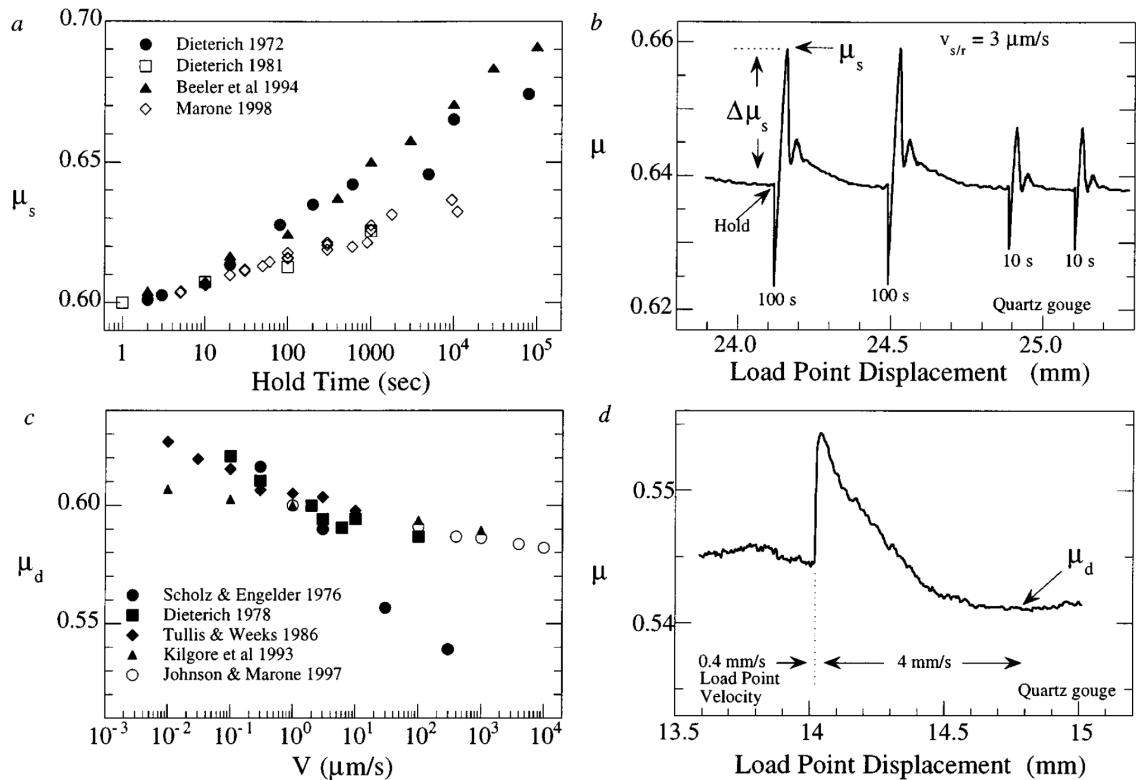
Figure 1.10: (a) The static friction coefficient increases linearly with the logarithm of hold time in slide-hold-slide experiments. Solid symbols are with bare rock; open symbols are for fault gauges. (b) Friction coefficient as a function of displacement in slide hold slide experiments (c) At a new steady state, with increasing velocity, dynamic friction shows a logarithmic dependency on slip rate. (d) Friction coefficient evolution with displacement in one velocity step experiment with direct effect and evolution effect. From Marone (1998).
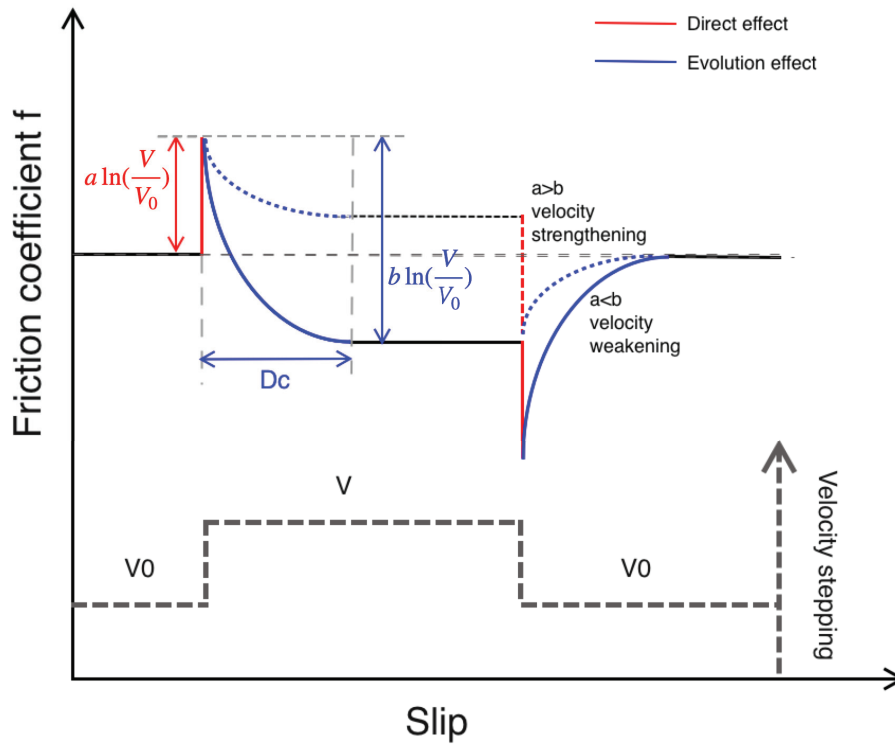
Figure 1.11: The friction coefficient evolves with displacement. When the velocity increases from V_0 to V, the friction initially rises rapidly (red curve) in a process known as the direct effect, with the increment characterized by parameter a. This is followed by a reduction over a characteristic distance D_c (blue curve), known as the evolution effect, with the decrease characterized by the parameter b. If $a > b$, the friction at higher slip rates is greater, leading to velocity strengthening and stable sliding. Conversely, if $a < b$, the friction at higher slip rates is lower, leading to velocity weakening, which favors instability to produce earthquake-like events.

(Figure 1.10a). Dieterich (1979a) performed velocity step experiments and found that the friction increases rapidly from a steady state following a velocity jump and then undergoes a relaxation over a certain distance to another steady state, as seen in Figure 1.10d. The rate and state friction (RSF) law incorporates state-dependent friction and considers healing effects, based on the above experiment evidence, which was further refined by Ruina (1983) with the introduction of the state variable θ, representing contact time of asperities (Dieterich and Kilgore, 1996). For dry friction, Dieterich (1979b); Ruina (1983) presented the following RSF law:

$$f = f_0 + a \log\left(\frac{V}{V_{ref}}\right) + b \log\left(\frac{\theta V_{ref}}{D_c}\right), \qquad (1.8)$$

where a and b are constitutive parameters that represent "direct effect" and "evolution effect" respectively (Figure 1.11 red and blue line), D_c denotes the characteristic slip

distance, f_0 is reference friction coefficient, and typical value is around 0.6, V_{ref} is the reference slip rate. The $a - b$ is influenced by factors such as temperature, rock type, and normal stress indicated by lab experiments (Blanpied et al., 1998). When $a > b$, the steady-state friction increases with increasing velocity, a phenomenon known as velocity strengthening. Conversely, when $a < b$, the steady-state friction decreases with increasing velocity, known as the velocity weakening. See Figure 1.11. Regions exhibiting velocity weakening are more prone to seismic slip, whereas regions with velocity strengthening are more likely to experience aseismic slip. In experiments of Blanpied et al. (1995), velocity weakening behavior was observed at temperatures ranging from approximately 100^oC to 300^oC, while the velocity strengthening behavior was noted at temperatures between 350^oC to 600^oC. Given the thermal gradient within the Earth, $a - b$ also varies with depth, indicating the range of the seismogenic depth. The state variable θ evolves according to the aging law (Dieterich, 1972):

$$\dot{\theta} = 1 - \frac{V\theta}{D_c}. \tag{1.9}$$

For steady state, the condition $\dot{\theta} = 0$ is satisfied. Hence, the state variable at steady state is given by $\theta_{ss} = \frac{D_c}{V}$. The steady-state friction coefficient is then $f_{ss} = f_0 + (a - b) \log \left(\frac{V}{V_{ref}} \right)$.

For the slip law (Ruina, 1983):

$$\dot{\theta} = -\frac{V\theta}{D_c} \ln \frac{V\theta}{D_c}. \tag{1.10}$$

The main difference between aging law and slip law is how they describe the evolution of state variable, which represents the history of contact conditions on fault surface. The aging law suggests that the state variable evolves with time, while the slip law suggests that the state variables evolves with slip.

In the microphysical view, RSF is also believed to be controlled by a thermally active Arrhenius process that represents the break of atomic bonds at junctions connecting the sliding surface (Rice et al., 2001; Nakatani, 2001).

The RSF law also has limitations, particularly in its ability to consistently reproduce laboratory results. The aging law within RSF reproduces time-dependent friction but shows asymmetry for increasing and decreasing velocities, which is not consistent with observed laboratory results (Blanpied et al., 1998). On the other hand, the slip law cannot reproduce time-dependent friction. However, Bhattacharya et al. (2022) demonstrated that friction is more sensitive to slip than to time. From a laboratory experiment perspective, the slip law fits the data better.

Regularized Rate and State Friction Law

The rate and state friction law is empirically derived from laboratory observations. Its logarithmic terms pose challenges in scenarios where the slip rate approaches zero or becomes negative. This is particularly relevant in earthquake simulations of complex earthquakes, where the sign convention can lead to negative slip rates, e.g., left lateral and right lateral slip.

The theoretical basis of the logarithmic form assumes that the direct velocity effect results from stress biasing of the activation energy in an Arrhenius rate process at contact junctions. This implies that forward jumps are more frequent than backward jumps.

The slip rate V can be derived from Equations 1.6 and 1.8:

$$V = V_{ref} \cdot \exp \frac{\tau}{-a\sigma'} \cdot \exp -\frac{\Psi}{a}, \qquad (1.11)$$

where $\Psi = f_0 + b \log \left(\frac{\theta V_{ref}}{D_c} \right)$ represents the current absolute offset of the friction. The term $\exp \left(\frac{\tau}{-a\sigma'} \right)$ reflects the frequency of forward microscopic jumps. However, this classic RSF model does not account for backward microscopic jumps as V approaches zero.

To address this, the regularized form of RSF adds $\exp \left(\frac{\tau}{a\sigma'} \right)$ to represent backward jumps. This refinement enables the model to handle scenarios where V is zero or negative.

The regularized form is given by:

$$V = V_{ref} \cdot (\exp \frac{\tau}{-a\sigma'} - \exp \frac{\tau}{a\sigma'}) \cdot \exp -\frac{\Psi}{a} = 2V_{ref} \cdot \sinh \frac{\tau}{-a\sigma'} \exp -\frac{\Psi}{a}. \qquad (1.12)$$

The regularized RSF law is expressed as:

$$\tau = -\sigma' \cdot a \cdot \operatorname{arcsinh} \left(\frac{V}{2V_{ref}} \exp \left(\frac{f_0 + b \log \left(V_{ref}\theta/D_c \right)}{a} \right) \right). \qquad (1.13)$$

where σ' is the effective normal stress. $\sigma' = \sigma - p$, where p is the pore pressure.

This regularized RSF law is widely used in numerical modeling of earthquake processes (Rice and Ben-Zion, 1996; Lapusta et al., 2000; Rice, 2001). It is supported by a thermally activated description of slip at frictional contacts for RSF.

Limitations and Improvements of RSF Law

The RSF law typically applies to slip rates between 10^{-9} to 10^{-3} m/s, while seismic slip rates are often above 10^{-3} m/s. At higher slip velocities, dynamic weakening effects become significant (Wibberley et al., 2008; Di Toro et al., 2011). Improvements to the RSF law include normal stress dependence (Linker and Dieterich, 1992), shear stress dependence (Nagata et al., 2012; Bhattacharya et al., 2015), and temperature dependence (Barbot, 2022). Other forms of state evolution and physics-based friction mechanisms, such as dilatancy strengthening and thermal pressurization, have been proposed (Rice, 2006; Schmitt et al., 2011; Segall and Rice, 1995).

RSF framework effectively reproduces and rationalizes a range of observed fault slip phenomena, such as earthquake nucleation (Dieterich, 1992) and aftershocks (Dieterich, 1994). The typically logarithmic time evolution of afterslip supports a logarithmic dependency of fault friction on slip rate (Avouac, 2015), consistent with RSF laws. The RSF model is widely used in numerical modeling of entire earthquake cycles (Lapusta et al., 2000), enabling the reproduction of statistical laws such as the Gutenberg-Richter law, Omori law, and Moment-Duration law based on synthetic catalogs produced from numerical models. Moreover, there are many models to derive RSF from microphysical perspectives (Chen et al., 2017; Perfettini and Molinari, 2017).

In conclusion, understanding fault friction through classic laws or improved empirical models remains fundamental in studying earthquake mechanics and predicting seismic events.

1.4.2   Modelling of earthquakes and stability analysis

In this section, I will present the different earthquake models in the RSF framework, starting with the basic spring slider model and transitioning to the continuum fault model. I will also analyze their stability.

Spring-slider model: Critical stiffness

The spring-slider model is a simple model that produces the stick-slip behaviors of earthquakes. It consists of a spring with stiffness k representing the rock medium's elasticity and a block that can slip under the force τ subjected to the spring and normal force σ subjected to the block, as seen in Figure 1.12a.

In the so-called quasi-dynamic assumption, we use radiation damping η to represent the instantaneous stress due to slip $\eta = \frac{\mu}{2C_s}$, where μ is the shear modulus and C_s is the shear wave speed (Rice, 1993). The friction is balanced with the shear
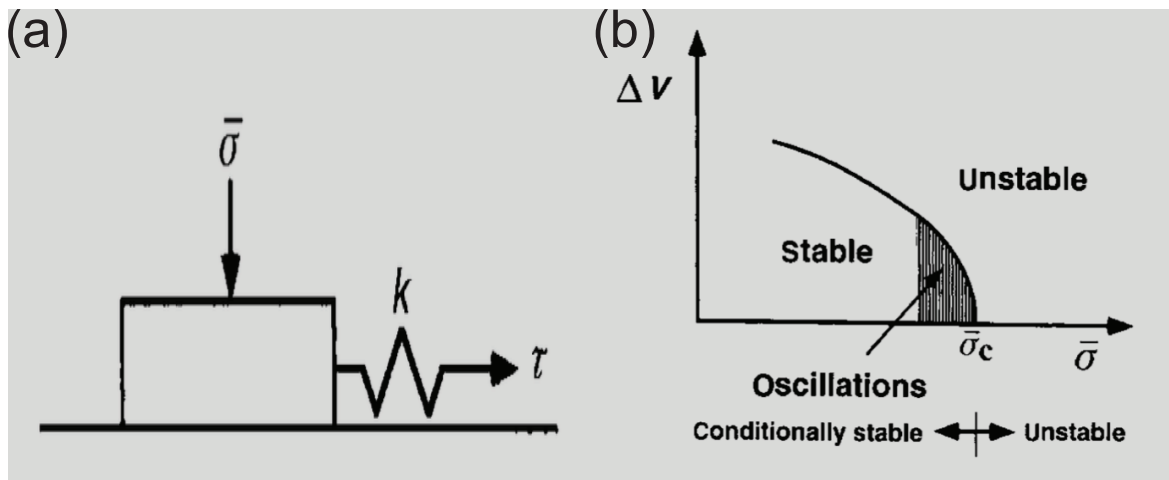
Figure 1.12: (a) In the spring-slider model, a block is connected to a spring with stiffness k and is subjected to a normal stress σ. The block undergoes slipping along a contact surface upon applying a force τ. (b) Stability phase diagram for a spring-slider model: For small perturbation of slip rate, the system becomes unstable when $\sigma > \sigma_c$ (corresponding to $k < k_c$), and remains stable when $\sigma < \sigma_c$ (corresponding to $k > k_c$). The shaded area near the boundary between the two regimes represents the oscillation regime, which indicates the transition from a stable to an unstable state. For large perturbation of slip rate, even for $\sigma < \sigma_c$ ($k > k_c$), the system can be unstable. From Scholz (1998).

traction from the spring and the radiation damping.

$$k(v^\infty t - \delta) - \eta v = \sigma_n(f_0 + a \log(\frac{V}{V_{ref}}) + b \log(\frac{\theta V_{ref}}{D_c})), \quad (1.14)$$

where k is the stiffness of the spring, v^∞ is the moving speed of the slider, δ is the slip of the slider, η is the radiation damping term, σ_n is the normal traction, f_0 is the reference friction coefficient, a and b are parameters for rate and state friction, representing the direct effect and evolution effect, respectively, V is the slip rate, θ is the state variable, V_{ref} is the reference slip rate, and D_c is the characteristic slip distance.

Ruina (1983) ignores the loading and radiation damping term and analyzes the stability of a spring slider system under small perturbations in either stress or slip rate. The critical stiffness is

$$k_c = \frac{(b-a)\sigma_n}{D_c} \quad (1.15)$$

Both aging and slip laws have the same critical stiffness when slightly above a steady state. For velocity strengthening, $a - b > 0$, the system is stable. For velocity weakening friction $a - b < 0$, under quasi-static loading, the system is stable if $k > k_c$ while the system is unstable if $k < k_c$.

Nonlinear stability analysis determines the stability of solutions under large perturbations. For aging law, $k > k_c$ is always stable (Ranjith and Rice, 1999). Slip law has a different behavior. Hopf bifurcation defines the critical points between stable and unstable regions of the system. See Figure 1.12b. Instability can occur when $k > k_c$ with large perturbation (Gu et al., 1984). Close to the boundary between stable and unstable regimes, oscillations occur. This oscillation regime was proposed as a physical mechanism for slow slip events (Liu and Rice, 2007; Leeman et al., 2016).

Continuum model: Nucleation length

The spring-slider model only has a single degree of freedom and simplifies the effects of stress interactions. In contrast, the Burridge-Knopoff model involves multiple blocks connected with springs(Burridge and Knopoff, 1967). Such a model can reproduce statistics of earthquakes, but the slip at each block is influenced only by neighboring springs and blocks. Therefore, these discrete models fail to accurately represent the complex interactions occurring in the Earth's crust (Rice, 1993). To address this limitation, Tse and Rice (1986); Rice (1992, 1993) advanced earthquake modeling by introducing a continuum approach. The governing equation is

$$\tau^\infty - \frac{\mu}{2\pi} \int_{-\infty}^{\infty} \frac{\partial s/\partial \xi}{x - \xi} d\xi - \eta v = \sigma_n(f_0 + a \log(\frac{V}{V_{ref}}) + b \log(\frac{\theta V_{ref}}{D_c})), \quad (1.16)$$

where τ^∞ is the far-field shear stress, μ is the shear modulus, $\frac{\partial s/\partial \xi}{x-\xi}$ represents the stress change at x due to the slip s at ξ, and x and ξ are points on the fault plane.

Earthquakes typically nucleate in frictional unstable regions. Nucleation lengths are an important consequence of a friction law with characteristic slip distances. Nucleation length is the critical dimension of a fault patch where stress accumulation overcomes frictional resistance, initiating a slip that can potentially propagate. It is the length of the initial zone of weakening that can grow and trigger a larger slip event. The nucleation length can be estimated from the critical stiffness of a spring-slider model. Dieterich (1992) estimated the critical stiffness of a spring-slider with the rate-and-state friction (RSF) aging law when the slip rate is well above the steady-state speed, specifically when $\frac{\theta v}{d_c} \gg 1$:

$$k_c = \frac{b\sigma_n}{D_c}. \tag{1.17}$$

The effective stiffness of an elastic crack is inversely proportional to the nucleation length and given by:

$$k = \frac{\Delta\tau}{\delta} = \frac{\mu'}{2L}, \tag{1.18}$$

where $\Delta\tau$ is the stress drop, μ' is μ for anti-plane strain or $\frac{\mu}{1-\nu}$ for plane strain, with ν being the Poisson's ratio and L is the nucleation length. Consequently, the nucleation length, known as the Dieterich length, is

$$L_b = \frac{\mu D_c}{b\sigma}. \tag{1.19}$$

This nucleation length has been verified through numerical analysis (Dieterich, 1992), indicating that the nucleation zone has a fixed length scaling with $1/b$. This is also consistent with experimental results provided by Dieterich and Kilgore (1996).

Rubin and Ampuero (2005) revealed two regimes for nucleation for the aging law. In the first regime, where $a/b < 0.3781$, as instability is approached, $v\theta/D_c$ increasing, allowing healing to be ignored. In this regime, the nucleation length is similar to the observations of Dieterich (1992). The second regime applies to $a/b > 0.3781$ values and slow loading conditions, where $v\theta/D_c$ remains quasi-constant, approaching 1. In this regime, fracture mechanics can be used to determine the critical length when the energy release rate balances with fracture energy. Numerical simulations validated this nucleation length, and it is much larger than the Dieterich length. In summary, the critical nucleation lengths in these two regimes are:

$$L_{\text{nuc}} = \begin{cases} 2 \times 1.3774 \times L_b & 0 \le a/b \le 0.3781 \\ 2 \times \frac{L_b}{\pi(1-a/b)^2} & a/b \to 1 \end{cases}. \qquad (1.20)$$

The nucleation length for slip law is significantly different from aging law due to the unidirectional growth of the nucleation slip pulse (Ampuero and Rubin, 2008).

The analysis of nucleation length above did not account for thermal or pore pressure effects, although dilatancy can stabilize slip. It is also worth noting that this nucleation length was estimated for a single flat crack under homogeneous friction.

1.4.3 Spatio-temporal complexities in earthquake cycle modeling

Observations of fault behaviors reveal a broad spectrum of slip, including various sizes of earthquakes and different slow and fast slip events, as discussed in section 1.3. Discrete fault slip models, such as the Burridge-Knopoff model, can reproduce the power-law decay of earthquake sizes. However, these models simplify the elastic interactions among neighboring blocks and cannot describe stress concentration around the crack tip. Continuum earthquake cycle simulations on single homogenous planar faults with lengths larger than L_{nuc} and proper mesh sizes produce characteristic earthquakes with regular recurrence intervals and magnitudes. This discrepancy between observations and traditional models highlights the need to explore the underlying complexities in earthquake cycles.

Rice (1993) introduced a discrete numerical system for modeling earthquake cycles by solving rate-and-state frictional slip on a computational grid with radiation damping. This model showed that complex slip behaviors and various event sizes could emerge for oversized cells compared to the nucleation lengths. Such cells can represent a geometrically disordered fault. Conversely, smaller cells can produce characteristic events. This indicated the inherent complexity of mechanical fault systems that lack a well-defined continuum limit. The quasi-static continuum method emphasized the generic complexity arising from discrete mechanical fault models (Ben-Zion and Rice, 1995). A length scale nucleation length L_b (as discussed in section 1.4.2) is adopted for rate and state friction stability to ensure numerical convergence. Therefore, a well-defined quasi-dynamic continuum model can not produce rich, complex slip behavior. The same conclusion is given with fully dynamic simulation (Rice and Ben-Zion, 1996; Ben-Zion and Rice, 1997).

Slow earthquakes emerge when the fault size is close to the critical nucleation length or near the friction stability transition (Liu and Rice, 2005, 2007), similar to the oscillation described in Scholz (1998), in the regime near $k \sim k_c$ (see Figure 1.12b). However, this contradicts the ubiquitous detection of slow slip events. Other mech-
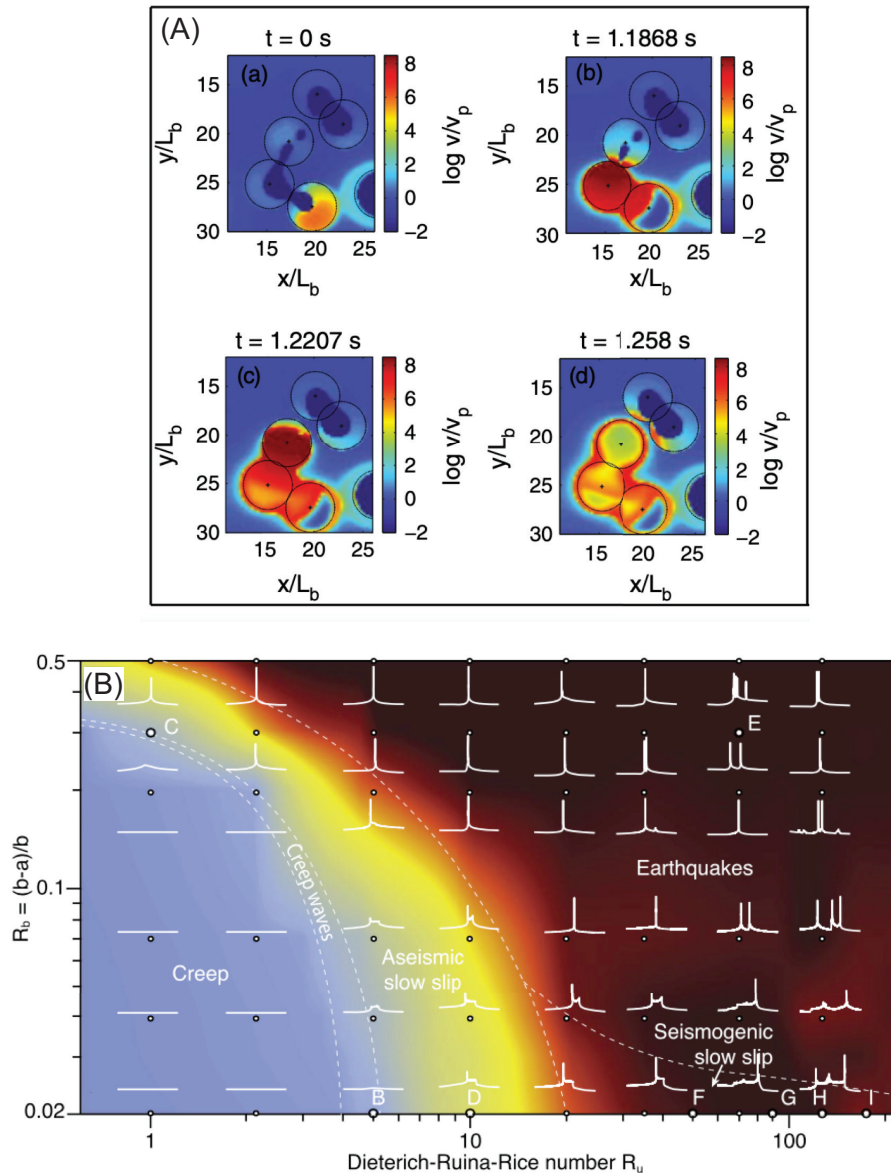
Figure 1.13: Spatio-temporal complex slip dynamics in earthquake modeling within RSF framework (a) Snapshot of slip rate on a fault model with multiple asperities. The spatially heterogeneous friction and interaction between asperities can ultimately lead to a large rupture. From Dublanchet et al. (2013). (b) The full spectrum of slip arises from varying friction conditions. Aseismic and seismogenic slow slip occur near velocity-neutral conditions. From Nie and Barbot (2021).

anisms, such as dilatancy strengthening, thermal pressurization, or pore pressure changes, need to be considered in the model to stabilize the rupture (Segall, 2010; Liu and Rice, 2007).

To effectively capture the complexities of fault behavior in continuum fault models with sizes larger than L_{nuc} under RSF law, it is crucial to consider two key types of heterogeneities: frictional and geometric complexities.

Dublanchet et al. (2013) analyzed interactions among asperities, providing insights into how frictional heterogeneity influences fault behavior and seismicity; High asperity density can lead to large events that rupture multiple asperities (Fig 1.13a). Similarly, Kato (2004) investigated the impact of the distance between asperities and the inhomogeneous spatial distribution of friction parameters on fault behavior. (Ben-Zion and Rice, 1995) demonstrated how regions with high stress drop act as barriers, contributing to power-law distributions of earthquake sizes. (Hillers et al., 2006) showed that large critical distances could act as barriers, and heterogeneous critical distances play an important role in producing complexities of slip events. Aochi and Ide (2009) examined pre-existing heterogeneity fields by varying D_c. For slow slip, Nie and Barbot (2021) explored fault dynamics across different frictional conditions, revealing variations in rupture behaviors ranging from slow to fast events depending on near-neutral weakening friction, as seen in Figure 1.13b. (Luo and Ampuero, 2018) performed a spatial heterogeneous friction fault model and demonstrated stability of a heterogeneous fault controlled by the relative length and frictional properties of strong and weak interfaces. Geometric factors such as fault roughness and nonplanarity also significantly affect earthquake cycles. Ozawa and Ando (2021) studied the role of fault roughness and subsidiary fault in reproducing aftershocks following Omori-Utsu law. Li and Liu (2016) investigated the role of nonplanar geometry on slow slip events in the Cascadia subduction zone. Additionally, Romanet et al. (2018) discussed how interactions between neighboring faults can lead to complex slip dynamics, contributing to the observed variations in slow and fast earthquakes (Figure 1.14).

Frictional and fault geometrical heterogeneity can produce a rich complexity of slip events. However, even for a single isolated fault with homogeneous friction, partial ruptures can occur for large fault lengths if the faults are loaded at a constant plate motion rate (Cattania, 2019; Erickson et al., 2011; Wu and Chen, 2014). Homogeneous planar faults can also exhibit complex rupture lengths and interevent times. On large faults, nucleation can occur near boundaries or on both sides. Due to the stress barriers generated by previous earthquakes, these sequences tend to be less characteristic, and we observe statistical features such as Omori decay and power-law distributed rupture lengths. Additionally, scale-dependent phenomena such as small repeaters and partial ruptures can be observed on these faults (Chen and Lapusta, 2009; Michel et al., 2017).

Our study aims to explore the spatio-temporal complexities in 3D earthquake
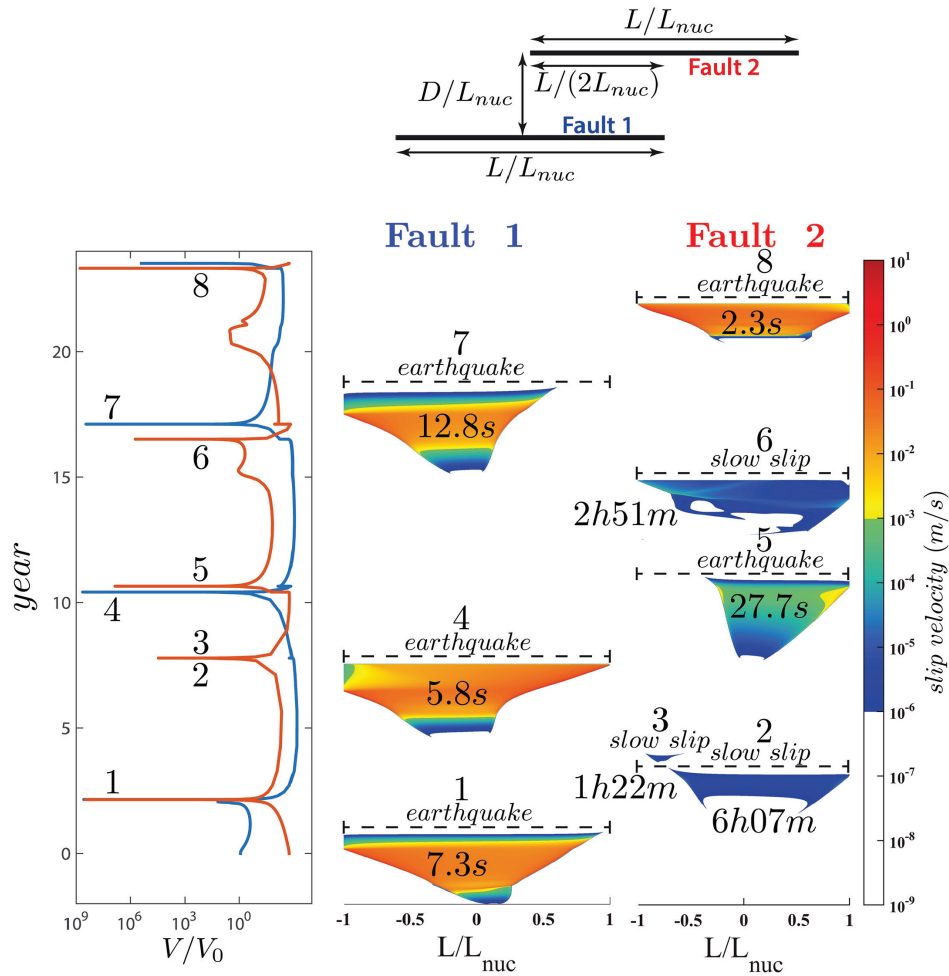
Figure 1.14: Spatio-temporal complexity of slip dynamics on a step-over in antiplane shear. The left panel shows the time evolution of slip rate on two faults, while the right panel shows the spatial distribution of slip rate on each fault. Warm colors indicate earthquake events and cool colors indicate slow slip events. In a fault system with two parallel faults under uniform friction conditions, interactions between two faults can result in both slow slip events and earthquakes. From Romanet et al. (2018).

cycle modeling, providing a comprehensive framework for understanding the intricate behaviors of complex earthquake sequences and slow and fast earthquakes. By incorporating geometric complexities and fault interaction in our numerical model, we aim to improve our understanding of slip dynamics on the various faults.

1.4.4   Numerical method to model earthquakes

Numerical modeling emerges as a powerful tool for studying the complexities of slip dynamics within fault systems. Different from statistical models of seismicity Epidemic Type Aftershock Sequences (ETAS) to represent earthquake occurrences (Ogata, 1988), physics-based numerical models offer a comprehensive understanding of earthquake processes by solving the evolution of slip on pre-existing fault systems governed by friction laws. The precise definition of the fault geometry is crucial for accurate modeling. Dynamic rupture modeling, with its accurate, fully dynamic solution, primarily focuses on the coseismic process for a single event (Aochi and Fukuyama, 2002; Duan, 2012; Ando et al., 2017; Taufiqurrahman et al., 2023), where the fault is governed by slip weakening friction. However, it only covers part of the earthquake cycle due to the high computational cost. Seismic cycle simulations are capable of modeling the entire earthquake cycle, encompassing interseismic, preslip, coseismic, and afterslip phases, over large time scales. They usually use a quasi-dynamic approach to handle the complexity of long-time scales. Wave propagation effects are neglected in favor of a radiation damping term (Rice, 1993). Various computational methods are developed for seismic cycle modeling. Boundary discretized methods, exemplified by the Boundary Element Method (BEM), focusing on fault planes and assumption of homogeneous material properties, exhibit superior computing performance and adaptability to arbitrary fault shapes (Li and Liu, 2016; Moore et al., 2019). In contrast, volume-discretized methods, including Finite Difference Method (Li et al., 2022), Finite Element Method (Liu et al., 2019), and Discontinuous Galerkin method (Uphoff et al., 2022) have their advantage for incorporating the inelastic deformation and elastic heterogeneity.

Geological faults, spanning a vast range of lengths, pose a computational challenge for seismic cycle simulations. Simulating the earthquake cycle in 3D fault networks by embedding 2D faults within a 3D medium incurs significantly higher computational costs than 2D simulations. It is a challenge for computing. However, observational studies, such as those by Ross et al. (2020), have revealed that earthquake swarm behavior is profoundly influenced by the three-dimensional fault structure, a detail overlooked by 2D models. This highlights the urgent need for an efficient tool capable of simulating 3D earthquake cycles within complex fault geometries to comprehend slip sequences accurately.

3D earthquake modeling often involves a vast number of variables, sometimes reaching up to a million degrees of freedom. While methods like the spectral bound-

ary integral element method using Fast Fourier Transform (FFT) offer efficiency, they are typically limited to single planar faults (Lapusta et al., 2000). Recent advancements, such as the work by (Romanet et al., 2021), aim to address mildly nonplanar faults, but these methods have yet to be extended to full 3D. Barbot (2021) explored the dynamics of interaction on multi-parallel faults by solving corresponding elastostatic Green's functions. The Fast Multipole Method and Hierarchical Matrices provide alternatives for efficient matrix-vector multiplication. The Fast Multipole Method, as elucidated by Greengard and Rokhlin (1987) and implemented by Thompson and Meade (2019) in earthquake cycle simulation, serves as a powerful tool for approximating far-field elements within a dense matrix, which is constructed from discretized elastic kernels. However, its application necessitates the computation of multipole expansions for various kernel types, introducing a layer of intricacy. In contrast, Hierarchical matrices present an efficient strategy for compressing dense matrices in a purely algebraic manner (Hackbusch, 2015). By selectively approximating specific far-field elements based on predefined conditions, these matrices accelerate matrix-vector multiplication in earthquake cycle modeling (Ohtani et al., 2011; Luo and Ampuero, 2018; Ozawa et al., 2022). Integrating Hierarchical Matrices in quasi-dynamic simulations substantially reduces computational complexities, scaling down from N^2 to a more manageable $N \log N$, where N is the number of elements. Nevertheless, recognizing the advantages of triangular elements over rectangular ones, especially in adapting to complex fault planes, suggests potential avenues for further refinement in earthquake modeling techniques.

1.5 Organization of this manuscript and contributions

This thesis aims to investigate the impact of complex 3D fault geometry on both seismic and aseismic slip sequences.

In Chapter 2, I introduce FASTDASH (FAult SysTem Dynamics: Accelerated Solver using H-mat), a novel quasi-dynamic earthquake sequence simulation method. This 3D model is developed to simulate slip sequences across complex fault systems, including both planar and nonplanar faults. By utilizing Hierarchical matrices, FASTDASH efficiently manages the complexities of fault networks, enabling detailed simulations within a feasible computational timeframe. To validate FASTDASH, I compare its outputs with analytical solutions for static penny-shaped cracks and benchmark them against the SCEC Sequences of Earthquakes and Aseismic Slip (SEAS) Benchmark problem BP4-QD, which addresses a 3D planar fault.

In Chapter 3, I focus on the fundamental geometry of step-over faults, examining stress interactions between two faults and the emergence of spatiotemporal

complex slip events. We quantify the influence of geometrical parameters on the distribution of slow slip events and earthquakes. Additionally, we reproduce the Moment-Duration scaling law and demonstrate its sensitivity to the slip rate threshold used to identify slow slip events.

In Chapter 4, we discuss the implications and perspectives of our research. Due to its universal applicability, our model can be extended to more realistic fault geometries. We simulated the 2023 Kahramanmaraş – Türkiye earthquakes. This highlights its ability to generate complex earthquake sequences based solely on the geometrical intricacies of fault systems without considering rheology, friction properties, or fluid interactions. This approach is particularly relevant in regions where fault geometry is well-defined. It also easily accommodates friction heterogeneity, depth-dependent normal stress, and various loading methods, highlighting the high flexibility of our code. Moreover, the development of this efficient numerical tool for studying earthquake cycles sets the stage for future work involving fluid injection.

This thesis comprises two papers to be submitted:

1. For Chapters 2: "FASTDASH: An Implementation of 3D Earthquake Cycle Simulation on Complex Fault Systems with Boundary Element Method Accelerated by H-matrices." Cheng, J., Almakari, M., Peruzzo, C., Lecampion, B., Bhat, H.S.

2. For Chapter 3: "Step-Over Fundamental Fault Geometry: The Effect of 3D Fault Interactions on Slow and Fast Earthquakes." Cheng, J., Almakari, M., Peruzzo, C., Lecampion, B., Bhat, H.S.

Regarding my contributions, in Chapter 2, I developed the quasi-dynamic earthquake sequence simulation method, implemented proper meshing techniques for complex fault geometry, and validated the model with static and dynamic solutions. I benchmarked results and determine the best numerical parameters for H-matrices and ODE solver. In Chapter 3, I conducted simulations and analyzed stress interactions and spatio-temporal slip events in step-over faults. In Chapter 4, I applied the method to a real earthquake scenario in Turkey, including setting up the model geometry, friction parameters, initial stress field, and loading conditions. I developed future research directions, explored potential applications of the model to different geological settings, and outlined the integration of fluid injection processes into the earthquake cycle simulations by combining a numerical modeling approach with laboratory experiments.

This work advances our understanding of the interplay between fault geometry and slip dynamics, offering valuable insights for future research and practical applications in earthquake modeling and hazard assessment. By integrating geological, geophysical, and mechanical perspectives, we aim to enhance the understanding of both seismic and aseismic activities within complex fault systems.

Chapter 2

Method

Avant-propos

Dans la nature, les systèmes de failles présentent des structures géométriques complexes, telles que des décrochements, des branches et des rugosités. De nombreuses études géologiques et géophysiques ont montré que la complexité géométrique des systèmes de failles dans la nature influence de manière décisive le déclenchement, l'arrêt et la récurrence des événements sismiques et asismiques. Cependant, la grande majorité des modèles de dynamique de glissement sont réalisés sur des failles planes en raison de limitations algorithmiques. Nous développons un modèle de dynamique de glissement quasi-dynamique en 3D pour surmonter cette restriction. Le calcul de la réponse élastique due au glissement est une multiplication matrice-vecteur, qui peut être accélérée par l'utilisation de matrices hiérarchiques. La complexité de calcul est réduite de l'ordre de O(N^2) à O($N \log N$). Nous validons notre code avec la solution analytique de la fissure statique et l'exercice de référence/validation SEAS du Southern California Earthquake Center.

2.1   Boundary element method

For the boundary element method (BEM), only the fault planes need to be discretized and solved under the assumption of a homogeneous and isotropic medium. The elastic equilibrium equation is

$$\nabla \cdot \sigma = 0, \qquad (2.1)$$

where σ is the stress tensor. The components σ_{ij} represent stress along x_i axis on the plane that is perpendicular with x_j. $i, j \in 1, 2, 3$ for a 3D problem. Body force and inertial terms are ignored here for simplification and quasi-dynamic assumption.

Hooke's law describes the material's constitutive law and relates strain and stress relations linearly as follows:

$$\sigma_{ij} = C_{ijkl}\epsilon_{kl}, \tag{2.2}$$

where C_{ijkl} are elastic constants, and ϵ_{kl} are strain tensor components calculated with displacement u as:

$$\epsilon_{ij} = \frac{1}{2}\left(\frac{\partial u_i}{\partial x_j} + \frac{\partial u_j}{\partial x_i}\right). \tag{2.3}$$

To derive the BEM formulation for elastic interactions, we need to introduce the representation theorem, which is derived from the reciprocity theorem. If we know the green function of the medium, we can calculate the elastic displacement at any point inside the volume as follows,

$$u_i(\mathbf{x}) = \int_{\Sigma} K_{ij}^U(\mathbf{x}, \xi)t_j(\xi)d\Sigma - \int_{\Sigma} K_{ij}^T(\mathbf{x}, \xi)u_j(\xi)d\Sigma, \tag{2.4}$$

where K^U and K^T are the displacements and the traction kernels in Kelvin's fundamental solution individually (Bonnet, 1999; Mogilevskaya, 2014).

Considering two internal surfaces Σ^+ and Σ^- that represent the upper and lower side of a fault plane, the representation theorem gives the displacement at x_* on the boundary by taking the limit from integration:

$$u_i(\mathbf{x}_*) = \lim_{x \to x_*} \int_{\Sigma^-+\Sigma^+} K_{ij}^U(\mathbf{x}, \xi)t_j(\xi)d\Sigma - \lim_{x \to x_*} \int_{\Sigma^-+\Sigma^+} K_{ij}^T(\mathbf{x}, \xi)u_j(\xi)d\Sigma, \tag{2.5}$$

where displacement u and t are the displacement field and traction field, respectively.

For a crack problem, we consider two planes merged to one surface $\Sigma = \Sigma^-+\Sigma^+$. We define the displacement discontinuity $\Delta u = u^- - u^+$ and traction $t_i^+ + t_i^- = 0$ due to continuity of traction.

Then, the displacement can be simplified as follows:

$$u_i(\mathbf{x}) = \int_{\Sigma} K_{ij}^T(\mathbf{x}, \xi)\Delta u_j(\xi)d\xi. \tag{2.6}$$

We substitute into Hooke's law Equation 2.2, and the traction integral becomes

$$T_i(\mathbf{x}) = \int_{\Sigma} H_{ij}(\mathbf{x}, \xi)\Delta u_j(\xi)d\xi, \tag{2.7}$$

where traction $\mathbf{T} = (T_1, T_2, T_3)$, and H is one of the hypersingular kernels in Kelvin solution (Bonnet, 1999; Mogilevskaya, 2014). See it in Figure 2.1a.
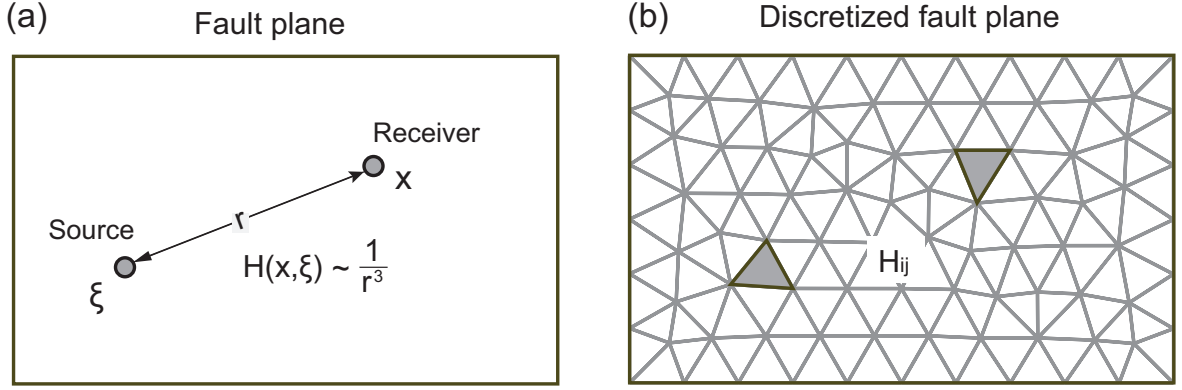
Figure 2.1: Schematic diagram of (a) boundary integral equation for traction-slip relations (b) discretized form for traction-slip relations.

Until now, we had an analytical solution for displacement and traction due to dislocation over the crack surface. For the numerical implementation, the fault plane needs to be discretized into planar triangular or rectangular elements. Our method allows both triangular and rectangular elements, but triangular elements are more flexible for nonplanar geometry.

In the simple case, the slip is defined uniformly over each element. Traction is given at the centroid and is the summation of the linear systems over all elements:

$$T_i(\mathbf{x}) = \sum_{q=1}^{N} \int_{\Sigma^q} H_{ij}(\mathbf{x}, \xi) d\xi \Delta u_j^q, \tag{2.8}$$

where q is the index of each element, u_j^q is the displacement in j direction for q^{th} element, Σ_q is the surface for q^{th} element. See it in Figure 2.1b.

In Equation 2.8, H_{ij} is a hyper-singular integral over element q. The traction kernel is proportional to r^{-3}, where r is the distance between source and receiver (Hills et al., 2013). The singularity comes out when the source and receiver points are overlapped. Numerical calculation of the integral is unstable in the vicinity of singularities. There are different techniques to remove the singularity. For a 2D kernel, Tada and Yamashita (1997) integral by parts and address by Cauchy principal values. For a 3D problem, to solve elastic fields induced by a triangular dislocation loop (which is the discontinuity displacement method), we use explicit formulae for the 3D hyper-singular integral equation of elastostatics from Fata (2011). In Fata (2011), the surface integral is simplified to contour integral with Stokes theorem, and the hypersingular term is reduced to a weakly singular term that can be evaluated in terms of Cauchy principle values. The explicit formula is written in recursive format with regard to each edge of the triangles, which makes it easy to implement numerically.

Finally, the elastic traction in discretized form has a matrix-vector format:

$$T_i = \sum_{j=1}^{N} A_{ij} \Delta u_j, \tag{2.9}$$

where T_i is the i component of traction, contributed by each components of Δu individually. j is the index of the element. A is a densely populated matrix of size $N \times N$. Each entry of that matrix is an integral equation over the corresponding element.

2.2   Governing equation

The numerical modeling of the earthquake cycle for BEM is governed by the force equilibrium equation on the discretized fault plane. On each element, the total traction on the fault is balanced with force resistance. However, this leads to unbounded traction. We use quasi-dynamic BEM, the inertial term is removed and approximated by a radiation damping term (Rice, 1993):

$$\boldsymbol{\tau^{rad}} = -\frac{\mu}{2C_s} \boldsymbol{V}, \tag{2.10}$$

where $\boldsymbol{V}$ is (V_s, V_d), slip rate in shear and dip direction. Only slip rate in the fault plane is allowed with no opening slip in our model. μ is shear modulus and C_s is shear wave velocity.

Total traction includes three ingredients, elastic shear traction τ^{el}, far field loading τ^{load} and radiation damping τ^{rad}. For elastic shear traction, it can be recast to a matrix-vector format in BEM (as discussed in section 2.1). For far-field loading, we allow constant plate rate loading (backslip approach) or stress rate loading in the same principle directions as background stress. For radiation damping, it only exists in the plane constructed by the fault plane.

The force resistance τ^f is normal traction T_n (compression is negative and extension is positive) times friction coefficient f:

$$\tau^f = -T_n * f. \tag{2.11}$$

We assume the fault is governed by rate and state friction (RSF) law (Dieterich, 1979a; Ruina, 1983), and regularized form of friction is (Lapusta et al., 2000; Rice et al., 2001)

$$f = a \cdot arcsinh(\frac{V}{2 * V_{ref}} \exp \frac{f_0 + b \log (V_{ref}\theta/Dc)}{a}), \tag{2.12}$$

where a and b are friction parameters, D_c is characteristic slip distance, V_{ref} is the reference slip rate, f_0 is the reference friction.

With aging law to describe the evolution of state variables θ:

$$\frac{d\theta}{dt} = 1 - \frac{V\theta}{D_c}. \tag{2.13}$$

Rake angle λ is defined as the angle between the slip vector and the strike vector. We assume that the slip vector is parallel with the traction vector, and we allow rake angle rotation. The 3D force equilibrium equation in a fault-based coordinate system can be written as:

$$\tau^f \cos\lambda = \tau_s^{el} + \tau_s^{load} + \tau_s^{rad} \qquad \text{for direction } \vec{s} \tag{2.14}$$

$$\tau^f \sin\lambda = \tau_d^{el} + \tau_d^{load} + \tau_d^{rad} \qquad \text{for direction } \vec{d} \tag{2.15}$$

$$T_n = \tau_n^{el} + \tau_n^{load} \qquad \text{for direction } \vec{n}. \tag{2.16}$$

By coupling Equation 2.14, Equation 2.15 and Equation 2.16 with rate and state friction law and state variable evolution from Equation 2.12 and Equation 2.13, we have five equations to describe the physical variables' changes on the fault with time in order to ensure the satisfaction of the force equilibrium. We differentiate each of them with time and get a set of explicit ordinary differential equations (ODEs):

$$\left\{ \frac{d\mathbf{y}}{dt} \right\} = [M] \{\mathbf{y}\}, \tag{2.17}$$

where $\mathbf{y} = (V, \lambda, T_n, \tau, \theta)$, and $M \in \mathbb{R}^{5\times5}$. Please refer to Appendix 2.A for more details on the derivation of the ODE system.

There are 5 unknowns in this system, including slip rate, rake angle, normal traction, shear traction, and state variable. We solve this system for every element with the Runge-Kutta45 method (Feblberg, 1969; Winkler, 1993). Runge-Kutta45 is an adaptive time-stepping method, and the time step is error-controlled, given by the relative difference between fifth-order and fourth-order Runge-Kutta solutions. For coseismic phases, time steps can be very small in order to capture the rapidly changing slip rate and traction in the solution. More details on the implementation and verification of Runge-Kutta45 are shown in section 2.4.4.

2.3 Hierarchical matrices

For problems that can be solved with a two-dimensional model, the computational cost increases rapidly once the third dimension is added. Here, we give an example. To simulate the fault system for the 2023 Turkey earthquakes presented in Chapter 3, 10^3 elements are required for a 2D simulation, while 10^5 elements are required for a 3D model. More importantly, the most time-consuming part is the calculation of elastic traction, which is a matrix-vector multiplication in BEM (see Equation 2.9) that needs to be called at every time iteration. The computational complexity of the classic matrix-vector product is $O(N^2)$. Large model-size simulations require greater memory size and computational time. Therefore, it is necessary to use efficient computational tools to accelerate the 3D earthquake sequence simulator.

The off-diagonal elements of the matrix **A** in Equation 2.9 decay quickly with r^{-3}, where r is the distance between the source and receiver. Thanks to the decaying nature, we can use Hierarchical Matrices (H-matrices) to accelerate the simulation. The idea of H-matrices is to decompose the dense matrix into sub-blocks and approximate some of the blocks that satisfy the admissibility condition. For the elements close to the diagonal blocks, we use full rank. For far off-diagonal blocks, we can approximate by using low-rank approximation.

The H-matrices we use is a C++ library Boundary InteGral equations With HierArchical Matrix (BigWham) (Ciardo et al., 2020; Sáez, 2023). For a given fault geometry, H-matrices only need to be constructed once before the time step. For every time step, we apply H-matrices vector multiplication to compute the elastic traction in Equation 2.9.

H-matrices is an efficient computation tool that can reduce memory storage for the dense matrix and reduce the computational complexity of matrix-vector multiplication from $O(N^2)$ to $O(NlogN)$.

2.3.1 Structure of H-matrices

To create the compressed representation of a dense matrix, we first construct a binary cluster tree T_I based on the partition of the domain, as shown in Figure 2.2a and Figure 2.2b. For the root of the cluster tree I, all the elements are in a box B, and then each box is divided by a separation plane recursively. Each node of the cluster tree T_I is defined by the sub-domain partition. The stopping criterion for subdivision is the number of elements in the sub-domain is less than the number of leaves N_{leaves}, which corresponds to a leaf of the cluster tree.

To construct the H-matrices, we decompose the dense matrix into sub-blocks recursively by going through the cluster trees. Each node in the cluster trees contains

a pair of row clusters τ and column clusters σ, which determines a block of matrix $\boldsymbol{A}$, as seen in Figure 2.2c and Figure 2.2d. After each subdivision, we examine the sub-blocks for admissibility conditions. If the sub-blocks meet the criteria for low-rank approximation, the subdivision stops; otherwise, it continues further subdivision until the sub-blocks are formed by the leaves of the cluster tree.

The admissibility condition is to determine if the blocks can be approximated or not,

$$\min(diam(B_\tau, B_\sigma)) \leq \eta \cdot dist(B_\tau, B_\sigma), \tag{2.18}$$

where $diam$ is the diameter of the cluster, and $dist$ is the distance between the row and column clusters, as seen in Figure 2.2c. This condition indicates that relatively distant clusters can be approximated, but relatively close clusters cannot. H-matrices property η can control the strictness of the admissibility condition. For larger η, more clusters are defined as distant clusters that can be approximated, and the calculation will be less accurate but more rapid. For elastic kernels, usually, $\eta = 3$ yields the best performance but varies for different geometries.

Finally, we show one example of H-matrices structure for a problem with 36,000 elements in Figure 2.2e.

2.3.2 Adaptive cross approximation

For the submatrix A_{LRA} that satisfies the admissibility condition, we compress with rank approximation.

Singular value decomposition is the optimal low-rank approximation for the Frobenius norm. However, it requires assembling the complete entries. Thus, the computation cost is expensive, in the order of $O(max(M, N)min^2(M, N))$.

Adaptive Cross Approximation (ACA) is an iterative method that gives a quasi-optimal low-rank approximation. The matrix $A_{LRA} = S_k + R_k$, where S_k is the k-rank approximation and R_k is the residual. At each step k, the outer product of pivot row u_k and column v_k is calculated and subtracted from the residual R_k and added to the approximation S_k. Fully-pivoted ACA requires the assembly of the entire matrix, but Partially-Pivoted ACA assembles one row or column per iteration. The stopping criterion is

$$||u_{k+1}||_2||v_{k+1}||_2 \leq \epsilon_{ACA}||S_{k+1}||_F, \tag{2.19}$$

where ϵ_{ACA} controls the accuracy of the low-rank approximation.

In this way, we decompose the submatrix A_{LRA} into sum of vector multiplication

(a) Division of domain

(b) Cluster tree of T_I

Matrix   A

Block cluster $T_{I \times I}$

Bounding box

(c) Bounding box

(d) Corresponding block in matrix

(e) Example of H matrices structure for SEAS BP4-QD benchmark
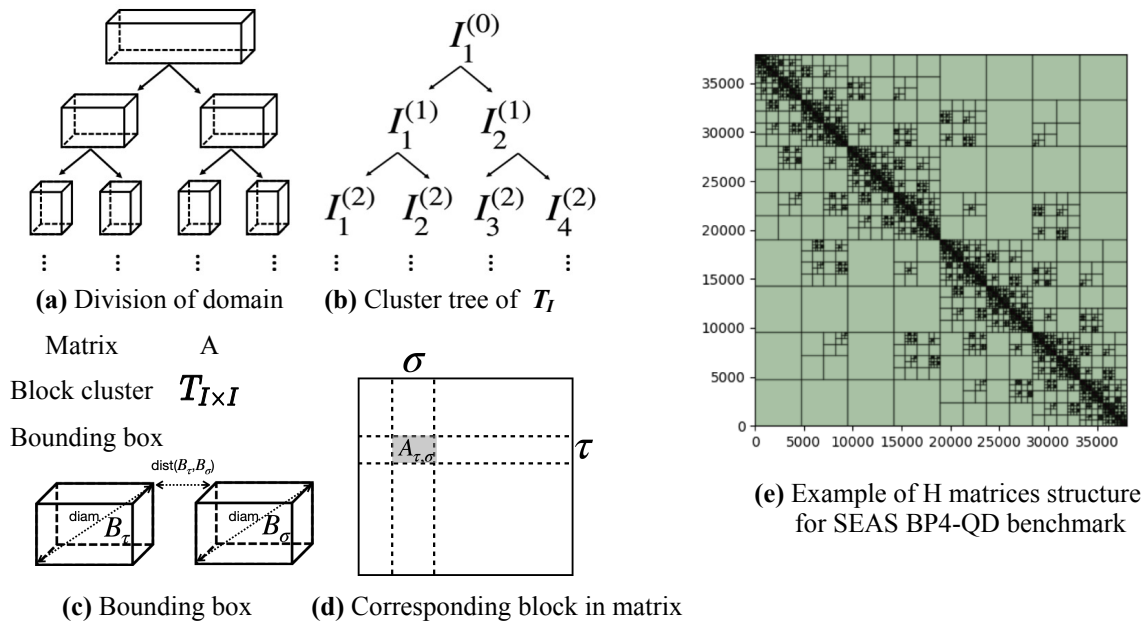
Figure 2.2: Illustration of H matrices structure (a) Division of domain (b) Cluster tree of T_I (c) Initial matrix $\boldsymbol{A}$ can be written as a block cluster representation $T_{I \times I}$, and each cluster is enclosed into a bounding box B. For cluster τ and σ, the distance between the two and each diameter are shown in the dashed lines with arrows (d) The cluster pair (τ, σ) represents the row and column cluster, and define the corresponding block in matrix.
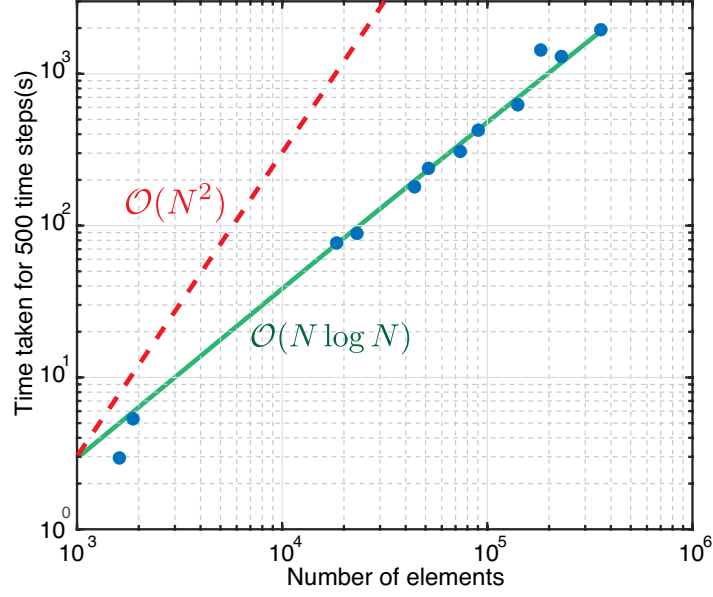
Figure 2.3: Computational complexities

for k-rank approximation:

$$A_{LRA} \approx A^k = \sum_{n=1}^{k} u_n v_n^T \tag{2.20}$$

$$A_{ij}^k = \sum_{n=1}^{k} u_{ni} v_{nj}^T. \tag{2.21}$$

For the submatrices with low-rank approximation, the matrix-vector multiplication can be performed as:

$$\sum_{j=1}^{N} A_{ij} \Delta u_j = \sum_{j=1}^{N} \sum_{n=1}^{k} u_{ni} v_{nj}^T \Delta u_j = \sum_{n=1}^{k} u_{ni} \left(\sum_{j=1}^{N} v_{nj}^T \Delta u_j \right). \tag{2.22}$$

The computation for the product of matrix and vector is $O(MN)$, and the submatrices with ACA are reduced to $O(k(M+N))$. For the submatrices that do not pass the admissibility check, we calculate the traction using the regular method. The total traction vector is the summation of all the submatrix-wise matrix-vector multiplication.

The total computational complexities theoretically are $O(NlogN)$ and practically are shown in Figure 2.3. For a simulation that require one day, with H-matrices acceleration, it will finish in one hour.

2.4 Implementation

FASTDASH is written in Python and can efficiently solve slip dynamics on complex fault systems. The H-matrices library we used (BigWham) is multithreaded and implemented in C++. We present the workflow of this method in Figure 2.4. Before delving into this model, we first introduce the coordinate system and sign convention in section 2.4.1. We discretize the natural fault system into triangular or rectangular elements, as shown in section 2.4.2. The fault is governed by rate and state friction law, as we discussed in section 2.2. Before the time step, we assign initial conditions and loading conditions, shown in section 2.4.3. We present the ODE solver Runge-Kutta45 in FASTDASH, and we verified the results with different models in section 2.4.4. In section 2.4.5, we describe how to choose the numerical parameters. In the end, we have post-processing for the slip catalog, seen in section 2.4.6.

2.4.1 Coordinate system and sign convention

There are three coordinate systems in this method: global system (x_1, x_2, x_3), local system (e_1, e_2, e_3), and fault system (s, d, n). For a global coordinate system, (x_1, x_2, x_3) is a right-handed coordinate system, where the surface of the Earth is in the x_1 x_2 plane, and the x_3 axis points vertically upwards from the Earth's surface (Figure 2.5a). We take the real fault geometry from nature and discretize it in the global systems with triangular (or rectangular) elements by using an automatic mesh generator, CUBIT, or GMSH. The mesh file with fault geometry information is written in the global system. H-matrices Library (BigWham) works on local coordinate system (e_1, e_2, e_3), which is based on the triangle elements (Fata, 2011). There are three nodes $\mathbf{y}^1, \mathbf{y}^2, \mathbf{y}^3$ in one triangle element, and here it requires the connectivity of the elements is anti-clockwise. The orthogonal basis of the local coordinate system is:

$$\mathbf{e_1} = \frac{\mathbf{y}^2 - \mathbf{y}^1}{||\mathbf{y}^2 - \mathbf{y}^1||}, \vec{e_t} = \mathbf{y}^3 - \mathbf{y}^1, \mathbf{e_3} = \frac{\mathbf{e_1} \times \vec{e_t}}{||\mathbf{e_1} \times \mathbf{e_t}||}, \mathbf{e_2} = \mathbf{e_3} \times \mathbf{e_1}, \qquad (2.23)$$

as seen in Figure 2.5b. y^1, y^2, y^3 are three nodes of the triangles in anti-clockwise direction. $\vec{\xi}$ is the slip vector, and the rake angle in the local system is α, defined as the angle between $\mathbf{e}_1$ and $\vec{\xi}$.

A fault-based system is the most intuitive system for analyzing results. The strike direction $\mathbf{s}$ is chosen along the surface trace of the fault plane and points towards the slip direction for a right lateral fault. $\mathbf{d}$ is perpendicular with $\mathbf{s}$ and $\mathbf{n}$, and points towards slip direction for a normal fault. $\mathbf{n}$ is the unit normal to the fault plane directed from the negative surface to the positive surface. Rake angle λ is the angle from the strike direction to the slip vector, where anti-clockwise is positive. In

FASTDASH
FAult SysTem Dynamics: Accelerated Solver using H-mat
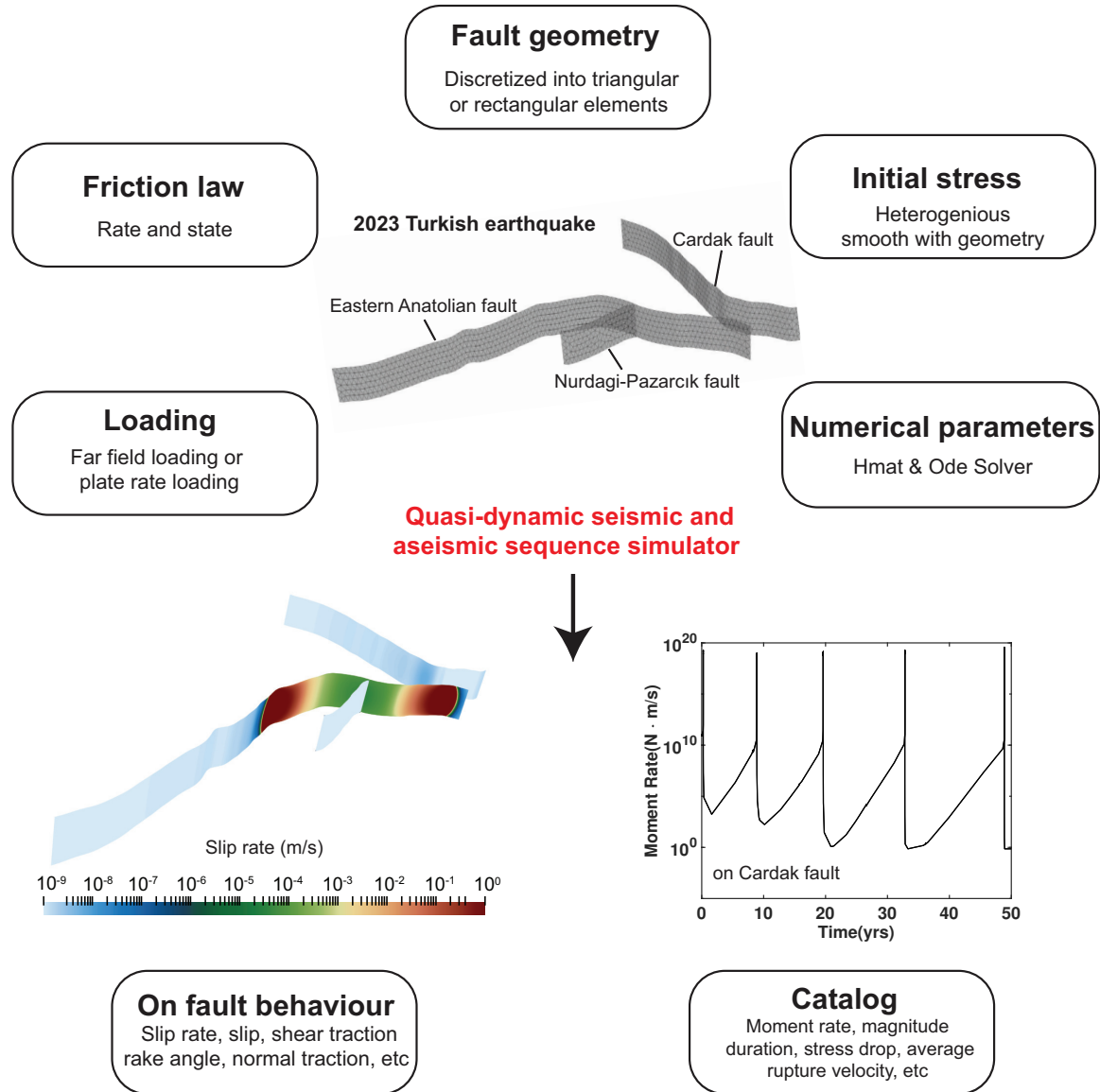
Figure 2.4: Workflow of FASTDASH.
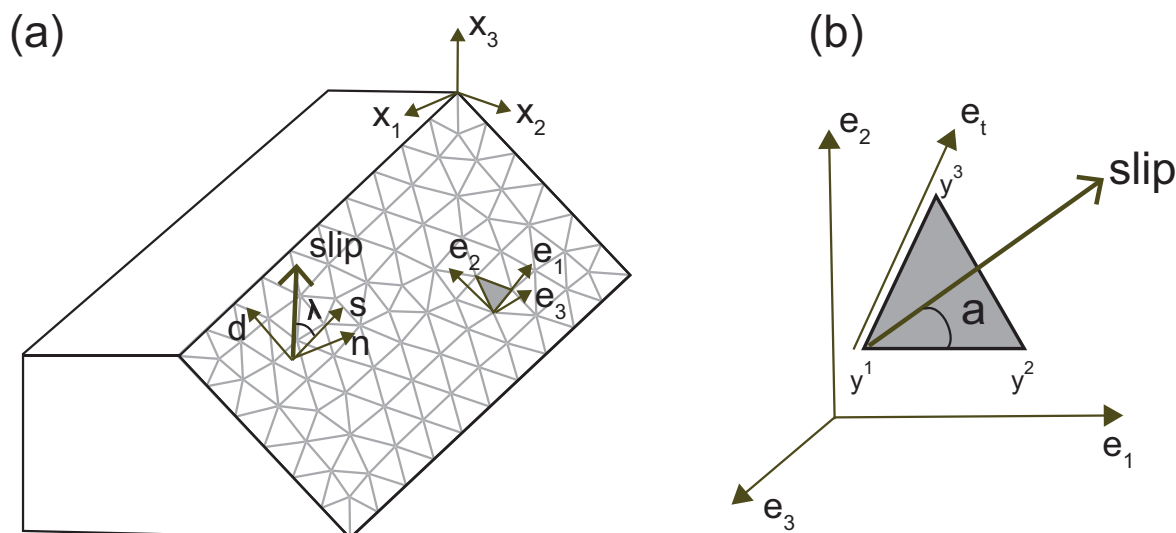
Figure 2.5: (a) Global coordinate system, fault coordinate system, and local coordinate system (b) Local coordinate system

.

FASTDASH, all the analysis is based on the negative surface, which is the footwall for a dipping fault. The slip vector $\vec{\xi} = u^- - u^+$ is taken as the displacement of the footwall relative to the hanging wall.

The ordinary differential equation system is written in a local coordinate system, and it is easy to implement BigWham to calculate the elastic traction. To assign the initial conditions of slip rate and traction, we need to transform the coordinates from the fault-based system to the local system. To output the slip rate and traction, we need to transform from the local system to the fault-based system.

The fault-based system and the local system are both element-wise and spatially varying coordinate systems, especially for nonplanar faults. For the fault-based system and the local system, $\mathbf{n}$ is equal to $\mathbf{e_3}$, which will simplify the 3D coordinate transformation to a 2D coordinate transformation. The details for the coordinate transformation are given in Appendix 2.B (Equation 2.54, Equation 2.55, Equation 2.61 and Equation 2.62).

2.4.2 Mesh generation

For complex fault systems, achieving high spatial resolution and effectively capturing geometrical properties can be challenging. Unstructured triangle meshes offer particular advantages in adapting to intricate fault geometry systems, providing greater flexibility. In Southern California and New Zealand, there are community fault models that provide a 3D representation of the fault system directly.

When dealing with arbitrary shapes that require mesh generation, we employ automatic mesh generators to discretize the fault plane into triangular or rectangular elements. For fundamental complexities such as step-overs and dipping faults, we recommend using GMSH (Geuzaine and Remacle, 2009). It allows the inclusion of bounded points, lines, and surfaces with specified shapes and desired grid sizes.

For realistic fault geometry, we suggest using CUBIT, which can produce a higher-quality mesh for complex fault geometries. Mesh quality controlled parameters (surface gradation, sizing function, the condition number of mesh smoothing, etc., see details in Appendix 2.C) can improve the shape quality of elements, which reduces the error for benchmark exercises.

2.4.3   Initial conditions and loading conditions

We establish the pre-stress field as the initial condition. It could be given in the sense of principle stresses or background stress tensor $\boldsymbol{\sigma}$. We can get traction along strike direction T_s, traction along the dip direction T_d and normal traction T_n by projecting onto the fault system:

$$\mathbf{T} = \boldsymbol{\sigma} \cdot \mathbf{n} \tag{2.24}$$
$$T_s = \mathbf{T} \cdot \mathbf{s} \tag{2.25}$$
$$T_d = \mathbf{T} \cdot \mathbf{d} \tag{2.26}$$
$$T_n = \mathbf{T} \cdot \mathbf{n}. \tag{2.27}$$

Because we assume the slip vector is parallel with the traction vector, the rake angle can be determined by traction net vector $\mathbf{T}$ and its strike component $\mathbf{T_s}$.

To initiate the first event, we impose a large slip rate in a circular patch in the center of the fault to initiate the rupture nucleation. The slip rate outside of the nucleation patch is constant V_0. At steady state, $\theta = \theta_{ss} = \frac{D_c}{V}$. Therefore, we have the steady-state initial condition of 5 unknowns $[V, \lambda, T_n, \tau, \theta]$ for the ODE system mentioned in section 2.2.

In FASTDASH, we have two approaches to apply to the far field time-dependent loading. The first approach is to consider a constant plate rate loading by using the back slip method:

$$\dot{\tau}_i^{load} = -V_{pl} \sum_{j=1}^{N} A_{ij}, \tag{2.28}$$

where V_{pl} is plate motion velocity. Faults are embedded by the creep region. The traction is calculated based on the relative slip rate. The final equivalent change in fault stress will be heterogeneous, increasing at the edge of the fault. In the second

approach, we consider a constant stress loading rate, which has the same principle direction as the Initial background stress tensor. Stress loading is directly projected onto the fault.

2.4.4   ODE solver: Runge-Kutta45

One powerful tool for solving ordinary differential equations (ODEs) in earthquake cycle simulations is the Runge-Kutta45 (RK45) solver.

The RK45 solver is an adaptive step-size solver that adjusts the step size based on local error estimates, efficiently handling the stiffness and nonlinearity in fault slip models. In earthquake cycle simulations, the RK45 solver integrates the equations of motion describing fault slip evolution. Its adaptive step-size control ensures accurate capture of rapid slip rate changes during seismic events and slower processes during interseismic periods (aseismic slip).

We implemented the RK45 solver in FASTDASH for computational efficiency. The solver operates in a local coordinate system, which saves time by constructing H-matrices in this system. Coordinate transformation is only performed when assigning initial conditions and outputting results, which is more effective in a fault-based system.

We verified the results using the spring-slider model, the Burridge-Knopoff model, and a 2D fault model.

For spring-slider model, the results were compared with those obtained using the Python package pyodesys, which solves systems of ordinary differential equations with various numerical integration methods, including RK45 (Haugene, 2016). The comparison is shown in Figure 2.6a.

For the Burridge-Knopoff model (This model was previously discussed in Chapter 1), we simulated a 20-block system and successfully reproduced the displacement on the 10th slider, in accordance with the findings of Erickson et al. (2011) (see Figure 2.6b).

For the 2D planar fault, we compared the maximum slip rate with results from the Virtual Earthquake Generator: Accelerated (VEGA), a 2D quasi-dynamic earthquake cycle modeling code developed by Pierre Romanet and Harsha S. Bhat (Romanet, 2017). Additionally, we compared the computational time among VEGA (written in Fortran), FASTDASH with Arrayfire for GPU computation (Yalamanchili et al., 2015), and FASTDASH with NumPy for CPU computation (Harris et al., 2020). We found that for systems with more than 2,000 elements, FASTDASH demonstrated better computational efficiency than VEGA, with GPU computation yielding the best performance. See Figure 2.6c.
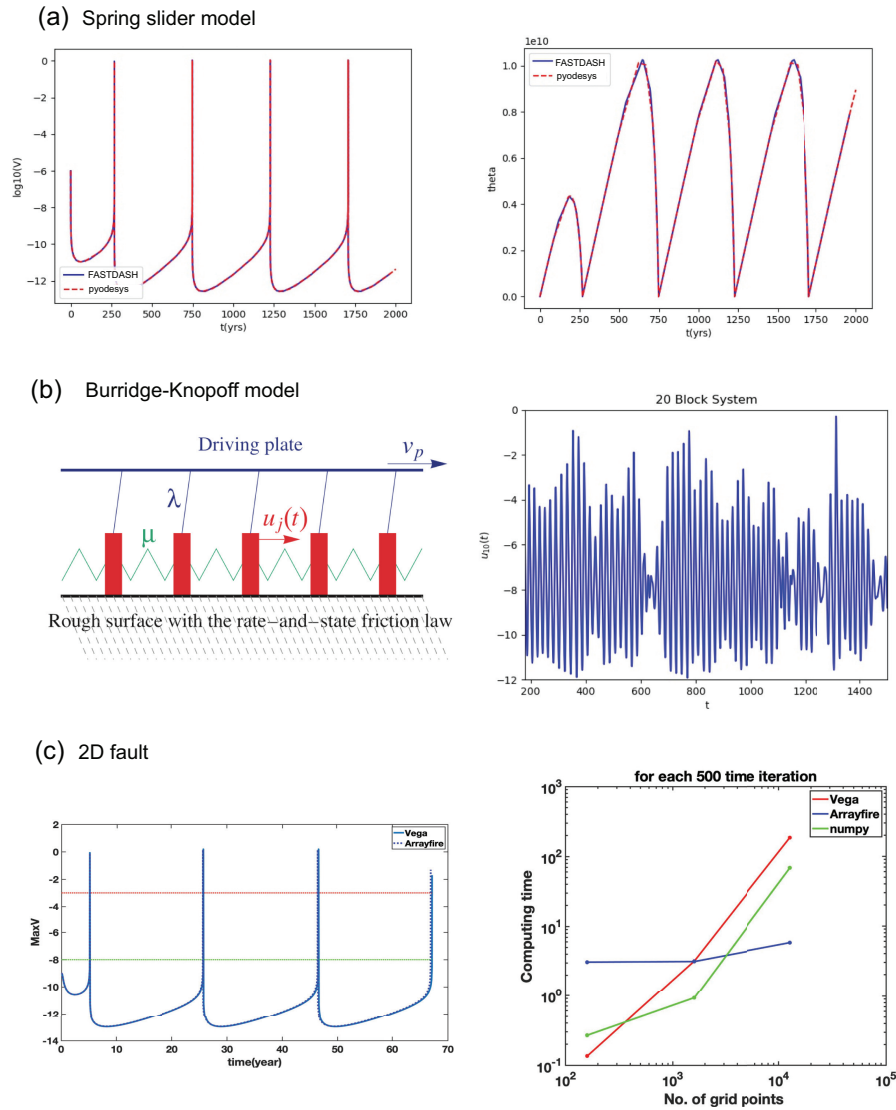
Figure 2.6: (a) Comparison of the spring-slider model results using the RK45 solver implemented in FASTDASH (blue solid line) and the Python package pyodesys (red dashed line). The left panel shows the slip rate evolution, while the right panel depicts the state variable evolution. The results exhibit excellent agreement, validating the RK45 solver implementation in FASTDASH. (b) The left panel illustrates the Burridge-Knopoff model setup. The right panel shows the displacement on the 10th slider of a 20-block Burridge-Knopoff model system, modeled using FASTDASH. These results (blue solid line) closely match the findings of Erickson et al. (2011) (red dashed line). Both time and displacement are non-dimensionalized. (c) The left panel compares the maximum slip rate for a 2D planar fault model using FASTDASH and the Virtual Earthquake Generator: Accelerated (VEGA). The right panel compares computational times for varying problem sizes among VEGA (Fortran), FASTDASH with Arrayfire (GPU computation), and FASTDASH with NumPy (CPU computation). The results show that for systems with more than 2000 elements, FASTDASH, especially with GPU computation, demonstrates the best computational efficiency.

2.4.5 Choose the numerical parameters

In order to choose the grid size, it is necessary to have a sufficient number of elements to resolve the process zone L_b. We already discussed L_b in Section 1.4.2. The grid size plays a pivotal role in achieving spatial convergence, while the time step is error-controlled through the Runge-Kutta45 method with a specified tolerance. Three Hmat parameters (Number of leaves N_{leaves}, parameter for admissibility condition η, tolerance for low rank approximation ϵ) were employed, and a convergence test for the SEAS Benchmark was conducted and will be discussed in Section 2.5. VTK files are utilized to save information at a given frequency to obtain output full-field data.

2.4.6 Post processing for catalog analysis

We identify slow slip events and earthquakes by using threshold values to determine the maximum slip rate. Slip rate thresholds for slow slip events and earthquakes are 10^{-8} m/s and 10^{-3} m/s, respectively. When the maximum slip rate exceeds a specific threshold, we identify it as an event. The duration during which the sliding rate exceeds the threshold is defined as the duration of the event T. We usually choose a slow slip threshold one order of magnitude greater than the plate rate. The indicators of seismic slip in experiments and geology is 10^{-3} m/s (Rowe and Griffith, 2015). We then do a mechanical and numerical check by ignoring the events in which the rupture area is smaller than the process zone size (Dieterich length $L_b = \frac{\mu D_c}{\sigma b}$, where μ is shear modulus, D_c is the characteristic slip distance, σ is normal stress and b is friction parameter for RSF that represents evolution effect (Dieterich, 1992)) and are resolved by less than 5 time steps.

The stress drop $\Delta\tau$ at location ξ is calculated as

$$\Delta\tau(\xi) = \tau^{after}(\xi) - \tau^{before}(\xi). \tag{2.29}$$

The moment rate $\dot{M}$ and moment M are calculated:

$$\dot{M}(t) = \int_A \mu V(\vec{\xi}, t) dA \tag{2.30}$$

$$M = \int_T \dot{M}(t) dt, \tag{2.31}$$

where A is the rupture plane, μ is the shear modulus and V is the slip rate.

Then the moment magnitude is calculated following Hanks and Kanamori (1979):

$$M_w = \frac{2}{3} \log_{10}(M) - 6.06. \tag{2.32}$$

2.5 Benchmark/Verification

In this section, we discuss and analyze a series of benchmark problems to verify the method's capabilities. Static benchmark validates the elastostatic solver, and dynamic benchmark validates the time-stepping solver.

2.5.1 Static benchmark

Penny shaped crack

To validate our code, we first compare our results with an analytical solution for a static crack, which is BigWham-related. To solve the elastic crack subjected to remote uniform stress loading, we superpose an uncracked body subjected to uniform far-field stress and a crack loaded by internal traction. In the case of the simplest axisymmetric crack, which is a penny-shaped crack under uniform remote stress loading, the problem can be solved analytically using the Green and Collins method, which is a method to solve boundary problems for a harmonic function. Sneddon (1946) gives the analytical solution for the penny-shaped crack under tensile loading. Based on that, Segedin (1951) gives the analytical solution under shear stress loading:

$$\Delta u(r) = \frac{8(\lambda + 2\mu)T}{\pi\mu(3\lambda + 4\mu)}\sqrt{R^2 - r^2}, r < R, \tag{2.33}$$

where u is the displacement discontinuity $u = u^+ - u^-$. r is the radius distance with the centroid. T is the remote shear stress loading, R is the radius of the crack. λ is the Lamé's parameter and μ is the shear modulus.

With FASTDASH, we can discretize the same penny-shaped crack with the triangular element (see Figure 2.7a), apply the displacement distribution from the analytical solution (see Figure 2.7b) and solve the traction numerically. Figure 2.7c showed the convergence of the result. The root mean square error reduces with increasing the number of elements.

Dugdale crack

According to the linear elastic fracture mechanism, there are stress singularities at the edge of the crack. Therefore, we also compare our result with the Dugdale crack model, which involves an elastic circular crack surrounded by a plastic zone. See Figure 2.8a. Dugdale crack is loaded by a uniform remote tension. For the elastic

(a)

(b)

(c)
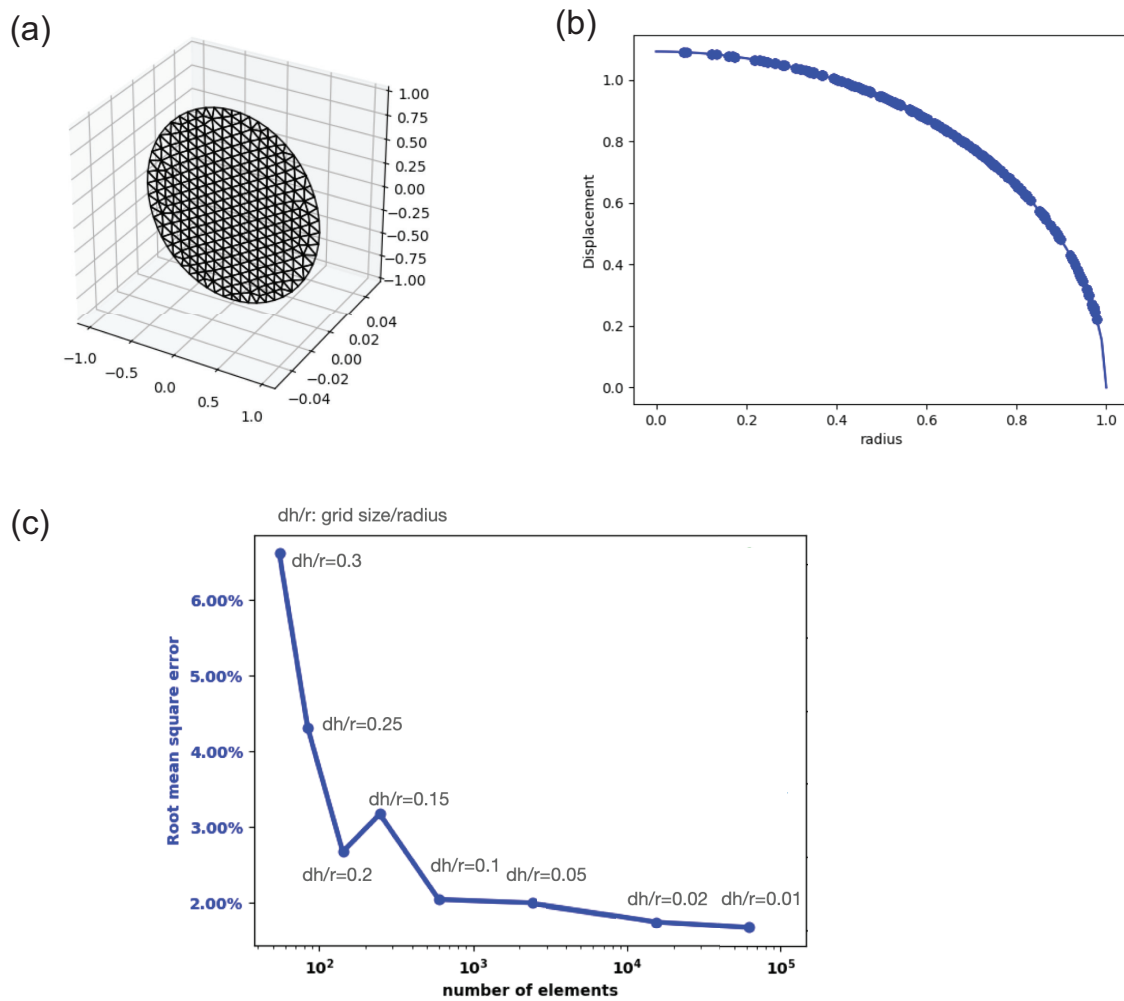
Figure 2.7: (a) A penny-shaped crack with a radius of 1, loaded by far-field shear stress and discretized with triangular elements. (b) Displacement analytical solution from Segedin (1951) along the crack radius shown in (a), with points representing the displacement at each discretized triangle. (c) The root mean square error between the calculated traction and analytical traction as the number of elements increases.
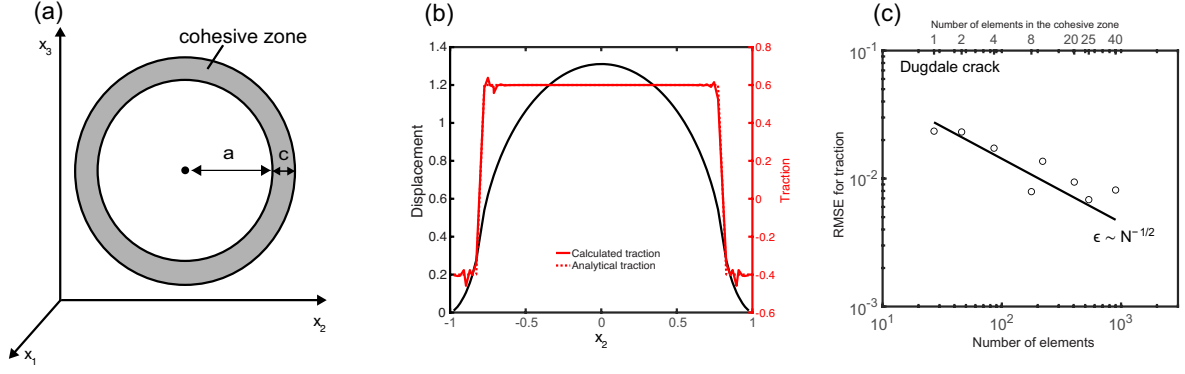
Figure 2.8: Static crack benchmark (a) Dugdale crack: elastic penny-shaped crack surrounded by cohesive zone (b) Analytical solution for Dugdale crack from Olesiak and Wnuk (1968) (c) Grid convergence as a function of number of elements.

crack $|x| < l$, it is traction-free, but in the plastic zone $l < |x| < a$, traction is equal to the yield stress σ_Y. The size of plastic zone is given by Dugdale (1960), as follows:

$$\frac{l}{a} = \sqrt{1 - \frac{\sigma_0^2}{\sigma_Y^2}}. \tag{2.34}$$

The displacement is given by Olesiak and Wnuk (1968)

$$\Delta u(\rho) = \frac{4(1-\nu)l\sigma_Y}{\mu\pi}\frac{1}{m} \times \begin{cases} \frac{\sigma_0}{\sigma_Y}\sqrt{1-\rho^2} - \sqrt{\frac{1-m^2}{1-\rho^2} + mE(\phi_1, \frac{\rho}{m})} & 0 < \rho < m \\ \frac{\sigma_0}{\sigma_Y}\sqrt{1-\rho^2} - \sqrt{\frac{1-\rho^2}{1-m^2} + \rho E(\phi_2, \frac{m}{\rho})} & \\ \quad - \frac{\rho^2-m^2}{\rho}F(\phi_2, \frac{m}{\rho}) & m < \rho < 1 \end{cases},$$

where $m = l/a$, and $\rho = r/a$. ν is the Poisson's ratio. And

$$\phi_1(\rho) = \arcsin\sqrt{\frac{1-m^2}{1-\rho^2}}, \phi_2(\rho) = \arcsin\sqrt{\frac{1-\rho^2}{1-m^2}}, \tag{2.35}$$

$E(\phi, k)$ and $F(\phi, k)$ are elliptical integrals of the first kind and second kind.

$$F(\phi, k) = \int_0^\phi \frac{d\alpha}{\sqrt{1-k^2\sin^2\alpha}}, E(\phi, k) = \int_0^\phi \sqrt{1-k^2\sin^2\alpha}d\alpha. \tag{2.36}$$

With superposition with remote tension σ_0, the traction $T = \sigma_0$ in the elastic crack and $T = \sigma_0 - \sigma_Y$ in the plastic zone.

We calculated the traction due to slip using the analytical solution and compared it with the analytical loading traction (Figure 2.8b). Additionally, we verified that the root mean square error between the numerical and analytical solutions decreases and converges as the number of elements increases, as shown in Figure 2.8c.

2.5.2 Dynamic benchmark

For dynamic fault problems, there is no analytical solution. Sequences of Earthquakes and Aseismic Slip (SEAS) is a project proposed by the Southern California Earthquake Center (SCEC) to validate different numerical implementations for earthquake cycles. We validate FASTDASH with SEAS Benchmark problem BP4-QD (Jiang et al., 2022). It is a problem to solve a 2D fault subjected to constant plate loading rate V_p embedded in a 3D homogeneous linear elastic whole space medium. See Figure 2.9a. The fault plane consists of a velocity-weakening rectangle surrounded by a strengthening patch, with a friction transition strip in between. The initial nucleation zone (green square) is located at the bottom left with a higher initial slip rate.

The use of boundary integral equations is widespread in the SEAS community. We compare our results with Unicycle, which is a boundary element method for earthquake cycle simulation without H matrices acceleration (Barbot et al., 2017). Figure 2.9b and Figure 2.9c shows the stress and accumulated slip on the central station. Figure 2.9d and Figure 2.9e shows the maximum slip rate for the entire fault and rupture front contour for the first earthquake. Both local and global data show good agreement with the results.

We also quantify the numerical error with the SEAS benchmark. We calculate the root-mean-square error to quantify the difference in rupture arrival time by using the maximum slip rate for the first six earthquakes between FASTDASH and Unicycle. The time-accumulating error has already been taken into account and is shown as,

$$RRMSE = \sqrt{\sum_{i=1}^{i=6}(\Delta t_i)^2/6} / \sqrt{\sum_{i=1}^{i=6}(t_i^U)^2}, \qquad (2.37)$$

where Δt_i is the rupture arrival time difference between FASTDASH and Unicycle for the ith ($i \leq 6$) earthquake and t_i^U is the rupture arrival time calculated from Unicycle for the ith ($i \leq 6$) earthquake.

We did a parametrical study for H-matrices properties and tolerance for ODE solver to test the convergence, as seen in Figure 2.10. With a larger number of leaves, H-matrices have less compression and high accuracy but longer computing time. It is not sensitive to η. The increase in time for N = 400 can be related to the structure of H-matrices. The results converge at a tolerance of 10^{-4} for the ODE solver, and errors do not decrease further, suggesting the reference might use the same tolerance. The smallest error occurs with a grid size of 500, which matches the reference results.

Figure 2.9: SEAS SCEC benchmark (a) SEAS benchmark problem 4 (Jiang et al., 2022). (b) and (c) Stress and slip in strike direction at station shown in (a). (d) Maximum slip rate on the entire fault. (e) Rupture front contour for the first earthquake.
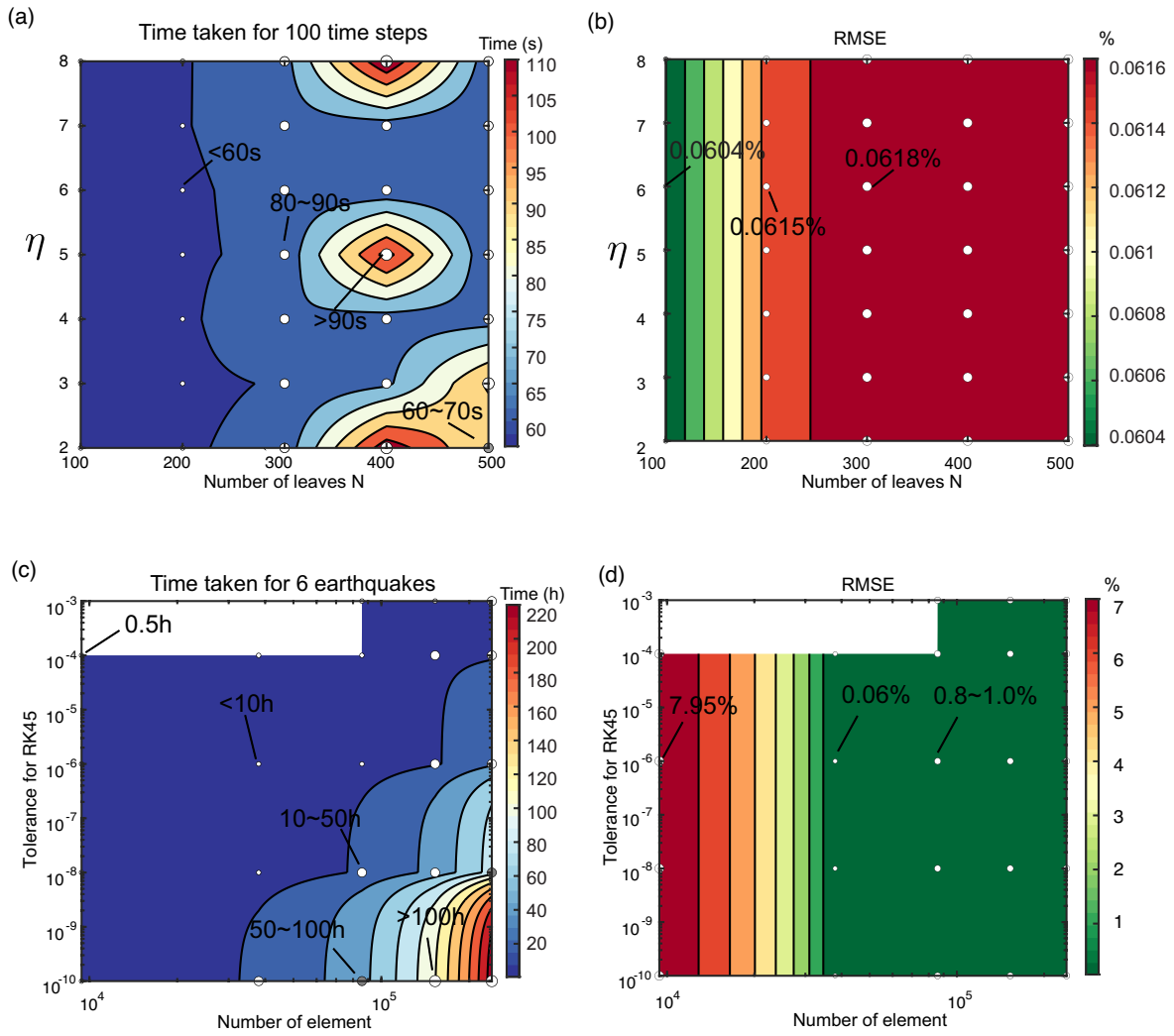
Figure 2.10: Quantify the numerical error with SEAS benchmark (a) The computing time with different Hmat properties (η and number of leaves N) (b) The Root mean square error relative to Unicycle with different Hmat properties (c) The computing time for 6 earthquakes with number of elements and tolerance of RK45. White region is where the results do not converge (d) The root mean square error with the number of elements and tolerance of RK45

.

Table 2.1: Best numerical parameters for SEAS BP4-QD

Parameters	Description	Value
N	H-mat property: maximum leaf size	100
η	H-mat property: distance between accepted blocks	3
ϵ	H-mat property: accuracy for ACA	10^{-4}
Δs	Grid size	$L_b/4$
ϵ_{rk}	tolerance for RK	10^{-4}

The best numerical parameters for BP4-QD are listed in Table 2.1, where we have the most time-efficient and accurate simulations.

Appendix 2.A   ODE system

We differentiate the friction resistance in Equation 2.11,

$$\dot{\tau}^f = -\dot{f} \cdot (T_n - p) - f \cdot (\dot{T}_n - \dot{p}), \tag{2.38}$$

where T_n is normal traction and p is pore pressure.

We differentiate the rate and state friction in Equation 2.12

$$\dot{f} = \frac{\partial f}{\partial V} \dot{V} + \frac{\partial f}{\partial \theta} \dot{\theta}. \tag{2.39}$$

Let

$$\frac{\partial f}{\partial V} = A \tag{2.40}$$

$$\frac{\partial f}{\partial \theta} = B. \tag{2.41}$$

We differentiate Equation 2.14, Equation 2.15, Equation 2.16, Equation 2.11, Equation 2.13 and get a set of ODEs. It is important to note that our ODE solver operates in a local coordinate system, so we transform the coordinates accordingly:

$$\dot{\tau} \cos \alpha - \dot{\alpha} \tau \sin \alpha = \dot{\tau}_1^{el} + \dot{\tau}_1^{load} + \eta_s (\dot{V} \cos \alpha - \dot{\alpha} V \sin \alpha)$$
$$\dot{\tau} \sin \alpha + \dot{\alpha} \tau \cos \alpha = \dot{\tau}_2^{el} + \dot{\tau}_2^{load} + \eta_s (\dot{V} \sin \alpha + \dot{\alpha} V \cos \alpha)$$
$$\dot{T}_n = \dot{\tau}_3^{el} + \dot{\tau}_3^{load}$$
$$\dot{\tau} = -(A\dot{V} + B\dot{\theta}) \cdot (T_n - p) - f \cdot (\dot{T}_n - \dot{p})$$
$$\dot{\theta} = 1 - \frac{V\theta}{D_c},$$

where, τ_1 and τ_2 are tractions along $\mathbf{e_1}$ and $\mathbf{e_2}$ in local coordinate system, α is the angle between $\mathbf{e_1}$ and the slip vector. These ODEs can be written in matrix-vector

multiplication form as follows:

$$
\begin{bmatrix}
-\eta_s \cos\alpha & \eta_s V \sin\alpha - \tau\sin\alpha & 0 & \cos\alpha & 0 \\
-\eta_s \sin\alpha & -\eta_s V \cos\alpha + \tau\cos\alpha & 0 & \sin\alpha & 0 \\
0 & 0 & 1 & 0 & 0 \\
A(T_n - p) & 0 & f & 1 & B(T_n - p) \\
0 & 0 & 0 & 0 & 1
\end{bmatrix}
\frac{\partial}{\partial t}
\begin{bmatrix}
V \\ \alpha \\ T_n \\ \tau \\ \theta
\end{bmatrix}
=
\begin{bmatrix}
\dot{\tau}_1^{el} + \dot{\tau}_1^{load} \\
\dot{\tau}_2^{el} + \dot{\tau}_2^{load} \\
\dot{\tau}_3^{el} + \dot{\tau}_3^{load} \\
f\dot{p} \\
\frac{d\theta}{dt}
\end{bmatrix} .
$$
$$(2.42)$$

We can write this ODE system explicitly

$$
\frac{\partial}{\partial t}
\begin{bmatrix}
V \\ \alpha \\ T_n \\ \tau \\ \theta
\end{bmatrix}
=
\begin{bmatrix}
\frac{\cos\alpha}{D_1} & \frac{\sin\alpha}{D_1} & \frac{f}{D_1} & -\frac{1}{D_1} & \frac{B(T_n-p)}{D_1} \\
\frac{\sin\alpha}{\eta V - \tau} & -\frac{\cos\alpha}{\eta V - \tau} & 0 & 0 & 0 \\
0 & 0 & 1 & 0 & 0 \\
\frac{A\cos\alpha(p-T_n)}{D_1} & \frac{A\sin\alpha(p-T_n)}{D_1} & \frac{f\eta}{D_1} & -\frac{\eta}{D_1} & \frac{B\eta(T_n-p)}{D_1} \\
0 & 0 & 0 & 0 & 1
\end{bmatrix}
\begin{bmatrix}
\dot{\tau}_1^{el} + \dot{\tau}_1^{load} \\
\dot{\tau}_2^{el} + \dot{\tau}_2^{load} \\
\dot{\tau}_3^{el} + \dot{\tau}_3^{load} \\
f\dot{p} \\
\frac{d\theta}{dt}
\end{bmatrix} ,
$$
$$(2.43)$$

where $D = A(p - T_n) - \eta$

For non-regularised rate and state friction law, friction is

$$
f = f_0 + a\log(\frac{V}{V_{ref}}) + b\log(\frac{\theta V_{ref}}{D_c})
\tag{2.44}
$$

$$
A = \frac{\partial f}{\partial V} = \frac{a}{V}
$$
$$
B = \frac{\partial f}{\partial \theta} = \frac{b}{\theta}.
$$

For regularized form

$$
f = a \cdot \operatorname{arcsinh}\left(\frac{V}{2 * V_{ref}} \exp \frac{f_0 + b\ln\left(V_{ref}\theta/Dc\right)}{a}\right)
\tag{2.45}
$$

$$
z = \frac{\exp \dfrac{f_0 + b\log\left(\frac{\theta V_{ref}}{D_c}\right)}{a}}{2V_{ref}}
\tag{2.46}
$$

$$
A = \frac{\partial f}{\partial V} = \frac{a}{\sqrt{\frac{1}{z^2} + V^2}}
\tag{2.47}
$$

$$
B = \frac{\partial f}{\partial \theta} = \frac{\partial f}{\partial V} \cdot \frac{bV}{a\theta}.
\tag{2.48}
$$

Appendix 2.B   Coordinate transformation

For the fault-based system:

$$\mathbf{s} = \frac{\mathbf{x_3} \times \mathbf{n}}{||\mathbf{x_3} \times \mathbf{n}||} = \begin{vmatrix} i & j & k \\ 0 & 0 & 1 \\ e_{31} & e_{32} & e_{33} \end{vmatrix} /||\mathbf{x_3} \times \mathbf{n}|| = \frac{1}{\sqrt{e_{31}^2 + e_{32}^2}} (-e_{32}, e_{31}, 0). \quad (2.49)$$

We define $\mathbf{d}$ to point downward:

$$\mathbf{d} = \mathbf{n} \times \mathbf{s} = \frac{1}{\sqrt{e_{31}^2 + e_{32}^2}} \begin{vmatrix} i & j & k \\ e_{32} & -e_{31} & 0 \\ e_{31} & e_{32} & e_{33} \end{vmatrix} = \frac{1}{\sqrt{e_{31}^2 + e_{32}^2}} (-e_{31}e_{33}, -e_{32}e_{33}, e_{31}^2 + e_{32}^2)$$

$$(2.50)$$

$$\mathbf{n} = \mathbf{e_3} = (e_{31}, e_{32}, e_{33}), \quad (2.51)$$

which is written in the global system.

Slip rate vector $\vec{V}$ in local system is $(V_{e_1}, V_{e_2}, V_{e_3})$, in fault based system is (V_s, V_d, V_n). In global system, slip vector $\vec{V}$ can be written with the basis $(\mathbf{e_1}, \mathbf{e_2}, \mathbf{e_3})$, $\vec{V} = \vec{V_{local}} = V_{e_1}\mathbf{e_1} + V_{e_2}\mathbf{e_2} + V_{e_3}\mathbf{e_3}$.

With basis $(\mathbf{s}, \mathbf{d}, \mathbf{n})$, $\vec{V} = \vec{V_{fault}} = V_s\mathbf{s} + V_d\mathbf{d} + V_n\mathbf{n}$. Considering the vector algebra relation $A \cdot (B \times C) = C \cdot (A \times B)$

In the strike direction, we can write:

$$V_s = \vec{V_{local}} \cdot \mathbf{s} = \vec{V_{local}} \cdot \frac{\mathbf{x_3} \times \mathbf{n}}{||\mathbf{x_3} \times \mathbf{n}||} = \frac{1}{\sqrt{e_{31}^2 + e_{32}^2}} \mathbf{x_3} \cdot (\mathbf{n} \times \vec{V_{local}}). \quad (2.52)$$

Because $\mathbf{e_1}, \mathbf{e_2}, \mathbf{e_3}$ are orthognal, we can write $\mathbf{e_3} \times \mathbf{e_1} = \mathbf{e_2}$, $\mathbf{e_3} \times \mathbf{e_2} = -\mathbf{e_1}$

$$\mathbf{n} \times \vec{V_{local}} = \mathbf{e_3} \times (V_{e_1}\mathbf{e_1} + V_{e_2}\mathbf{e_2} + V_{e_3}\mathbf{e_3}) = V_{e_1}\mathbf{e_2} - V_{e_2}\mathbf{e_1}. \quad (2.53)$$

Then,

$$V_s = \frac{1}{\sqrt{e_{31}^2 + e_{32}^2}} \mathbf{x_3} \cdot (V_{e_1}\mathbf{e_2} - V_{e_2}\mathbf{e_1}) = \frac{1}{\sqrt{e_{31}^2 + e_{32}^2}} (V_{e_1}e_{23} - V_{e_2}e_{13}). \quad (2.54)$$

In the dip direction, we can write:

$$V_d = \vec{V_{local}} \cdot \mathbf{d} = \vec{V_{local}} \cdot (\mathbf{n} \times \mathbf{s}) = \mathbf{s} \cdot (\vec{V_{local}} \times \mathbf{n}) = \frac{1}{\sqrt{e_{31}^2 + e_{32}^2}} (\mathbf{x_3} \times \mathbf{n}) \cdot (\vec{V_{local}} \times \mathbf{n}). \quad (2.55)$$

Considering the vector algebra relation $(A \times B) \cdot (C \times D) = (A \cdot C)(B \cdot D) - (B \cdot C)(A \cdot D)$. Slip rate vector has no opening component, so $\mathbf{n} \cdot \vec{V_{local}} = 0$

Then,

$$V_d = \frac{1}{\sqrt{e_{31}^2 + e_{32}^2}} \mathbf{x_3} \cdot \vec{V_{local}} = \frac{1}{\sqrt{e_{31}^2 + e_{32}^2}} (V_{e_1} e_{13} + V_{e_2} e_{23} + V_{e_3} e_{33}). \tag{2.56}$$

We can write the slip rate in matrix format as follows:

$$\begin{bmatrix} V_s \\ V_d \\ V_n \end{bmatrix} = \begin{bmatrix} \dfrac{e_{23}}{\sqrt{e_{31}^2 + e_{32}^2}} & \dfrac{-e_{13}}{\sqrt{e_{31}^2 + e_{32}^2}} & 0 \\ \dfrac{e_{13}}{\sqrt{e_{31}^2 + e_{32}^2}} & \dfrac{e_{23}}{\sqrt{e_{31}^2 + e_{32}^2}} & 0 \\ 0 & 0 & 1 \end{bmatrix} \begin{bmatrix} V_{e_1} \\ V_{e_2} \\ V_{e_3} \end{bmatrix}. \tag{2.57}$$

The matrix transformation from local system to fault-based system R is

$$\boldsymbol{R} = \begin{bmatrix} \dfrac{e_{23}}{\sqrt{e_{31}^2 + e_{32}^2}} & \dfrac{-e_{13}}{\sqrt{e_{31}^2 + e_{32}^2}} & 0 \\ \dfrac{e_{13}}{\sqrt{e_{31}^2 + e_{32}^2}} & \dfrac{e_{23}}{\sqrt{e_{31}^2 + e_{32}^2}} & 0 \\ 0 & 0 & 1 \end{bmatrix}. \tag{2.58}$$

The inverse of $\boldsymbol{R}$ can help us transform from the fault-based system to the local system:

$$\boldsymbol{R}^{-1} = \begin{bmatrix} \dfrac{e_{23}\sqrt{e_{31}^2 + e_{32}^2}}{e_{23}^2 + e_{13}^2} & \dfrac{e_{13}\sqrt{e_{31}^2 + e_{32}^2}}{e_{23}^2 + e_{13}^2} & 0 \\ \dfrac{-e_{13}\sqrt{e_{31}^2 + e_{32}^2}}{e_{23}^2 + e_{13}^2} & \dfrac{e_{23}\sqrt{e_{31}^2 + e_{32}^2}}{e_{23}^2 + e_{13}^2} & 0 \\ 0 & 0 & 1 \end{bmatrix}. \tag{2.59}$$

Thus, the slip rate can be written in the local coordinate system as follows:

$$\begin{bmatrix} V_{e_1} \\ V_{e_2} \\ V_{e_3} \end{bmatrix} = \begin{bmatrix} \dfrac{e_{23}\sqrt{e_{31}^2 + e_{32}^2}}{e_{23}^2 + e_{13}^2} & \dfrac{e_{13}\sqrt{e_{31}^2 + e_{32}^2}}{e_{23}^2 + e_{13}^2} & 0 \\ \dfrac{-e_{13}\sqrt{e_{31}^2 + e_{32}^2}}{e_{23}^2 + e_{13}^2} & \dfrac{e_{23}\sqrt{e_{31}^2 + e_{32}^2}}{e_{23}^2 + e_{13}^2} & 0 \\ 0 & 0 & 1 \end{bmatrix} \begin{bmatrix} V_s \\ V_d \\ V_n \end{bmatrix}. \tag{2.60}$$

Therefore,

$$V_{e_1} = \frac{\sqrt{e_{31}^2 + e_{32}^2}}{e_{23}^2 + e_{13}^2} (V_s e_{23} + V_d e_{13}) \tag{2.61}$$

$$V_{e_2} = \frac{\sqrt{e_{31}^2 + e_{32}^2}}{e_{23}^2 + e_{13}^2}(-V_s e_{13} + V_d e_{23}) \qquad (2.62)$$

$$\alpha = \tan^{-1}\left(\frac{V_{e_2}}{V_{e_1}}\right) \qquad (2.63)$$

$$\lambda = \tan^{-1}\left(\frac{V_d}{V_s}\right). \qquad (2.64)$$

Appendix 2.C   Mesh subtleties

When performing static crack benchmarks for Dugdale cracks, we observe that high-quality meshes result in lower errors. This indicates that the collocation method is somewhat mesh-dependent, performing best with well-shaped elements. Therefore, it is crucial to ensure high mesh quality when solving these problems.

Meshes should adapt to various geometric or user-defined properties (such as heterogeneous friction) to accurately represent surfaces mathematically (see example in Figure 2.11a). However, capturing these geometric properties sometimes results in variations in size and the presence of degenerate (non-convex or inverted) elements, as shown in Figure 2.11b-d.

CUBIT provides several parameters to control mesh quality, such as surface gradation, sizing functions, condition number smoothing, surface smoothing, and geometry approximation angle. Adjusting these parameters can significantly improve the shape quality of mesh elements. We recommend using Trimesh, which uses the third-party library MeshGems; Trimesh offers robust and fast automatic mesh generation. It optimizes mesh quality based on Tridelanunay principles.

Surface gradation controls how rapidly triangle sizes change when transitioning from small to larger sizes (Figure 2.11b and Figure 2.11c). The default setting for gradation is 1.3. A smoother gradation (closer to 1.0) results in more elements, especially around small features.

Sizing functions can be linear or constant, as shown in Figure 2.12. Variations in grid size can cause oscillations. Therefore, it is better to control the grid size uniformly to reduce errors.

Condition number enhances element shapes by optimizing the mesh condition number, ensuring non-inverted, well-shaped elements. The value of beta is compared at each iteration to the maximum condition number in the mesh. It ensures

(a)

(b)

(c)

(d)
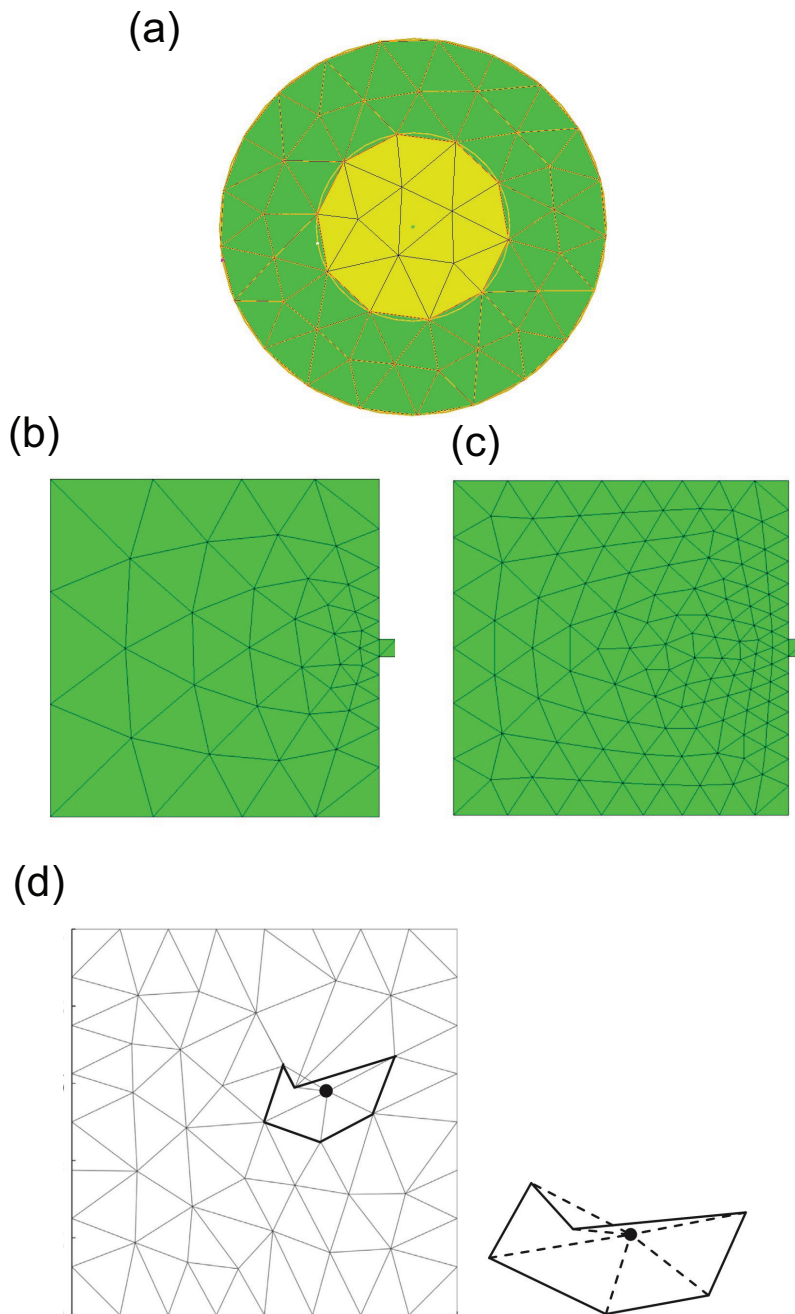
Figure 2.11: (a) An example of a discretized mesh capturing two geometrical boundaries (outer and inner circles). (b) Mesh with large surface gradation. (c) Mesh with small surface gradation. (d) Degenerate elements.
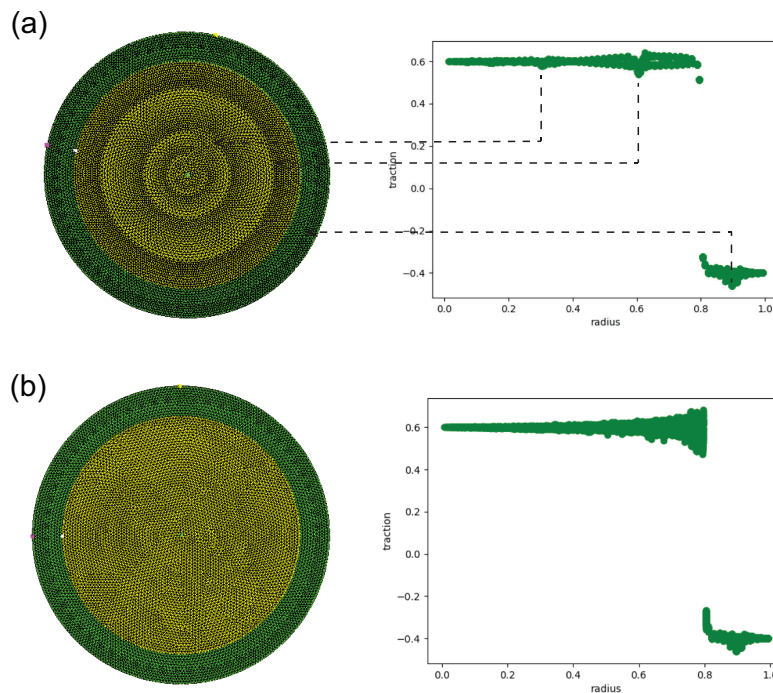
Figure 2.12: Dugdale crack meshed with a constant size function. The traction shown along the radius is superposed in all directions. Traction oscillates where the grid size changes. (b) Dugdale crack meshed with a linear size function.

that the maximum condition number is less than the beta, resulting in better quality. Specifies the number of cores to use for processing, typically set to 4 for balanced performance.

Surface Smoothing is used to refine the mesh surface further to improve overall quality.

There are also other parameters to control mesh quality. Different parameters can be adjusted as needed to achieve better mesh quality. The Jacobian Ratio measures the deviation of an element's shape from an ideally shaped element, ensuring high-quality mesh elements. Geometry Approximation Angle can help capture curved features using linear edges of triangles. Adjusts triangle size on curved boundaries so that the linear edges deviate from the geometry by no more than the specified angle. This ensures smaller elements are placed in regions of higher curvature, controlling element distribution and capturing geometric features accurately.

To achieve accurate and reliable results in static crack benchmarks for Dugdale cracks, it is essential to use high-quality meshes. Utilizing Trimesh with optimized settings in Cubit, including surface gradation, condition number smoothing, surface

smoothing, and geometry approximation angle, ensures well-shaped elements and minimizes errors. Adjusting these parameters appropriately, along with using the beta and CPU optimization criteria, allows for better adaptation to geometric and user-defined properties, resulting in superior mesh quality.

Chapter 3

Fundamental complexities: step-over fault system

Avant-propos

Dans cette étude, nous examinons l'émergence d'événements sismiques lents et rapides complexes, entraînés par des interactions élastiques et des champs de contraintes hétérogènes sur plusieurs cycles sismiques au sein d'un système de failles 3D avec deux failles planaires parallèles. Nous visons à comprendre comment la géométrie complexe et multi-segmentée de ce système de failles 3D influence la dynamique de glissement. Nous utilisons un modèle de cycle sismique quasi-dynamique en 3D avec une méthode des éléments de frontière accélérée par des matrices hiérarchiques (Cheng et al., 2024b). Pour une faille isolée unique sous friction à taux de fragilisation spatialement uniforme, des séismes réguliers se produisent si la longueur de la faille dépasse la longueur de nucléation. Cependant, lorsque l'on considère l'interaction entre deux failles, des événements de glissement spatio-temporels complexes émergent en raison de l'interaction des contraintes de la faille voisine. Divers événements de glissement lent, ainsi que des séismes ayant des ruptures partielles ou complètes, sont identifiés dans le catalogue de glissement. Nous investiguons systématiquement comment les propriétés géométriques et frictionnelles influencent ces séquences sismiques et asismiques complexes. En incorporant les interactions de la troisième dimension, notre modèle permet une gamme plus large de paramètres qui soutiennent la coexistence de séismes et d'événements de glissement lent par rapport aux modèles 2D. Concernant la mise à l'échelle moment-durée des événements de glissement lent, un débat persistant existe dans les études observationnelles concernant les relations de mise à l'échelle cubique et linéaire. Nos résultats numériques

suggèrent que le glissement lent a une mise à l'échelle linéaire, mais cette relation de mise à l'échelle peut fortement dépendre du seuil de taux de glissement choisi pour identifier les événements de glissement lent.

3.1 Introduction

Earthquake-related slip accounts for only a fraction of overall slip dynamics in plate tectonics, with advancements in geodetic networks revealing slow slip events (SSEs) in various tectonic environments such as the Cascadia subduction zone (Hirose et al., 1999; Dragert et al., 2001), Haiyuan fault (Jolivet et al., 2013), and San Andreas fault (Rousset et al., 2019). SSEs involve episodic, slow shear motion with minimal seismic activity and are linked to slow earthquakes like low-frequency earthquakes (LFEs), very low-frequency earthquakes (VLFEs), and tremors (Ito et al., 2007; Shelly et al., 2007; Michel et al., 2018). These events exhibit diverse spatiotemporal complexities, occurring at different depths and durations across regions like Nankai Trough (Obara et al., 2004; Hirose and Obara, 2006; Ozawa et al., 2001) and Hikurangi (Wallace and Eberhart-Phillips, 2013). SSEs can precede, trigger, or occur independently of earthquakes, influencing fault behavior by altering the stress field (Avouac, 2015; Bürgmann, 2018; Obara and Kato, 2016). Understanding SSEs is essential for gaining insights into earthquake mechanisms, as they emerge from various factors including frictional properties (Liu and Rice, 2005; Rubin, 2008; Skarbek et al., 2012; Luo and Ampuero, 2017; Nie and Barbot, 2021), fault geometry, thermal instabilities (Wang and Barbot, 2020), and the presence of fluids (Bernaudin and Gueydan, 2018; Cruz-Atienza et al., 2018; Bhattacharya and Viesca, 2019; Gao and Wang, 2017; Garagash and Germanovich, 2012).

For a long time, the geometry of subduction interfaces was assumed to be simple, especially when studying slow slip events (SSEs) through other physical mechanisms such as heterogeneous friction or considering fluid, as mentioned before. However, the fault geometry has complex 3D structures. For example, recent imaging of the Ecuadorian subduction zone by Chalumeau et al. (2024) reveals that earthquakes occur across multi-fault segments and subparallel planes, challenging this simplistic view. This complexity emphasizes the need to account for complex fault geometries when studying SSEs. Observations from Hikurangi, including drilling data and seismic reflection images, further highlight the role of material heterogeneity and geometric complexity in promoting slow slip events (Barnes et al., 2020; Kirkpatrick et al., 2021). Similarly, in the Cascadia subduction zone, spatial variations along the downdip direction of SSEs suggest a significant influence of geometric factors (Hall

et al., 2018). Mitsui and Hirahara (2006) simulated slow slip events, demonstrating the role of varying dip angle of geometry. Advanced simulations, such as those performed by Li and Liu (2016) for Cascadia and Perez-Silva et al. (2021) for Guerrero, indicate that non-planar fault geometries are pivotal in understanding SSEs. Fundamental complexities in fault geometry are also considered in SSE modeling, including investigations into precursory slow slip influenced by fault roughness (Cattania and Segall, 2021) and the emergence of slow slip events from two parallel faults under spatial uniform rate-weakening friction in 2D models (Romanet et al., 2018). Laboratory experiments by (Kwiatek et al., 2024) further underscore the complexity, showing both fast and slow ruptures with varying fault slips on rough faults. The effect of stress interaction between multiple faults on slow slip events in 3D models is still unresolved.

In this work, we focus on a step-over configuration with two parallel faults under spatially uniform rate-weakening friction conditions. We investigate how geometrical and frictional parameters influence slip behaviors in a 3D model. Our study identifies four slip regimes: only slow slip events (SSEs), SSE-dominant, earthquake-dominant, and only earthquakes. In contrast, under the same model settings, a single planar fault only produces earthquakes. We introduce a new metric as a function of fault width, fault length, overlap distance, and distance between faults to determine the geometric range conducive to the coexistence of earthquakes and slow slip events. These complex spatiotemporal slip events naturally arise from traction heterogeneities (we call them traction asperities) evolving with space and time due to fault interactions.

3.2   Method

We used the recently developed numerical approach, FASTDASH (Cheng et al., 2024b), which integrates a 3D quasi-dynamic earthquake cycle modeling using boundary element methods accelerated by Hierarchical matrices. This technique significantly optimizes computational efficiency, reducing complexity from $O(N^2)$ to $O(N \log N)$, where N represents the number of discretized fault elements. Such efficiency is crucial for solving complex 3D fault systems effectively. We analyzed a fault system with two overlapping faults subjected to a far-field constant stress rate loading. Both faults are governed by laboratory-derived rate and state friction (RSF) law with aging state evolution (Dieterich, 1979b; Ruina, 1983). Friction is spatially uniform rate weakening. This model includes radiation damping, which is an approximation of inertial effect (Rice, 1993). Therefore, the model neglects any elastic wave propa-

gation. Both shear and normal traction can vary due to elastic interaction between two faults. With this approach, we can calculate key information on faults, including maximum slip rate, moment rate, duration, and the distributions of stress and slip during multiple earthquake cycles.

In stability analysis, two important parameters are the process zone length (L_b) and the nucleation length (L_{nuc}). L_b represents the region where the breakdown energy is released and where traction and slip change rapidly. Numerical methods require a sufficient number of grid points within this zone to capture these variations accurately. In this study, we use a grid size of $\Delta s = L_b/3$. On the other hand, L_{nuc} is the critical length necessary for slip nucleation to occur. For faults that are governed by rate and state friction with aging law, these parameters are defined as follows: (Lapusta and Liu, 2009; Rubin and Ampuero, 2005; Viesca, 2016),

$$L_b = \frac{\mu D_c}{b \sigma_n} \tag{3.1}$$

$$L_{nuc} = \frac{2 L_b}{\pi (1 - a/b)^2} \qquad a/b \to 1, \tag{3.2}$$

where μ is shear modulus, D_c is the characteristic slip distance, and a, b are the rate and state friction parameters to represent the direct effect and evolution effect. For rate weakening friction, $0 < a/b < 1$. σ_n is the normal traction.

We aim to understand how the geometrical parameters and frictional parameters affect the fault behavior on a 3D extensional step-over fault configuration. The geometrical parameters include fault width W, fault length L_f, overlap distance L, and distance between two faults D (see Figure 3.1a). All the length properties are scaled by L_{nuc}, which is a function of friction properties a/b. We fix the aspect ratio of fault $L_f/W = 3$ and vary fault width W/L_{nuc} from 1.5 to 8, overlap distance L/L_f from 0 to 1, distance between two faults D/L_{nuc} 0.1 to 5. Friction $a/b \in \{0.4, 0.6, 0.8\}$. We perform 61 simulations with different geometry and friction settings for our analysis. The model parameters are shown in Table 3.1.

3.3 Result

For a single fault that is longer than L_{nuc} under spatial uniform rate-weakening friction ($a/b < 1$), only periodic earthquakes will occur (Liu and Rice, 2005; Rubin, 2008). By considering a fault system with two parallel faults, spatiotemporal complex slip events emerge due to the traction heterogeneity produced by fault interaction (Figure 3.1).

Table 3.1: Model parameters

Parameters	Description	Value
b	RSF evolution effect parameter	0.01
D_c	Characteristic distance	0.001 m
V_{ref}	Reference slip rate for RSF	10^{-6} m/s
f_0	Reference friction coefficient for RSF	0.6
μ	Shear modulus	3×10^{10} Pa
ρ	Density	2670 kg/m^3
C_s	Shear wave velocity	3464 m/s
ν	Poisson's ratio	0.25
V_0	Initial slip rate	10^{-9} m/s
$\dot{\tau}_s$	Shear loading rate	0.05 Pa/s

Table 3.2: Friction and geometry parameters for Model 1 and Model 2

Parameters	Description	Value for Model 1	Value for Model 2
a	RSF direct effect parameter	0.008	0.008
L_{nuc}	Nucleation length	477.46 m	477.46 m
D	Distance between two faults	47.746 m	47.746 m
W	Width of the fault	954.92 m	1909.80 m
L_f	Length of the fault	2864.80 m	5729.50 m
L	Overlap distance	1432.40 m	2864.80 m

We classify earthquakes and slow slip events based on their slip rates. An event is considered an earthquake if its maximum slip rate is greater than 10^{-3} m/s. This threshold is chosen based on experiments and geology observation (Rowe and Griffith, 2015). The slip rate of slow slip events is 1 or 2 orders higher than the plate rate. In our study, if the maximum slip rate falls between 10^{-8} m/s and 10^{-3} m/s, it is classified as a slow slip event. Various slow slip events, as well as earthquakes having partial or full ruptures, are identified in the slip catalog (Figure 3.1d). With various combinations of geometry and friction parameters, we identify four regimes: only slow slip events, SSE-dominant, earthquake-dominant, and only earthquakes. We will present the spatial-temporal complex events we get from our simulations and reproduce the moment-duration scaling law.

3.3.1   Spatial-temporal complex events

We demonstrate that a step-over configuration produces a wide range of spatio-temporal complex events. To illustrate the transition between SSE-dominant and earthquake-dominant regimes, we present two examples: Model 1 and Model 2. The parameters are detailed in Table 3.2. By increasing the fault width (W) from $2L_{nuc}$ to $4L_{nuc}$, we observe a shift from SSE-dominant to earthquake-dominant behavior. In Model 1, slow slip events dominate the slip catalog, with only three earthquakes on each fault during the period in which ten earthquakes occur on a single fault. In Model 2, we observe periodic earthquakes with two slow events occurring during the interseismic period. The evolution of slip for each event over time and space is shown in Figure 3.1d.

We selected four events from these two simulations to display the slip distribution on the two fault planes, illustrating both SSEs and earthquakes occurring on the same faults with partial and full ruptures. Especially in Model 2, events E, F, G, and H form a chain of events, repeating on both faults. Additionally, the duration and inter-event times vary significantly for these events.

In the SSE-dominant regime, we observe full-rupture SSEs (Event A). In contrast, in the earthquake-dominant regime, SSEs are limited in extent (Events F and G), resulting in fewer moments released by SSEs in the total catalog.

By increasing fault width, the increased interaction between the faults results in larger stress perturbations, which in turn lead to more frequent earthquakes dominating the sequence of slip events. However, the interaction strength is also controlled by other geometrical parameters L, D and L_f. We discuss the effect of other geometrical parameters in Section 4.1.
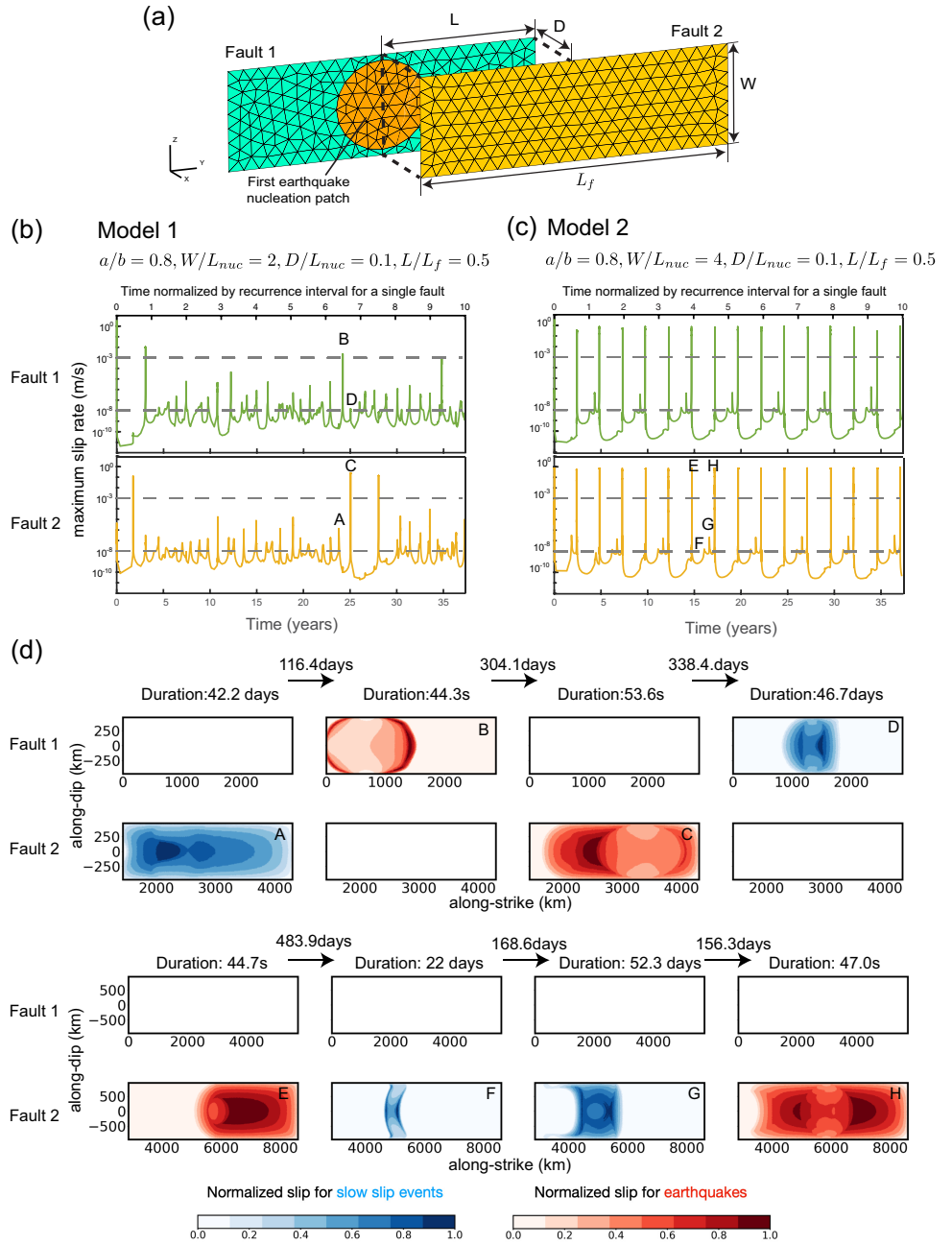
Figure 3.1: (a) Step-over fault configuration. Discrete mesh grids are exaggerated (b-c) Example of SSE-dominant regime and earthquake-dominant regime: Time evolution of maximum slip rate. The green curve is on fault 1, and the yellow curve is on fault 2. Grey dash lines are slip rate threshold for earthquakes and slow slip events (d) Spatial distribution of normalized slip for slip sequences with selected Events A, B, C, D in simulation showing in (b) and E, F, G, H in simulation showing in (c). Blue represents slow slip events, and red represents earthquakes. Event A is a slow slip event with full rupture. Events D, F, and G are slow slip events with partial rupture. Events B and E are earthquakes with partial rupture. Events C and H are earthquakes with full rupture. The red and blue color shows normalized slip for earthquakes and slow slip events. Normalize slip is defined as $(u - u_{min})/(u_{max} - u_{min})$.

3.3.2   Moment-duration scaling law

We perform seismic cycle simulations with various geometric and friction parameters. We generate an extensive dataset in which slip events span several orders of magnitude in rupture area, slip, moment, and duration.

In the fault system that is discretized with N elements, moment M for one event is given by

$$M = \mu \int_0^T \left(\sum_{i=1}^N V_i(t) A_i \right) dt, \tag{3.3}$$

where V_i and A_i are the slip rate and the area for corresponding ith element respectively, and T is the duration for this event.

We analyzed slip sequences from each simulation over an equivalent time period (the duration required for a single fault to have 10 earthquakes). We generated moment-duration scaling plots for both slow slip events (SSEs) and earthquakes (EQs), revealing different scaling behaviors: earthquakes exhibit cubic scaling, whereas SSEs follow linear scaling. See Figure 3.2.

Our findings indicate that the scaling of slow slip events (SSEs) is significantly influenced by the criteria used to define them. Specifically, lower slip rate thresholds for identifying SSEs result in a higher number of detected events, with both the duration and moment of each event increasing accordingly. This variability can alter the scaling relationship between moment and duration. For instance, using a threshold of 10^{-8} m/s, we identified 1925 SSEs with a scaling relationship of $M \sim T^{1.2}$. However, when the threshold was increased slightly to 10^{-6} m/s, the number of detected SSEs decreased to 640, and the scaling relationship adjusted to $M \sim T^{1.5}$. Notably, cubic scaling behavior was observed for large SSEs. This highlights the sensitivity of SSE detection and scaling to the chosen slip rate threshold, underscoring the importance of consistent event definition in studies of SSE dynamics.

In the 2D step-over models discussed by Romanet et al. (2018), the scaling relationship appears insensitive to the slip rate threshold for both SSEs and earthquake identification. However, our 3D simulations introduce greater complexity to the model, revealing a sensitivity to the slip rate threshold for SSEs. This may explain the observed variations in scaling relationships for SSEs in real-world observations.
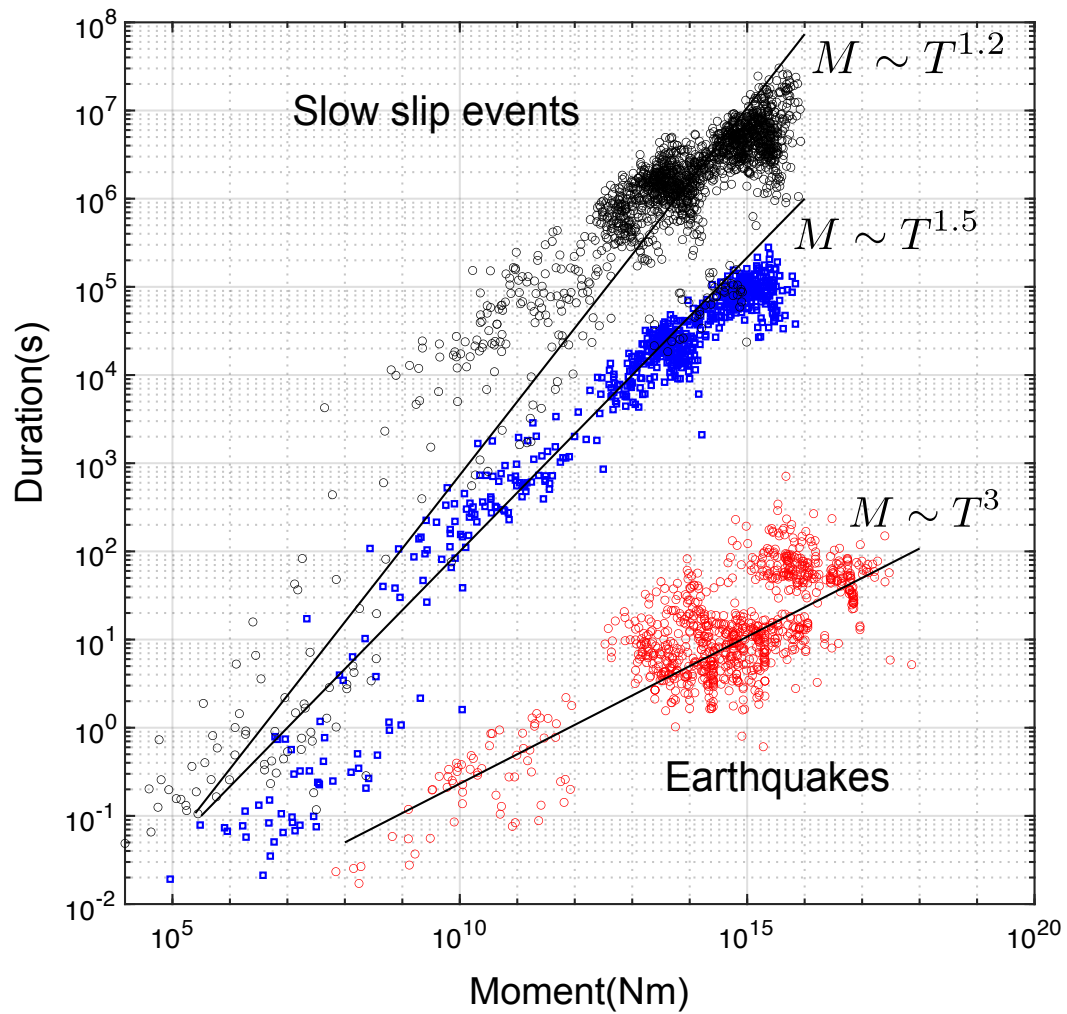
Figure 3.2: Moment-Duration scaling across all simulations. Red denotes earthquakes exhibiting cubic scaling. Blue and black represent slow slip events identified with slip rate thresholds of $10^{-6} m/s$ and $10^{-8} m/s$, respectively, showing varying but predominantly linear scaling from $M \sim T^{1.5}$ to $M \sim T^{1.2}$.

(a)

(b)
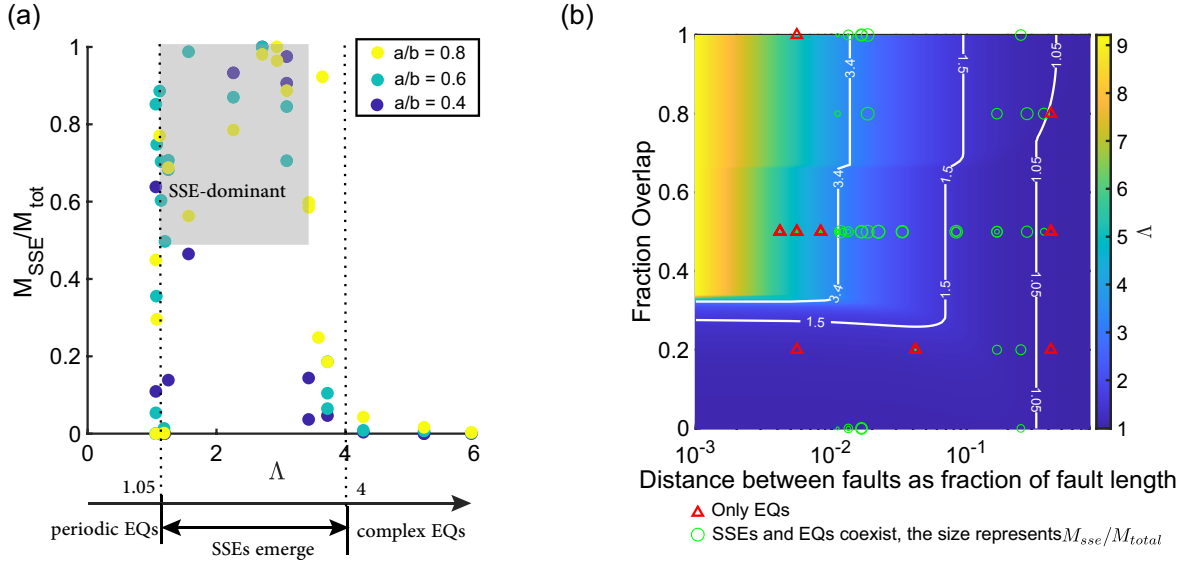
Figure 3.3: (a) The relationship between the fault interaction metric Λ and the SSEs ratio. Different colored dots represent various friction parameters a/b. The dashed lines indicate that SSEs emerge within a specific range of Λ. The grey area shows the results with the SSE-dominant slip catalog. (b) Fault interaction metric Λ as a function of overlap and the distance between two faults, expressed as a fraction of the fault length. The positions of the symbols represent the geometrical configurations in our simulations. Red triangles indicate simulations with only earthquakes, while green circles indicate simulations with coexisting SSEs and EQs, with the size of each green circle corresponding to the SSEs ratio.

3.4 Discussion

3.4.1 The metric of fault interaction and SSEs ratio

The coexistence of slow slip events (SSEs) and earthquakes (EQs) is significantly influenced by stress perturbations from neighboring faults. When these interactions are considered in a three-dimensional context, the complexity increases notably. Currently, there is no quantified approach to explain how geometrical complexities—such as overlap distance (L), distance between faults (D), and fault dimensions (width W and length L_f)—control the coexistence of slow and fast earthquakes. In this study, we introduce a new metric, Λ, to quantify the maximum stress interaction on a secondary fault due to a primary fault. This metric is geometrically derived and inspired by fracture mechanics, assuming a unit stress drop and 2D framework. We utilize Muskhelisvili-Kolosov complex potentials (Muskhelishvili et al., 1953) to

obtain full-field solutions for cracks, making Λ a function of all relevant geometrical parameters. $\Lambda = f(L, D, W, L_f)$ as derived in Appendix 3.A. The actual interaction between two cracks is linearly proportional to the average stress drop.

$$\Lambda = \max \left\{ -2\Im\left[\Phi'(z)\right] - 2y\Re\left[\Phi''(z)\right] + 2f_s y \Im\left[\Phi''(z)\right] \right\}, \tag{3.4}$$

where $f_s = 0.6$, $z \in [x_1 + iD, x_2 + iD]$ and $x_1 = (2L-1)L_f/2$, $x_2 = x_1 + L_f$ and L is the overlap.

For $\Lambda = 0$, indicating no interaction, two faults are very far from each other and behave independently. For $\Lambda \to \infty$, indicating strong interaction, the faults are very close to each other, resulting in significant interaction. We quantified the distribution of seismic and aseismic slip in the simulation results using the SSEs ratio η, which represents the proportion of moment released by SSEs to the total moment released in the slip catalog over ten earthquake cycles for a single fault with the same friction properties.

When $\eta = 0$, there are only earthquakes; when $\eta = 1$, there are only slow slip events. SSEs and EQs coexist when the $0 < \eta < 1$. Specifically, SSEs are dominant when $0.5 < \eta < 1$, whereas EQs are dominant when $0 < \eta < 0.5$.

Our results indicate that geometrical parameters significantly influence the distribution of seismic and aseismic slip (Figure 3.3a). When Λ is either too low ($\Lambda \lesssim 1$) or too high ($\Lambda \gtrsim 4$), faults predominantly host earthquakes. At the left boundary, $\Lambda \approx 1$, the primary controlling factor is the distance between two faults (D). Since Λ is roughly proportional to $1/\sqrt{D}$, the SSE ratio drops rapidly as Λ approaches this boundary. At the right boundary, $\Lambda = 4$, fault width (W) is the main controlling factor. With Λ being roughly proportional to $\sqrt{W}$, the SSE ratio decreases slowly as it nears this boundary. The low Λ values result in periodic earthquakes, while high Λ values lead to complex earthquakes.

However, when Λ falls within an intermediate range ($1 < \Lambda < 4$), both earthquakes and SSEs can coexist. Within a more specific range ($1.5 < \Lambda < 3.4$), SSEs dominate, shown in the grey area in Figure 3.3a. This is because SSEs are highly sensitive to minor stress perturbations, as noted by Obara and Kato (2016). A proper range of interaction is essential to favor slow slip events (SSEs). If the interaction is too weak, the stress perturbation is insufficient to generate SSEs. Conversely, if the interaction is too strong, SSEs cannot be sustained and will grow into earthquakes.

We also tested different friction parameters (see Figure 3.3a with different colors). For high values of a/b, a slightly wider range of geometrical parameters needs to be considered to identify SSE-dominated regimes. Despite these variations, geometry remains the primary controlling factor. The SSE ratio can potentially be

inferred from these geometrical parameters. This framework provides a mechanical interpretation of how different types of slip events are distributed based on fault geometry.

For a given Λ, various combinations of geometrical parameters can yield the same value. Figure 3.3b illustrates Λ as a function of the overlap and the distance between two faults, expressed as a fraction of the fault length. The value of Λ decreases rapidly with increasing distance between the faults. Λ increases with greater overlap, but when the distance between the two faults is larger, the effect of overlap becomes less significant. Figure 3.3b demonstrates these possible combinations. Most of our simulation results, which feature the coexistence of SSEs and EQs, cover possible combinations where $1 < \Lambda < 4$. When the geometrical configuration approaches the lower and upper Λ threshold boundaries ($\Lambda = 1, \Lambda = 4$), the SSE ratio gradually decreases and transitions to only earthquakes. This provides a comprehensive view of how different geometrical configurations influence fault interactions and the coexistence of SSEs and EQs. Additionally, it helps us select appropriate geometrical parameters based on the SSE ratio.

This study highlights the critical role of geometrical parameters in understanding and predicting complex slip behavior emerging from fault interaction. The metric Λ can be easily extended to other fault systems by modifying the geometry of the second fault. For example, the second fault can be slightly oriented or have roughness. Future research should focus on refining these metrics and exploring additional realistic geometrical parameters to enhance further our understanding of the interplay between slow and fast earthquakes in complex fault systems.

3.4.2   Traction asperities

Notably, our study is based on faults with spatially uniform rate-weakening friction conditions. Previous studies (Lay et al., 2012; Veedu and Barbot, 2016) used the single planar fault and demonstrated that slow slip events emerge in small asperities with rate-weakening friction and earthquakes occur in large asperities with rate-weakening friction within the context of friction asperities. Those friction asperities are spatially and temporally stable. Here, we introduce the concept of traction asperities, which naturally arise from multiple fault systems due to stress interactions and the history of events. These asperities can also determine the nucleation and arrest of both slow and fast earthquakes.

Due to stress interactions from neighboring faults and previous ruptures, the traction field exhibits spatial and temporal heterogeneity, as shown in Figure 3.4.

We observe the evolution of the traction field on fault 2 during four events (E, F, G, and H) in Model 2. Nucleation occurs at regions with a high ratio of shear traction to normal traction asperity (HRA). When the HRA is narrow, nucleation fails to propagate dynamically within a single asperity, potentially leading to aseismic events (e.g., Events F and G). Conversely, regions with a low ratio of shear traction to normal traction (LRA) possess higher strength and act as barriers to arrest events nucleated from the HRA. For example, after nucleation, Event E prefers to propagate towards the right HRA and arrests at the left LRA, resulting in a partial rupture. Same for Events F and G, rupture arrests at LRA. The heterogeneity of traction asperities complicates the nucleation processes. The coalescence of slip fronts and relatively homogeneous traction fields may lead to full rupture earthquakes, as observed in Event H.

3.4.3   Compare with 2D models

Compared to the 2D method used in Romanet et al. (2018), our 3D method does not rely on the assumption of a fixed rupture depth of 1 km when calculating the moment to reproduce scaling laws. Because the 2D model lacks the third dimension, they have to assume the length in that dimension, which is totally arbitrary. The 3D method allows for a more accurate understanding of scaling relationships. Our results show that moment-duration scaling is sensitive to the slip rate threshold for slow slip events, a sensitivity that previous 2D models did not reveal.

3.4.4   Comparison with a single planar fault with heterogeneous friction properties

In this work, we focus on a fault system with two parallel faults and examine the stress interaction between them, leading to a spatio-temporal complex stress field that causes slow slip events and earthquakes with partial and full ruptures. This complexity arises from the dynamic interaction of the faults and their rupture history rather than from fixed fault parameters. In contrast, models focusing on friction heterogeneity, such as those by Dublanchet et al. (2013) and Kaneko et al. (2010), suggest that variations in frictional properties can significantly influence seismic behavior. However, friction heterogeneity is static once set and does not evolve over time and space, requiring parameter adjustments, such as changes in the sizes, densities, and distances of asperities, to match the observed complexity. Our model demonstrates that simple geometric configurations, like two parallel faults, can naturally
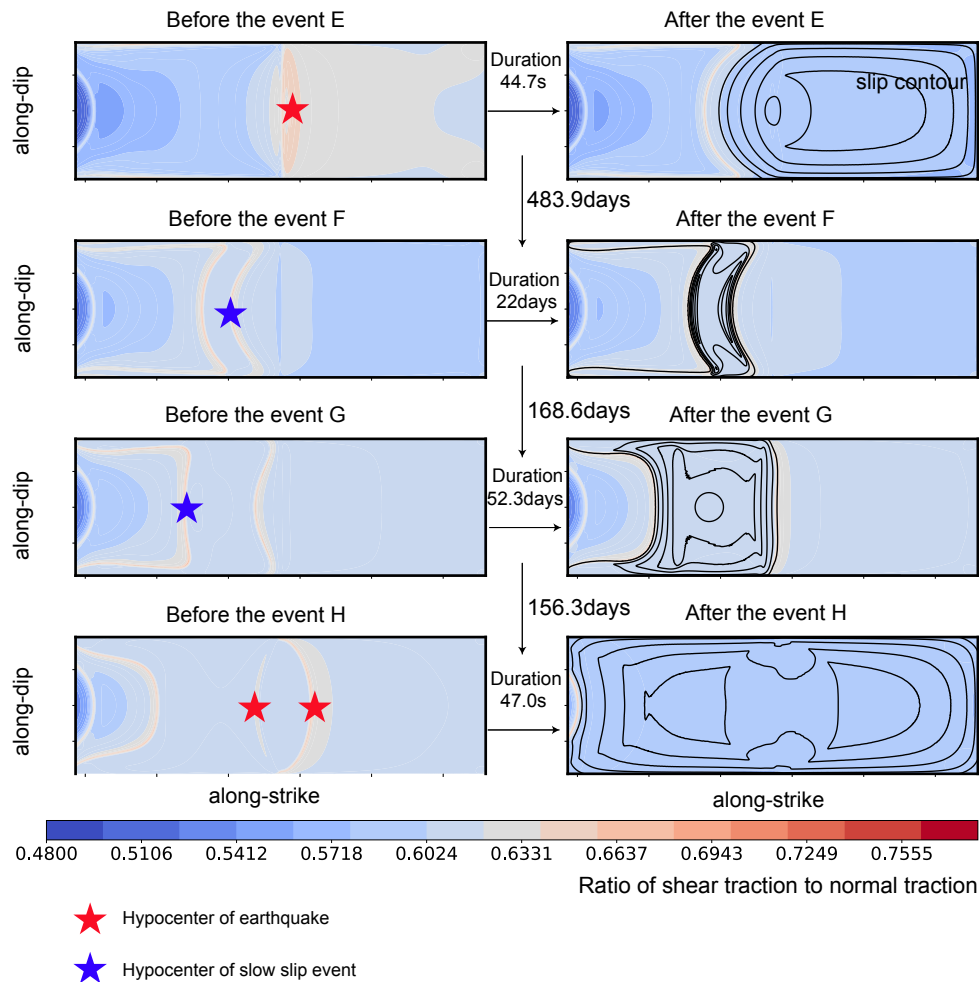
Figure 3.4: Traction field evolution during four events (E, F, G, and H) on fault 2 in Model 2. The colormap indicates the ratio of shear traction to normal traction. The first column displays the traction field before the nucleation of each event, with red stars marking earthquake hypocenters and blue stars indicating SSE hypocenters. The second column shows the traction field after each event, with black contour lines representing the slip distribution. The duration of each event and the inter-event times are noted.

produce a wide range of moment-duration laws and complex nucleation patterns, closely mimicking natural seismic and aseismic slip events. Geometric features can be more readily measured using methods like surface rupture tracing and seismic imaging, offering a practical advantage over frictional measurements. Thus, while both geometric complexity and frictional heterogeneity contribute to understanding seismic events, geometric complexity provides a more robust and dynamically evolving framework. Future research should integrate these mechanisms to refine predictive models and enhance our understanding of complex slip events.

3.5   Conclusion

In this study, we investigate the emergence of complex slow and fast seismic events driven by elastic interactions and heterogeneous stress fields over multiple earthquake cycles within a 3D fault system with two parallel planar faults. We aim to understand how the complex, multi-segmented geometry of this 3D fault system influences slip dynamics. We use a 3D quasi-dynamic earthquake cycle model with a boundary element method accelerated by Hierarchical matrices (Cheng et al., 2024b). For a single isolated fault under spatial uniform rate-weakening friction, regular earthquakes occur if the fault length exceeds the nucleation length. However, when considering the interaction between two faults, spatio-temporal complex slip events emerge due to the stress interaction from the neighboring fault. Various slow slip events, as well as earthquakes having partial or full ruptures, are identified in the slip catalog. We systematically investigate how geometrical and frictional properties influence these complex seismic and aseismic sequences. By incorporating interactions from the third dimension, our model allows for a broader range of parameters that support the coexistence of earthquakes and slow slip events compared to 2D models. For Moment-Duration scaling of slow slip events, there has been an ongoing debate in observational studies regarding the cubic and linear scaling relations. Our numerical results suggest that slow slip has linear scaling, but the scaling relation may heavily depend on the chosen slip rate threshold for identifying slow slip events.

Appendix 3.A The definition of fault interaction metric Λ

The Muskhelisvili-Kolosov complex potentials for a shear crack of length $2a$ are given by Scheel et al. (2021)

$$\Phi'(z) = -\frac{1}{2i}\left[\frac{z}{(z^2-a^2)^{1/2}} - 1\right] \tag{3.5}$$

$$\Phi''(z) = \frac{1}{2i}\left[\frac{-a^2}{(z^2-a^2)^{3/2}}\right] \tag{3.6}$$

$$\Psi'(z) = -2\Phi'(z) - z\Phi''(z). \tag{3.7}$$

The stress field is then given by $\sigma_{ij}(z) = \sigma_{ij}^0 + \Delta\sigma_{ij}(z)$ where

$$\Delta\sigma_{22}(z) = 2y\Im\big[\Phi''(z)\big] \tag{3.8}$$

$$\Delta\sigma_{12}(z) = -2\Im\big[\Phi'(z)\big] - 2y\Re\big[\Phi''(z)\big], \tag{3.9}$$

where $\Re$ and $\Im$ correspond to the real and imaginary parts of their arguments, respectively. Length $2a$ is the minimum value of fault length L_f and fault width W. The complex coordinate of fault 2 is denoted as z.

Fault 1 spans from $(-L_f/2, 0)$ to $(L_f/2, 0)$. Fault 2, on the other hand, extends from (x_1, D) to (x_2, D), where $x_1 = (2L-1)\cdot(L_f/2)$, $x_2 = x_1 + L_f$ and L is the overlap.

We define the metric Λ as the maximum of $\Delta\sigma_{12} + f_s\Delta\sigma_{22}$ on fault 2. This metric, which is a function of all geometrical parameters, quantifies the strength of the stress interaction between the two faults:

$$\Lambda = \max\left\{-2\Im\big[\Phi'(z)\big] - 2y\Re\big[\Phi''(z)\big] + 2f_sy\Im\big[\Phi''(z)\big]\right\}. \tag{3.10}$$

Chapter 4

Discussions and Perspectives

In this manuscript, I have presented the 3D slip sequence model using the boundary element method accelerated by Hierarchical matrices (Chapter 2). We validated this method with analytical solutions for static cracks and numerical benchmarks for a dynamic fault problem (Chapter 2). We also explored a fundamental geometric complexity: the step-over fault configuration (Chapter 3). In this chapter, we will delve into a comprehensive discussion. Additionally, we will outline future perspectives, highlighting potential developments and directions for further research and exploration.

4.1 General discussion

4.1.1 Frictional heterogeneity and geometrical heterogenity

The observation of spatio-temporal complex events highlights the diversity of seismic and aseismic slip behaviors. Slow slip events (SSEs) can last from hours to several years, contrasting with earthquakes, which typically last only seconds to minutes. The moment, duration, and nucleation location for events vary significantly. SSEs can occur in the seismogenic zone as well as at shallow and deep depths, underlying the inherent spatial-temporal complexity of slip behaviors.

Traditional models of seismic cycles have focused on friction heterogeneity to produce spatio-temporal complexities of slip events. Variations in frictional properties along the fault plane significantly influence fault behavior, leading to the localization of stress and variations in slip distribution. These factors are critical for understanding earthquake nucleation and propagation. Kaneko et al. (2010) showed

that friction heterogeneities can provide a unifying explanation for various observations of fault behavior, detectable through geodetic observations of interseismic coupling. Dublanchet et al. (2013) focus on a numerical 3D model with friction asperities, where velocity-weakening patches primarily host fast, seismic ruptures and are surrounded by velocity-strengthening patches that exhibit more stable, aseismic slip behavior. He examined the interaction among friction asperities, producing complex seismic processes by controlling the density of asperities. Luo et al. (2017) investigated the diversity of slip behaviors, generating a full spectrum of fault behaviors by controlling the proportion of velocity-weakening and velocity-strengthening materials, their relative strength, and other frictional properties. However, friction heterogeneity is static once set. It does not evolve over time and space, requiring many parameter adjustments, such as changes in the sizes, densities, distances, and strengths of friction asperities, to match the observed slip complexity. There are also studies that use friction to address complex events in observation. The 2004 Mw 9.2 Sumatra-Andaman, 2010 Mw 8.8 Chile, and 2011 Mw 9.0 Tohoku great earthquakes exhibited similar depth variations in seismic wave radiation. This phenomenon can be explained by considering depth variations in fault frictional strength (Lay et al., 2012).

One key aspect of nature is that faults have complex structures. Geological observations reveal that fault structures are geometrically complex across multiple length scales, featuring damage zones, roughness, bends, branches, and step-overs. These geometric complexities significantly affect earthquake behavior. Examples include the Landers earthquake (Sowers et al., 1994), the Kaikōura earthquake (Klinger et al., 2018), and the Ridgecrest earthquake (Nevitt et al., 2023), as discussed in Chapter 1. Numerical studies also emphasize the importance of geometric complexity. For instance, Cattania and Segall (2021) analyzed the precursory slow slip and foreshocks on rough faults, Ozawa and Ando (2021) reproduced realistic spatiotemporal aftershock activities on a rough main fault surrounded by numerous subsidiary faults, and Ozawa et al. (2023) quantified the likelihood of rupture arrest occurring at fault bends. Li and Liu (2016) studied the spatiotemporal evolution of SSEs using nonplanar fault models in the Cascadia region.

Our study in Chapter 3 focuses on the effect of 3D fault geometry on earthquake cycles. By considering the interaction between two parallel faults, a spatio-temporal complex heterogeneous stress field is naturally generated. Even with a simple geometrical complexity, complex events with various SSEs and earthquakes of different sizes and durations emerge. Rupture nucleation and arrest can significantly modify the stress field, further promoting slip complexity. The complexities produced in our model arise from the stress interaction of faults and their rupture history rather

than fixed fault parameters. The formation of traction asperities or stress barriers that evolve over time and space could account for partial rupture and SSEs, with nucleation along the fault varying depending on the temporal evolution of these stress barriers.

Measuring friction properties presents greater challenges compared to assessing geometric complexities. Fault complexities can be directly measured through geological field studies (Mitchell and Faulkner, 2009) and indirectly through seismological studies and geodetic measurements. In contrast, friction parameters are typically derived from laboratory experiments, which are influenced by various conditions such as temperature (Blanpied et al., 1995), normal stress (Carpenter et al., 2016), and fluid pressure (Scuderi and Collettini, 2016). In numerical modeling, the spatial variation of friction parameters is often determined based on depth-dependent temperature and composition. However, it is debatable whether the rate-and-state friction (RSF) parameters derived from these experiments can adequately describe the full seismic cycle, including all transient features observed in nature. For instance, friction is velocity-dependent and exhibits behaviors such as transitioning to velocity strengthening at high velocities and coseismic dynamic weakening due to friction heating (Di Toro et al., 2011). Friction parameters change throughout earthquake cycles and with fluid injection (Scuderi and Collettini, 2016), yet incorporating all these physical mechanisms into models remains challenging.

In addition to laboratory experiments, macroscopic physical models can also estimate parameters such as friction parameter a (direct effect) and b (evolution effect) and characteristic slip distance D_c, taking into account their velocity dependence (Chen et al., 2017). The parameter $(a - b)\sigma_n$, where σ_n is the normal stress, can be estimated from postseismic slip using inversion of geodetic data (Thomas et al., 2017). However, these postseismic slip estimates rely heavily on the resolution of kinematic inversion and necessitate accurate estimation of normal stress. Moreover, this approach is applicable only under velocity-strengthening friction conditions, where $a > b$.

Robust empirical laws emerging from seismological observations reinforce the need to consider heterogeneity in models, whether frictional or geometric. Both mechanisms—frictional heterogeneity and geometric complexity—can produce similar complexities of events. Friction asperities correspond to traction asperities. In friction models, earthquakes often nucleate from velocity-weakening (VW) patches, and ruptures are impeded when they propagate into velocity-strengthening (VS) patches. Similarly, in geometric models, earthquakes nucleate from high traction rate patches and are impeded by low traction rate areas. When two friction asperities are close enough, multiple asperities interact, leading to the formation of

a larger earthquake (Johnson, 2010; Dublanchet et al., 2013). This phenomenon is also observed in geometric heterogeneity models, where the rupture can propagate through adjacent traction asperities, causing coalescence and resulting in a larger earthquake. Both friction and geometry can produce aperiodic behavior, but achieving this with friction models requires more adjustments and incorporation of physical mechanisms, as friction asperities are fixed in time and space. Our work shows that even with simple geometric heterogeneity, such as two parallel faults, we can achieve significant complex behavior.

While friction is important and recognized as heterogeneous, our research suggests that geometric complexities may play a more critical role— a factor often overlooked in current studies. Although future work should incorporate friction, our two-fault model achieves similar results without explicitly considering frictional heterogeneity or fluid presence, indicating that geometric complexity alone can effectively explain complex slip behaviors.

In conclusion, it is crucial to consider both frictional heterogeneity and geometric complexity in earthquake cycle simulations. Future research should emphasize a more integrated approach to studying slip behaviors, combining these two factors to achieve a comprehensive understanding of realistic earthquake sequences. Our method, FASTDASH, allows for straightforward implementation of friction heterogeneity.

4.1.2 Comparison of model in 2D and 3D

Most numerical models involving geometrical complexities are conducted using a two-dimensional plane strain assumption to avoid the high computational costs associated with 3D modeling. Traditionally, accelerating 3D models have relied on Fast Fourier Transform (Lapusta et al., 2000), which is insufficient for solving geometrically complex fault models. Our study overcomes this limitation by employing Hierarchical Matrices to accelerate the 3D modeling of seismic cycles while maintaining a complex fault geometry.

While 2D models have provided foundational insights with the advantage of computational efficiency, they cannot simultaneously consider variations along strike and depth, limiting their ability to represent 3D structures. Exploring 3D geometric complexities is time-consuming but essential for making fault models more realistic and capturing the full range of earthquake behaviors. Our 3D model demonstrates that these additional degrees of freedom lead to significant differences in stress distribution and slip behavior, emphasizing the necessity of three-dimensional analysis

for accurate fault characterization. The 3D model offers a more comprehensive representation of geological structures and fault behaviors, capturing complexities that 2D models inherently miss.

3D models provide a more realistic representation of a geological picture. Observations of fault zone structures reveal that the fault core is surrounded by a fractured damage zone, with the density of 3D fractures decreasing with distance from the fault core (Mitchell and Faulkner, 2009). Additionally, the fault zone width decreases with depth while fracture density increases, forming what is known as flower structures (Ben-Zion et al., 2003; Ma and Andrews, 2010). Numerical results from Okubo et al. (2019) support these observations. These studies of fault zone structure emphasize the necessity of 3D modeling.

Furthermore, 3D models can explain complex earthquake behaviors that 2D models cannot. For example, the 2013 Mw 7.7 Balochistan, Pakistan earthquake exhibited left-lateral motion with a reverse component on a dipping fault that 2D models fail to simulate accurately (Vallage et al., 2015). Observations of earthquake swarm processes also demonstrate that 3D geometry is critical for understanding the spatiotemporal evolution of swarms, capturing phenomena that 2D models inherently miss (Ross et al., 2020).

In summary, 3D modeling offers a more comprehensive and realistic depiction of geological and seismological observation, highlighting the importance of three-dimensional analysis for accurate fault characterization and slip events understanding, as well as statistical scaling laws.

4.1.3   Assumptions in our model

The fault geometry in our model is fixed and does not evolve with rupture. However, during earthquakes, new fractures are created, and the interaction between these new fractures and the original fault system also affects fault behavior. To accurately model this, a higher number of elements are required to discretize additional fractures, and the mesh needs to be updated to account for fracture growth. Correspondingly, H-matrices must be updated as well. Considering the evolution of the damage zone in the earthquake cycle is computationally challenging. Faults extend over several kilometers, while fracture growth occurs on the order of centimeters or even smaller. Therefore, it is reasonable to ignore such changes over relatively short time scales. However, changes in fault geometry must be addressed over long geological time scales.

Our method is quasi-dynamic and does not account for dynamic wave effects, which are crucial in fully dynamic approaches commonly used for coseismic time scales where dynamic wave effects are significant. Fully dynamic models provide detailed insights into coseismic rupture phenomena, such as the propagating rupture front, rupture speed, and supershear rupture. In contrast, in earthquake cycle modeling, the quasi-dynamic approximation significantly accelerates calculations for each time step. This is essential for simulating earthquake cycles over extended periods that require numerous time steps. This approach enables us to simulate multiple ruptures on a fault to understand how one rupture triggers another. When comparing quasi-dynamic (QD) and fully dynamic (FD) methods in 2D models, Thomas et al. (2014) found that QD models underestimate slip, slip rate, and rupture velocity compared to FD models, showing quantitative differences. Despite these differences, QD methods are widely used in the seismic cycle simulation community because they produce qualitatively similar fault behaviors, slip patterns, and sequences. Some studies, like Romanet et al. (2021), have attempted to reduce this approximation by using a Spectral Boundary Integral Equation Method (sBIEM) for a single mildly nonplanar fault. Their findings show that the zeroth-order effects of wave-mediated stress transfer are more significant than the higher-order effects of fault non-planarity. However, this method is only applicable to single, mildly nonplanar faults, whereas realistic fault geometries are often highly heterogeneous and involve multi-fault networks. Liu et al. (2019) presents a method that combines FD and QD approaches, using fully dynamic simulations during the coseismic phase and quasi-dynamic simulations during the interseismic phase. This approach requires a switching criterion and on-fault quantity transfers between codes, complicating implementation and making error quantification difficult. Quasi-dynamic simulations provide an overall view of fault behavior, complementing the detailed coseismic rupture insights from fully dynamic simulations. Each approach is used for specific purposes, depending on the goal of the study.

We use the Boundary Element Method (BEM) for our fault modeling. This method allows us to efficiently solve problems involving geometrically complex faults by assuming an elastic medium surrounding the fault planes. In contrast, volumetrically discretized models like the Discontinuous Galerkin (DG) method (e.g., Tandem (Uphoff et al., 2022)), Finite Difference (FD) method (e.g., GARNET (Li et al., 2022)), and Finite Element Method (FEM) (e.g., EQsimu (Liu et al., 2019)) can account for heterogeneous elastic properties but require significantly more computational time (Scholz, 2002). As discussed in Chapter 1, many observations support the idea that complex fault geometry is associated with complex earthquake behaviors. In order to capture long-term behavior, heterogeneous elastic properties can be ignored, allowing us to focus on fault geometry as a first-order effect on fault behavior.

The current model assumes simplified rheological behavior and neglects fluid effects. Including a more comprehensive rheological model (e.g., viscoelasticity) and considering the impact of pore fluids, especially for subduction zone models, could provide better insights into fault zone mechanics and earthquake-triggering processes.

4.2   Perspectives

In this section, we will discuss some future perspectives that can build on this work.

4.2.1   More realistic fault geometry model

Real faults often exhibit complex geometries. In Chapter 3, I presented one of the fundamental complexities of fault systems, step-overs, using a simplified model with two parallel planar faults. This work demonstrated that even simple geometries can produce complex slip events, underscoring the importance of incorporating realistic geometries in fault modeling. Natural fault networks can be decomposed into simple geometrical complexities for more detailed analysis.

Step-overs, as studied in my work, involve two parallel faults with identical geometry. However, in real fault networks, the second fault can have different orientations, and both faults can have nonplanar geometry. There are usually multiple faults in a fault network. It is also essential to consider the effects of the number of faults in the system.

Almakari et al. (2024) performed a 2D fault volume model study with a primary rough fault accompanied by off-fault fractures. These off-fault fractures follow a power-law length distribution, with fracture density decreasing with distance from the fault. This fault volume model accurately reproduces diverse slip dynamics, including slow slip events, low-frequency earthquakes, and earthquakes, all within a unified framework. Extending this work into 3D in the future could provide even more comprehensive insights.

In both Chapter 3 (step-over fault system) and Section 4.2.2 (Turkey earthquake), I focused on strike-slip faults. It would be interesting to explore dipping faults in future studies to capture a wider range of fault behaviors.

4.2.2 Realistic fault system: The 2023 Kahramanmaraş – Türkiye earthquakes

Introduction

February 6, 2023, earthquakes in Turkey, with magnitudes of Mw 7.8 and Mw 7.6, causing over 55,000 deaths and impacting around 14 million people, highlight the significance of understanding fault geometry complexities for risk assessments. The earthquake of Mw 7.8 nucleated on the Nurdağı-Pazarcık fault (NPF), a branch of the Eastern Anatolian fault (EAF), and then propagated bilaterally on EAF over 300km. With a 9-hour delay, the earthquake of Mw 7.6 occurred on the Çardak fault, which varies from 10 to 50km away from the EAF. All faults are left-lateral strike-slip faults. In this section, we simulate earthquake cycles on the fault system that can be activated in the 2023 Turkey earthquake, including NPF, EAF, and Çardak fault. For simplicity, we ignore other splay faults. We focus on the interaction among these faults.

Method

We construct our fault model (Figure 4.1) according to the discontinuous line seen in the InSAR image (Raimbault, Jolivet and Aochi, personal communication, 2024), and the dip is fixed at 90° down to 15 km. The frame is rotated clockwise by 30°, and the new Cartesian coordinates (X, Y) used in the simulations correspond briefly to the fault parallel and normal directions. Principal horizontal stress orientations are setting segmented, shown in Figure 4.1. We also smooth the orientations in order to have a reasonable range of shear and normal traction. Friction, material properties principle stress value, and stress rate are shown in Table 4.1.

Previous studies have already shown that in order to obtain the convergence of the result, the element size needs to be small enough to resolve the process zone length L_b (Rubin and Ampuero, 2005)

$$L_b = \frac{\mu D_c}{b \sigma_n}.$$
(4.1)

L_b is 2400m in this problem. We choose grid size 400m, which is $L_b/6$. This model requires 105,722 triangular elements. To solve the Turkey 2023 doublet earthquakes, we need 6500 time steps, and it will be completed in 2 hours. The rupture process and timing are shown in Figure 4.2.
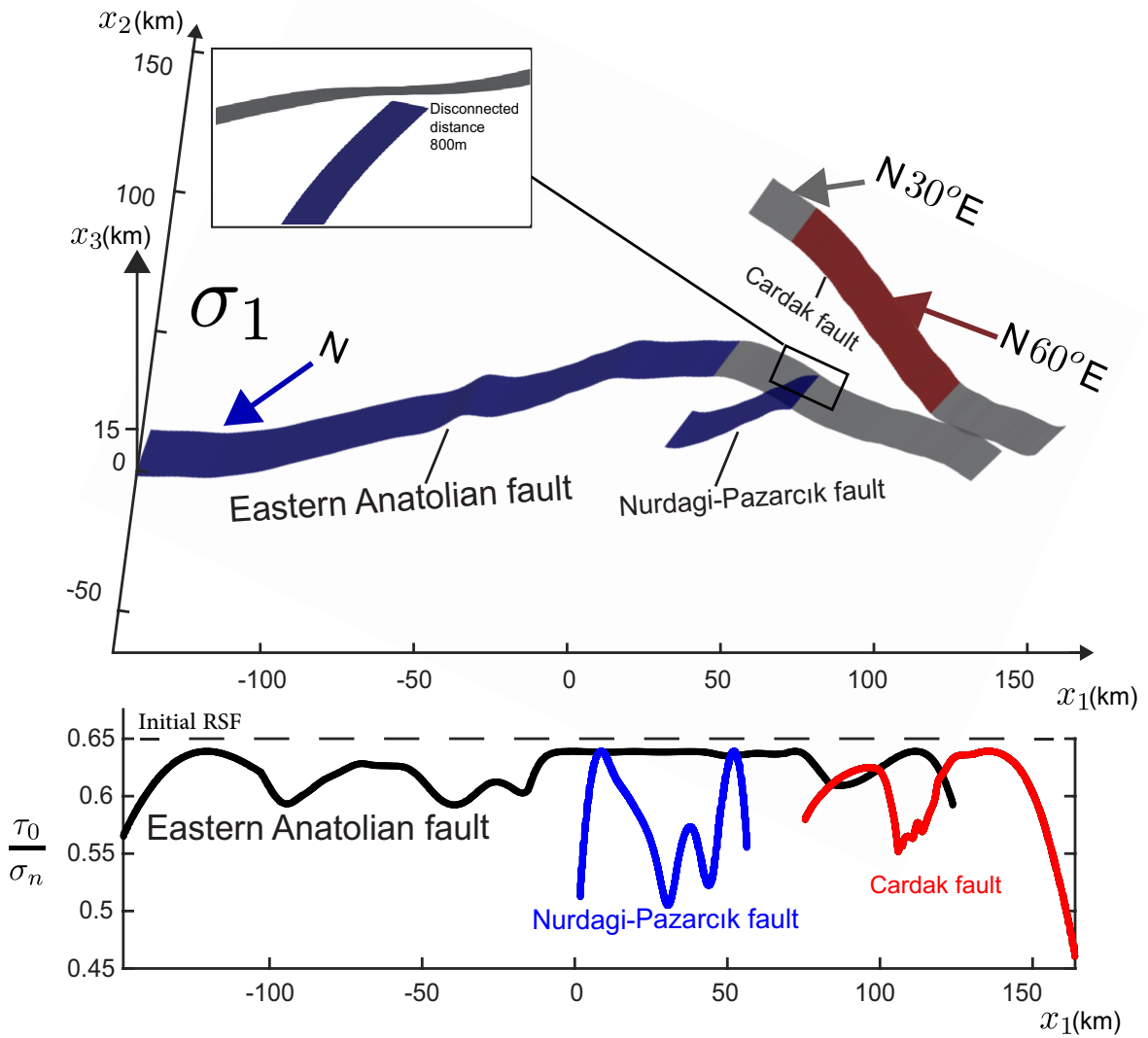
Figure 4.1: Geometry of the fault system in Turkey earthquakes and stress field setting in this study.

Table 4.1: Model and numerical parameters for the 2023 Kahramanmaraş – Türkiye earthquakes

Parameters	Description	Value
a	friction property: parameter for RSF	0.003
b	friction property: parameter for RSF	0.01
D_c	friction property: characteristic slip distance	0.04 m
V_{ref}	friction property: reference velocity for RSF	10^{-6} m/s
f_0	friction property: reference friction coefficient for RSF	0.6
μ	material property: shear modulus	3×10^{10} Pa
ρ	material property: density	2670 kg/m^3
C_s	material property: shear wave velocity	3464 m/s
V_0	initial condition: initial slip rate	10^{-9} m/s
σ_1	initial condition: maximum principle stress	100 MPa
σ_2	initial condition: vertical principle stress	50 MPa
σ_3	initial condition: minimum principle stress	30 MPa
$\dot{\sigma_1}$	initial condition: maximum principle stress rate	0.2 Pa/s
$\dot{\sigma_2}$	initial condition: vertical principle stress rate	0.05 Pa/s
$\dot{\sigma_3}$	initial condition: minimum principle stress rate	0.03 Pa/s

Result

We then simulate multiple earthquake cycles on this fault system and solve 6 earthquakes for the main faults. See Figure 4.3. It takes 68,000 time steps, and the computation is completed in one day. Our results show that earthquakes on EAF are more frequent than those on the Cardak fault and NPF. Due to the interaction between three faults, we have complex earthquake sequences in the following earthquake cycles.

Conclusion

Unlike conventional modeling approaches limited to single planar faults, this model lets us simulate how earthquakes might happen in complex fault systems, no matter how many faults or whether they are planar or nonplanar. The geometrical complexities of fault systems can be well-defined by geological and geophysical approaches. We can simulate real-world fault systems and use a physics-based model to figure out how big earthquakes might be, where they could occur, and how often. In Chapter 3, We applied this approach to the 2023 Kahramanmaraş – Türkiye earthquakes,

(a) Time = 25s

(b) Time = 1day 4hrs 12min 5s

(c) Time = 2mo 17days 19hrs 2min 51s

(d) Time = 6yrs 1mo 15days 17hrs 28min 30s

(e) Time = 6yrs 8mo 1day 4hrs 1min 52s

(f) Time = 6yrs 11mo 22day 12hrs 57min 18s

Slip rate (m/s)

10^{-9} 10^{-8} 10^{-7} 10^{-6} 10^{-5} 10^{-4} 10^{-3} 10^{-2} 10^{-1} 10^{0}
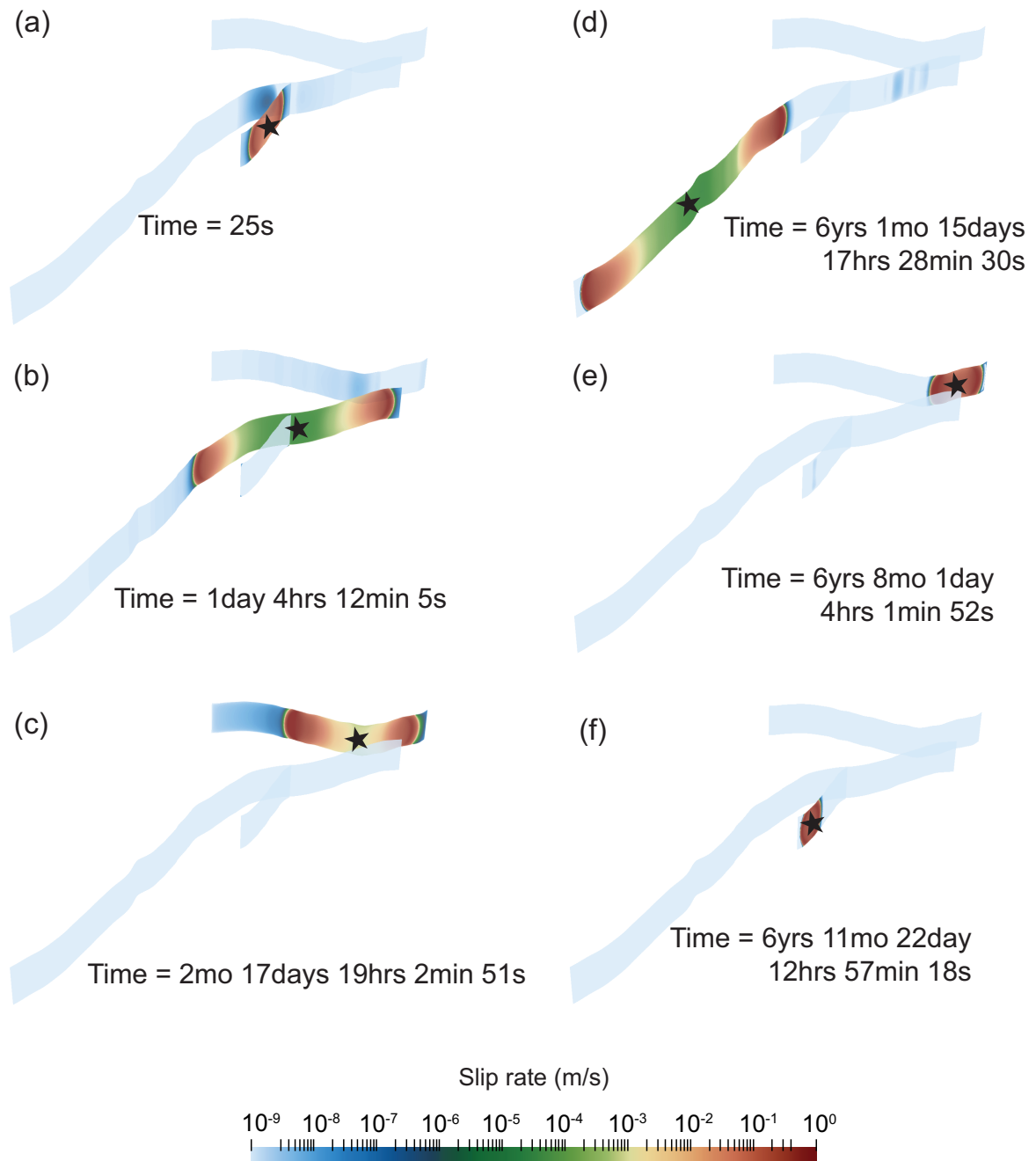
Figure 4.2: The slip rate in the Turkish model for the first and second earthquake sequences. (a)(b)(c) The first sequences rupture in the order of NPF, EAF, and Cardak fault (d)(e)(f) The second sequences rupture in the order of EAF, Cardak fault, and NPF.
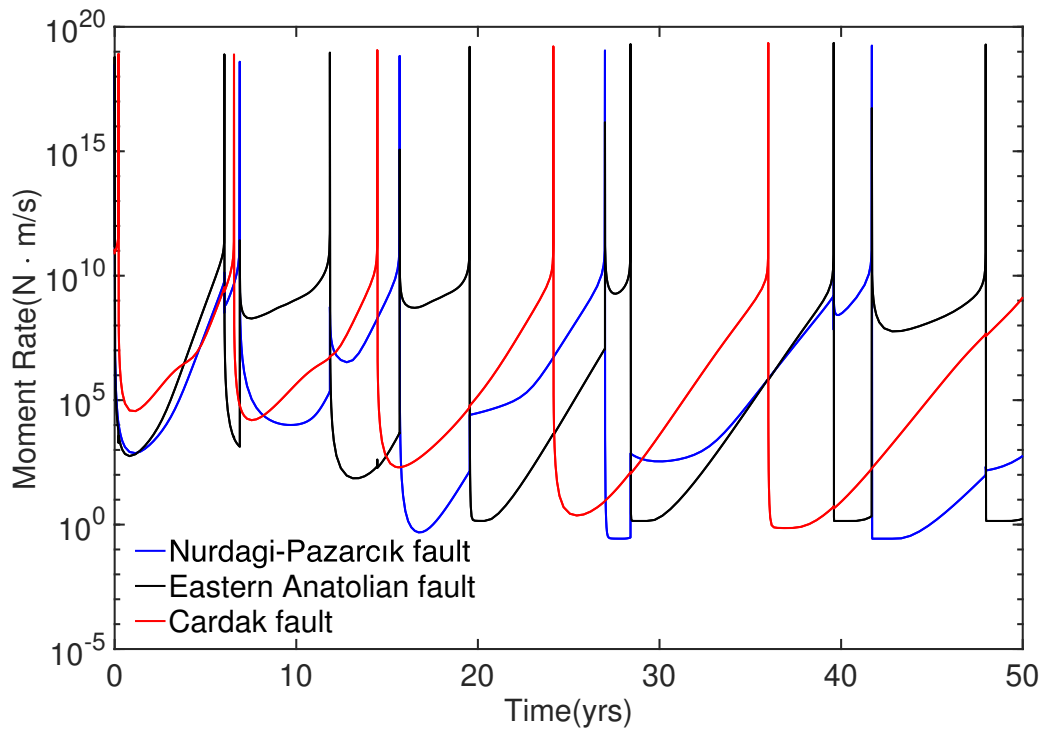
Figure 4.3: Moment rate evolution on three faults segments for 50 years.

considering how the three faults affected each other. With our innovative method, we analyzed six earthquakes in just one day—a task that would have taken around 24 days with older techniques that do not use Hmat acceleration. To get the timing right and study supershear ruptures, a fully dynamic model is needed. Our model aims to explain the complicated patterns of earthquake sequences clearly.
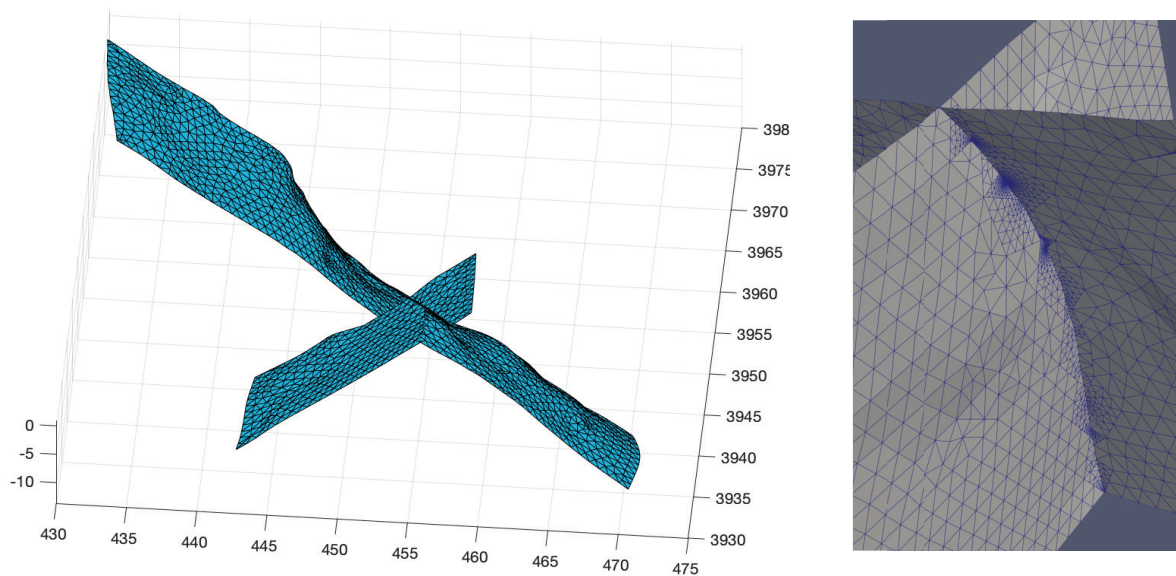
Figure 4.4: The geometry of the conjugate faults activated during the 2019 Ridgecrest earthquakes and grid handling at their intersection.

4.2.3 Realistic fault systems: The 2019 Ridgecrest earthquake and Mexico subduction zone

In the previous section, we demonstrated the effectiveness of our method using a realistic fault system, specifically the 2023 Kahramanmaraş – Türkiye earthquakes. Our approach can be effectively applied to various fault geometries, aiding in the study of real-world earthquakes. In the following sections, we will present two additional examples—the 2019 Ridgecrest earthquake and the Mexico subduction zone—to show the capability of our method.

The 2019 Ridgecrest earthquakes

We extracted the conjugate faults activated during the 2019 Ridgecrest earthquakes from the Southern California Earthquake Center (SCEC) Community Fault Model (CFM) (Plesch et al., 2007) and remeshed them in CUBIT to ensure that the two faults share the same edges and nodes at their intersection. The mesh is more refined towards the intersection between the two faults (as shown in Figure 4.4 on the right) to model the dynamics of the system at the intersection accurately.

Considering a constant stress field, the resulting shear and normal tractions on the faults are shown in Figure 4.5. This traction distribution supports right-lateral

slip motion on the longer fault and left-lateral slip motion on the shorter fault, the same as the observation. Future studies can develop more detailed models to reproduce the earthquake sequences, where a foreshock on the shorter fault triggers the mainshock on the longer fault.

Mexico subduction zone

We also simulated the real geometry of the Mexico subduction zone, which is close to Guerrero. The geometry of the subduction zone is from a personal discussion with Carlos D. Villafuerte. We got different earthquake sequences that nucleate at different positions, as shown in Figure 4.6 and 4.7. For the earthquake depicted in Figure 4.7, our observations indicate that the geometric complexities of the fault structure may influence the shape of the rupture front. Future work can focus on exploring the slow slip events in this region.

4.2.4   Loading condition and initial condition

Loading condition: plate rate and stress rate

In earthquake cycle simulations, two commonly used types of loading are plate rate loading and stress rate loading.

For plate rate loading, the backslip approach (Heimisson, 2020) is implemented in FASTDASH. This method specifies fault-slip rates and then calculates and imposes stressing rates that correspond to the specified slip rates, as shown in Equation 2.28. However, this often results in singularities in stressing rate at fault boundaries, leading to unrealistic hypocenters of events associated with these singularities. Shaw (2019) introduced a new generalized hybrid loading method that combines the ability to drive faults at desired slip rates with more regularized stressing rates, allowing faults to slip more naturally.

On the other hand, stress rate loading involves applying a constant stress loading rate aligned with the principal direction of the initial background stress tensor. This method is more accurate for complex geometries, assuming a constant stress rate in the region and allowing the shear and normal traction rate on the fault to vary with the strike.

However, there is one issue in stress rate loading, which is unrealistic stress accumulation. In Chapter 3, we use stress rate loading along the strike, as the two
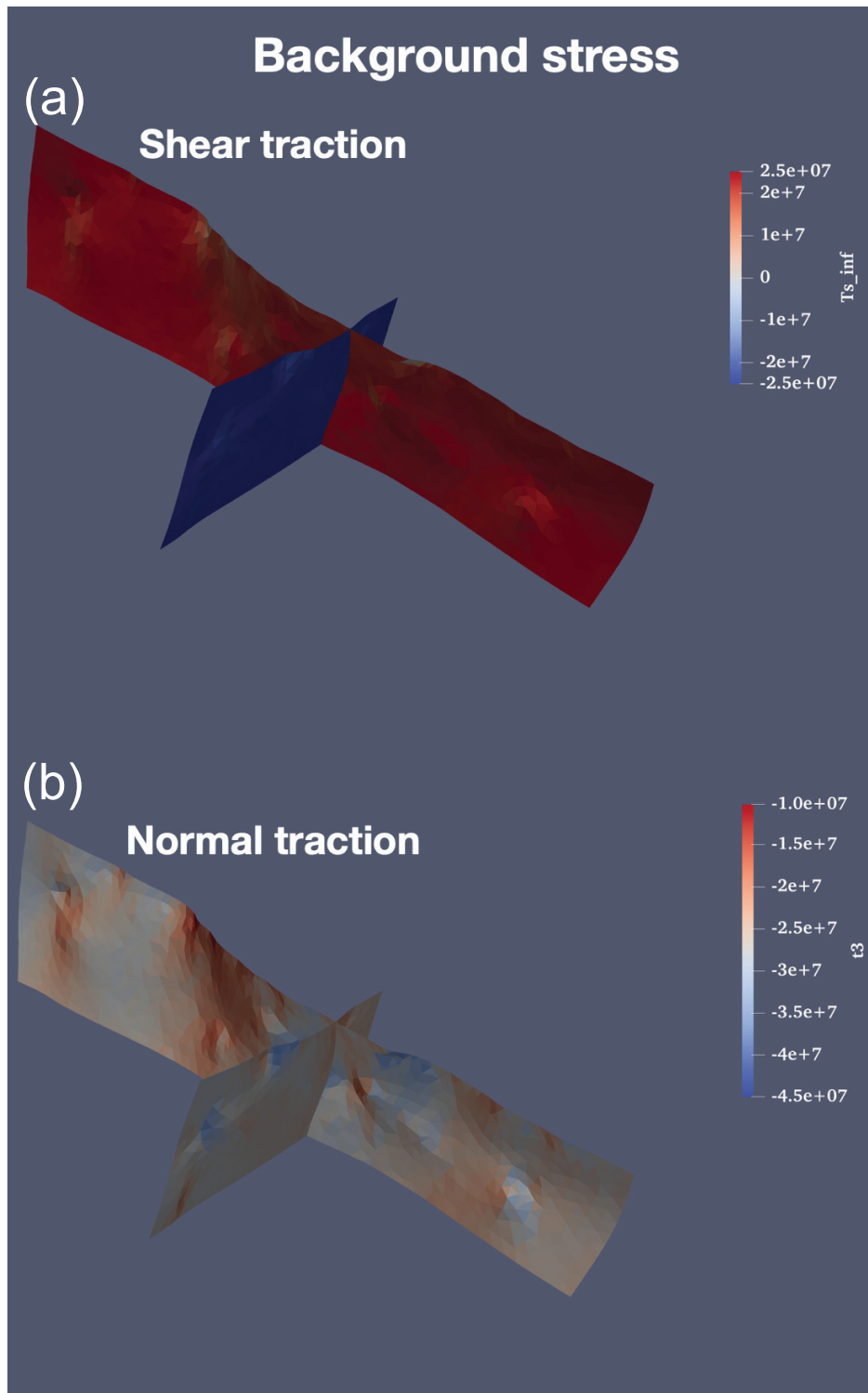
Figure 4.5: Resulting shear and normal traction distribution on the conjugate faults activated during 2019 Ridgecrest earthquakes. The units of shear traction and normal traction are both Pascal (Pa).
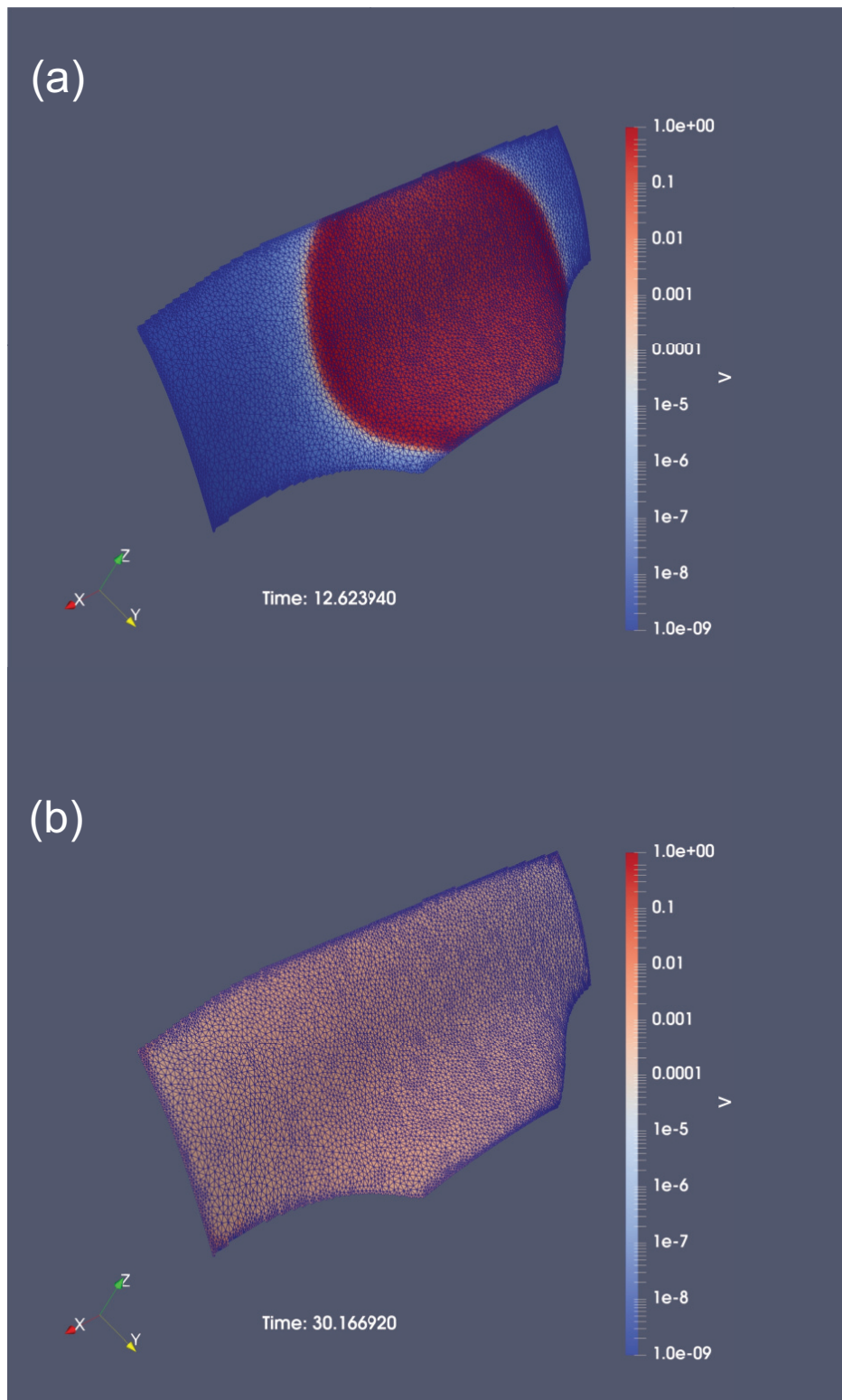
Figure 4.6: Slip rate snapshots for Mexico subduction zone simulation. One earthquake nucleated close to the center of geometry. The units of slip rates are meters per second (m/s), and the units of time are seconds (s).
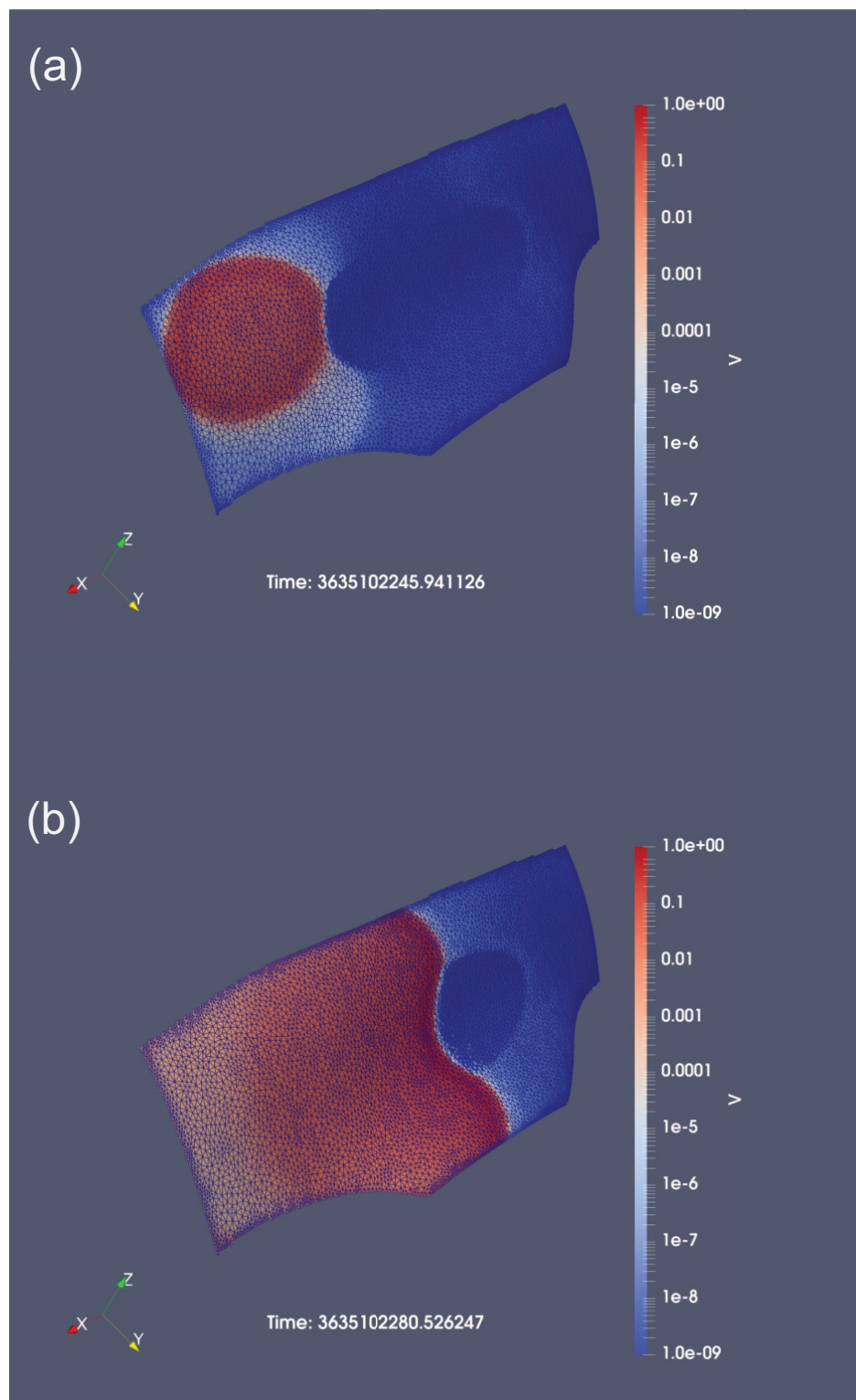
Figure 4.7: Slip rate snapshots for Mexico subduction zone simulation. One earthquake nucleated close to the top left corner of geometry. The units of slip rates are meters per second (m/s), and the units of time are seconds (s).

Table 4.2: Stress field applied to the rough fault

Parameters	Description	Value
σ_1	maximum principle stress	45 MPa
σ_2	vertical principle stress	18 MPa
σ_3	minimum principle stress	10 Mpa
ψ	angle between x-axis and maximum principle stress	45°
$\dot{\sigma_1}$	maximum principle stress rate	0.0045 Pa/s
$\dot{\sigma_2}$	vertical principle stress rate	0.0018 Pa/s
$\dot{\sigma_3}$	minimum principle stress rate	0.0001 Pa/s

faults are planar, and there is no unrealistic normal traction accumulation on the faults. Earthquakes and slow slip events will release the shear stress accumulation. In Section 4.4.2, concerning the Turkey case, there is a strike variation, and we observe normal traction increasing with time, which slightly increases the recurrence intervals of earthquakes. Since the time scale is not too long, the normal traction remains reasonable. However, if the simulation time scale is extended significantly, the normal traction accumulation could become excessively high, particularly in a complex fault system.

Here, we provide an example with a rough fault to illustrate this issue. We focus on a 3D sinusoidal rough fault, with the stress field information detailed in Table 4.2. A heterogeneous traction distribution on the fault plane is shown in Figure 4.8. The results in Figure 4.9 demonstrate that the recurrence interval increases over time due to the rapid accumulation of both shear and normal traction on the faults, which is unrealistic in nature. The surrounding material cannot support excessively high normal stress and will eventually exhibit plastic behavior, which our model cannot capture.

One way to address this issue is to set a yield limit for normal stress. Once the normal stress reaches a certain threshold, it is capped at this yield value. However, this approach can lead to the loss of normal traction interactions in complex geometries. Alternatively, we can apply a time-dependent relaxation term for both shear and normal stresses. This relaxation term approximates the viscoplastic behavior of off-fault materials and can be defined as follows (Ozawa et al., 2023):

$$\frac{d\tau}{dt} = -\frac{\tau - \tau_0(s)}{t_{relax}} \tag{4.2}$$

$$\frac{d\sigma}{dt} = -\frac{\sigma - \sigma_0(s)}{t_{relax}}, \tag{4.3}$$
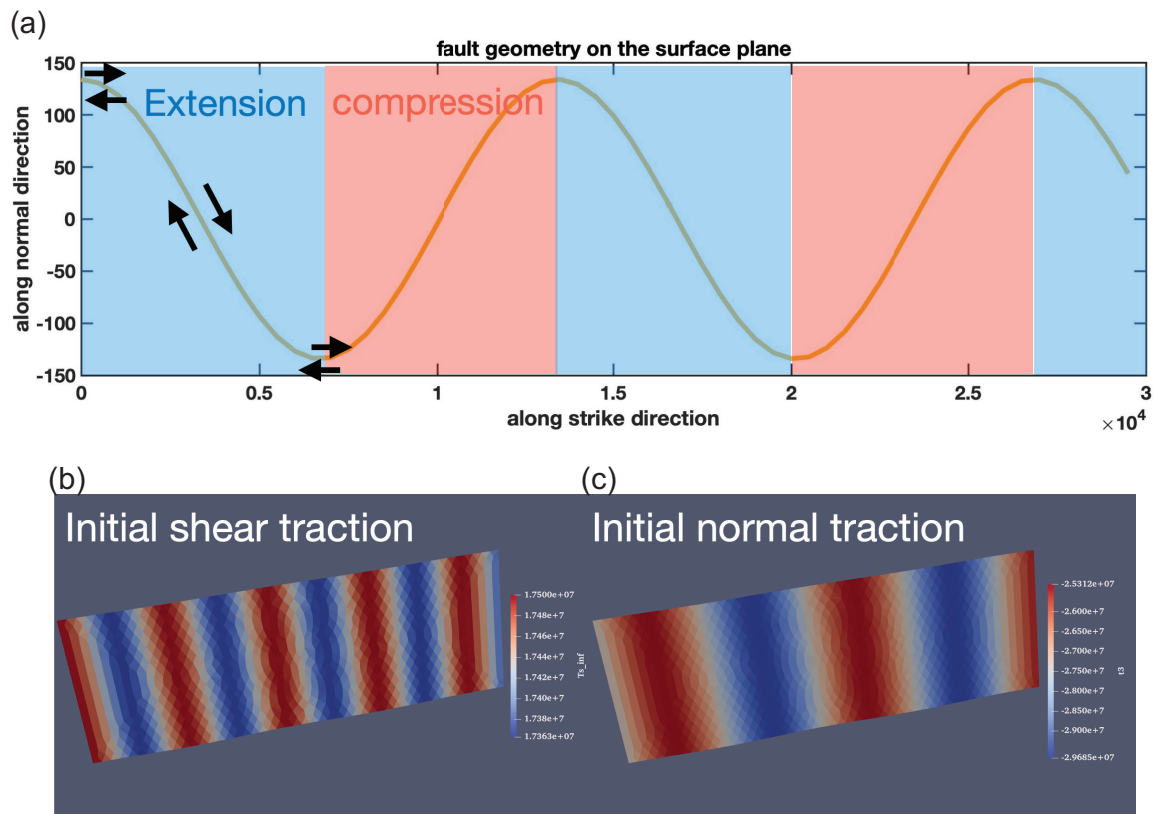
Figure 4.8: Geometry of sinusoidal rough fault and initial condition. The units for a distance along strike direction and along normal direction are meters (m). The units for initial shear and normal traction are Pascal (Pa).
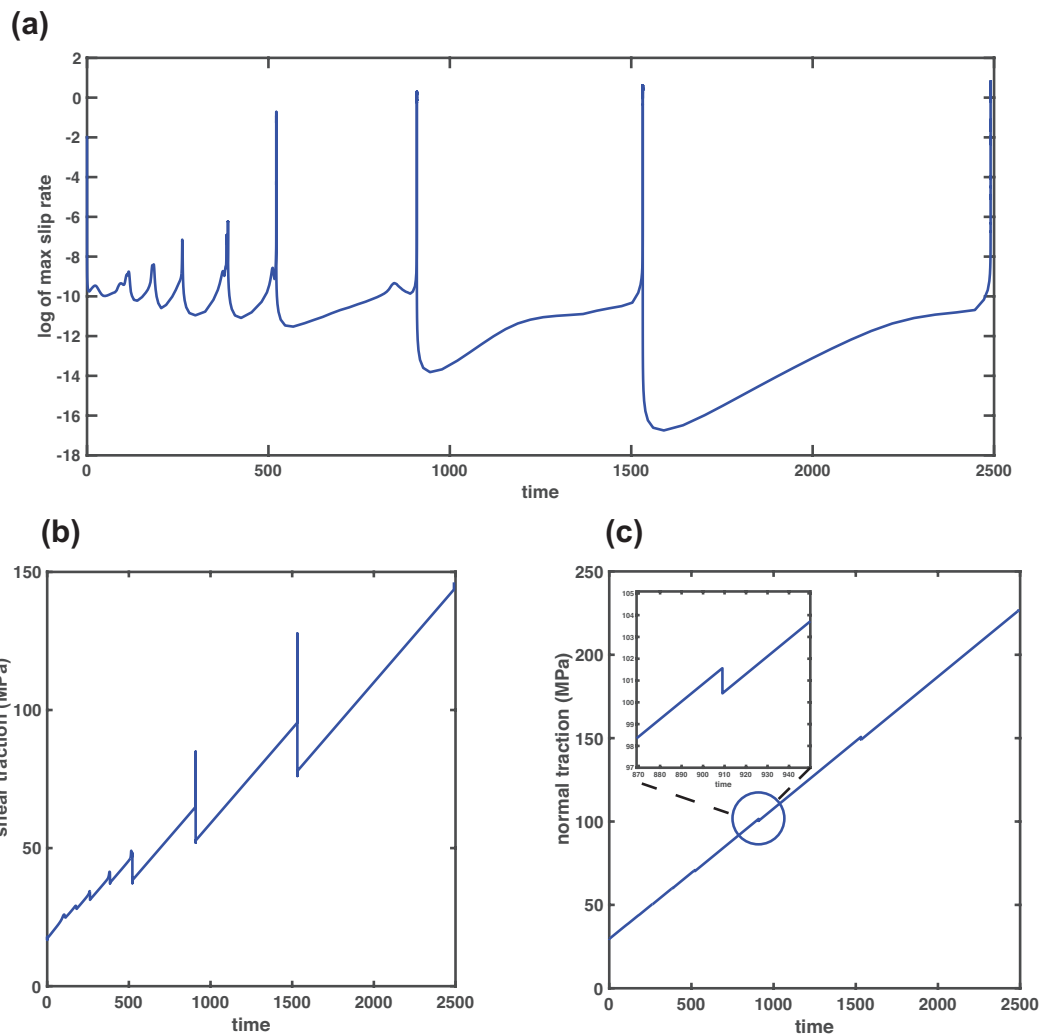
Figure 4.9: Maximum slip rate evolution, shear and normal traction evolution on the sinusoidal rough fault. The units for maximum slip rate are meters per second (m/s), and for time, they are years (yrs).

where t_{relax} is the characteristic relaxation time, σ_n is the background normal stress and τ_0 is the background shear stress. This method can resolve the issue of unrealistic stress accumulation and preserve the stress interactions in complex fault systems.

Depth variation of normal traction

The variation of normal traction with depth is primarily due to the increasing weight of the overlying rock and soil layers, leading to greater overburden pressure. This pressure, also known as lithostatic pressure, increases linearly with depth. These principles are well-documented in geological and geophysical literature (Scholz, 2019).

To enhance the realism of our model, we can consider depth variations in normal traction. By assigning normal traction element-wise within our model, it becomes straightforward to incorporate these variations and study different events along the depth of the fault. This approach allows for a more accurate representation of the stress distribution and its impact on slip events.

4.2.5 Free surface effects

Since no stress is transmitted between the solid Earth and the atmosphere, it is essential to consider half-space solutions and account for free surface effects (Segall, 2010). The half-space model is particularly important for shallow dipping faults and large subduction zones.

To simulate a fault in a semi-infinite medium, we can use the mirror image technique, which has been applied in rupture dynamics problems (Quin, 1990; Aochi and Fukuyama, 2002). By placing a "mirror image" source of stress or displacement on the opposite side of the boundary, a symmetric problem is created that is easier to solve analytically. This approach helps satisfy zero-traction boundary conditions by superposing the stress fields from the original and mirror image sources.

Zhang and Chen (2006) derived the theoretical formulation of the half-space Green's function kernel for rupture dynamics, but it is limited to planar faults and is primarily used for wave propagation problems. The dislocation method, however, offers flexibility for applying to complex geometries in elastostatic solutions. For instance, Okada (1992) gave the rectangular dislocation solution in half-space. Nikkhoo and Walter (2015) gave analytical, artifact-free triangular dislocations solution in half space. They addressed artifact singularities and numerical instabilities through a geometric method involving the superposition of three angular disloca-

tions. This method incorporates the main dislocation, the image dislocation, and a harmonic function to eliminate resultant surface normal traction, thus meeting the zero-traction boundary condition at the free surface. Applying this in FASTDASH is straightforward.

We compare the displacement distribution on the free surface with rectangular dislocation in Okada (1992) and triangular dislocation in Nikkhoo and Walter (2015), shown in Figure 4.10. The relative error is less than 10^{-4}.

To avoid the implementation of another type of kernels while incorporating free surface effects, a traction-free virtual interface at the surface can be used alongside the full-space solution. Although this approach requires more computation, it simplifies the development. It also allows the virtual surface plane's shape to be arbitrary, adapting to various topographies. This method for solving half-space problems has been implemented in rupture dynamics (Hok and Fukuyama, 2010).

Currently, our model focuses on the full-space static kernel and does not account for surface effects. We plan to enhance our model by integrating this half-space approach and considering the impact of topography. This will allow the investigation of shallow dipping faults and subduction zones.

4.2.6   Fluid fault interaction on geometrically complex faults

Including a more comprehensive impact of pore fluids could provide better insights into fault zone mechanics and earthquake-triggering processes.

Scientific objectives and state-of-the-art

Seismic hazard assessment is essential for societal safety and infrastructure resilience, aiming to quantify seismic risks for informed decision-making and preparedness. The maximum magnitude of earthquakes, influenced by the complexity of fault systems, is a critical aspect of this assessment. The geometrical complexity of fault systems in the natural environment decisively influences the initiation, propagation, and arrest of seismic events (King and Nábělek, 1985; Nakata et al., 1998; Wesnousky, 2006). Nonplanar faults, with their multi-scale roughness, introduce stress heterogeneity that determines earthquake size by controlling rupture termination. Rupture jumps across fault step-overs can significantly increase the size and magnitude of earthquakes, heightening the risk and potential damage. February 6, 2023, earthquakes in Turkey, with magnitudes of Mw 7.8 and Mw 7.6, causing over 55,000
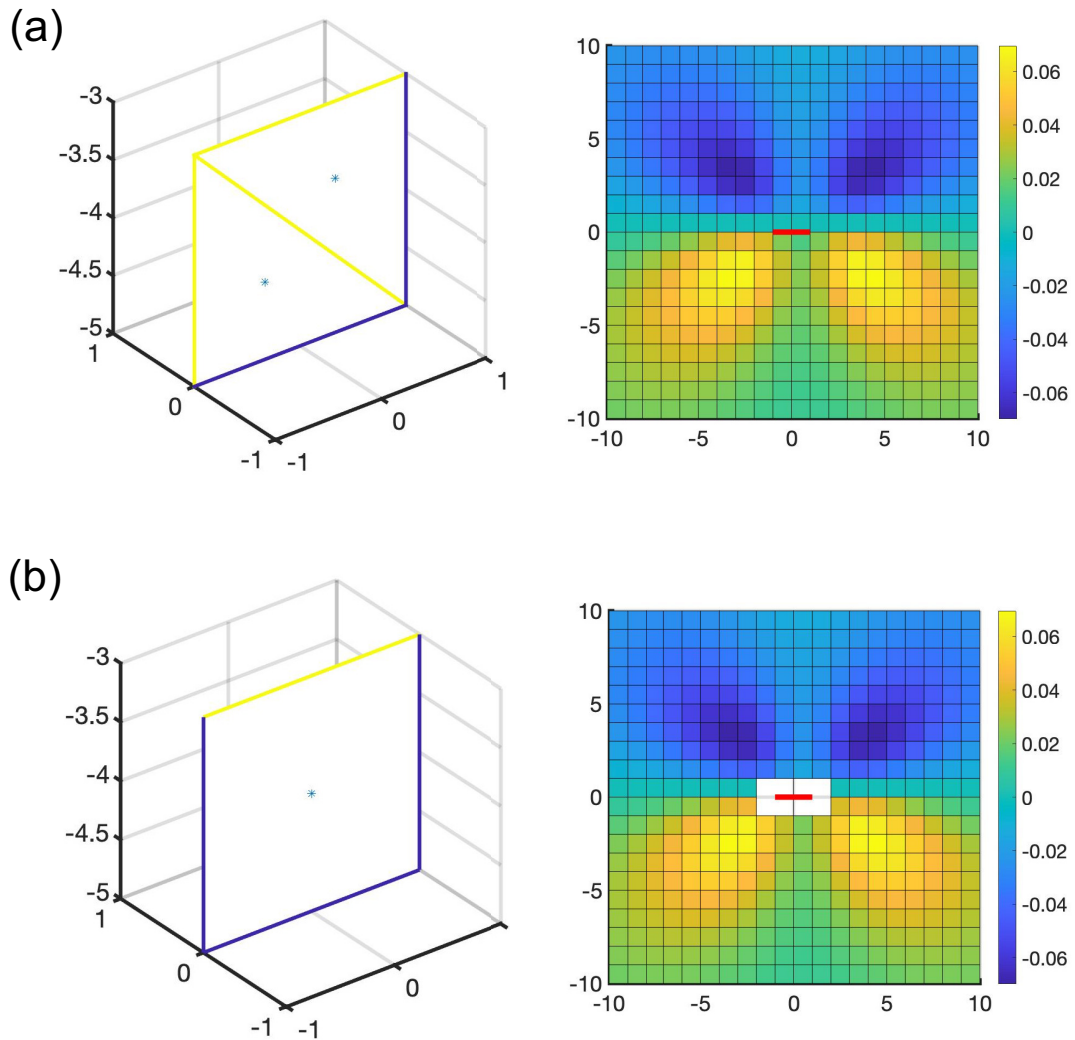
Figure 4.10: (a) Triangular elements and displacement distribution on the free surface plane by using solutions from Nikkhoo and Walter (2015). The red line represents the dislocation edge. (b) Rectangular elements and displacement distribution on the free surface plane by using a solution from Okada (1992). White elements represent singularities.

deaths and impacting around 14 million people, highlight the significance of understanding fault geometry complexities for risk assessments.

Another crucial factor in seismic activity is fluid pressure. Fault zones are filled with fluids within cracks and pores. Fluid flow can occur naturally from dehydration reactions in hydrous minerals in subducting slabs, enabling tremors, slow slip, or promoting aseismic slip (e.g., tremors in Japan, as observed by Shelly et al. (2006) and aseismic slip in New Zealand as noted by Hamling et al. (2017)). Fluid flow can also result from anthropogenic activities. Energy-related projects, such as wastewater disposal and geothermal energy production, can add or remove fluid in the medium, triggering induced seismicity (Ellsworth, 2013; Bao and Eaton, 2016; Goebel et al., 2017; Keranen and Weingarten, 2018). Surrounding a region of fluid injection, pore pressure diffusion leads to a change in effective stress, which may perturb the resistance and stability of pre-existing faults. This phenomenon has been demonstrated in the in-situ experiments of Guglielmi et al. (2015) and in the laboratory experiments of Cebry et al. (2022). Beyond fluid diffusion, poroelastic stress transfer can trigger seismicity over long distances, as shown in studies by (Segall and Lu, 2015; Goebel et al., 2017). Therefore, incorporating fluid pressure into slip sequence simulations significantly enhances their relevance to both natural and induced seismic events.

Theoretical models suggest that induced earthquake magnitude correlates with injected fluid volume (Shapiro et al., 2011; McGarr, 2014; Bentz et al., 2020), yet they often overlook prestress levels. Fracture mechanics-based models, such as those by Garagash and Germanovich (2012); Galis et al. (2017); Sáez and Lecampion (2024), highlight prestress sensitivity, but they usually assume simplistic fault geometries, neglecting complex stress interactions in multiple fault systems. However, events like the 2012 Brawley swarm (Wei et al., 2015) and the 2017 Pohang event (Palgunadi et al., 2020) reveal the significance of dynamic fault interactions in fluid-induced earthquakes.

Fluid-fault interaction yields diverse slip dynamics, while even without fluids, elastic interactions within fault networks lead to varied tractions and slips. Hence, it is crucial to consider both mechanisms for accurate slip dynamics replication. **Future work can focus revolves around complex fault geometries and the interaction between fluids and faults in earthquake cycles** (Figure 4.11). We aim to investigate fault roughness, discontinuities (step-overs), and varying fluid pressures using a comprehensive approach combining numerical modeling and experiments. Incorporating fluid effects into numerical models adds complexity but deepens our understanding of fluid-triggered events' maximum magnitudes. Laboratory experiments offer direct validation for the results of simulations, thereby synergistically

Figure 4.11: Schematic of planned fluid and fault coupling based on proof of concept model of Romanet et al. (2018).

complementing each other.

Methodology

Physics-based models facilitate numerous simulations, enabling the exploration of parameters and the creation of phase diagrams to assess significance. However, validating results can be challenging due to assumptions and real-world applicability. Laboratory experiments offer direct validation of simulation outcomes, providing tangible evidence to confirm or challenge model predictions. However, they entail higher time and financial costs compared to modeling and often have limited spatial resolution.

To effectively meet our research objectives, **we propose an integrated approach combining numerical modeling with laboratory experiments to investigate the effects of fault geometry and fluid flow on the maximum magnitude of events.** Initially, modeling will explore how factors like fault roughness and discontinuity impact the maximum magnitude of fluid-triggered seismic events, broadening possibilities and identifying key phenomena. Subsequently, laboratory experiments will cross-validate observations from numerical results. Our objectives will be addressed through three work packages (WPs).

We will implement a fluid pressure solver with the physical ingredients in a new 3D complex fault network earthquake cycle model, which is necessary to explain the experiments. This work package offers a numerical tool for experiments in WP2 and WP3.

Simulating the earthquake cycle in 3D fault networks by embedding 2D faults within a 3D medium incurs significantly higher computational costs than 2D simulations. Conventional acceleration methods like Fast Fourier Transform (FFT) are ineffective for complex fault systems. Observational studies, such as those by Ross et al. (2020), have revealed that earthquake swarm behavior is profoundly influenced by the three-dimensional fault structure, a detail overlooked by 2D models. This highlights the urgent need for an efficient tool capable of simulating 3D earthquake cycles within complex fault geometries to comprehend slip sequences accurately.

In my PhD research, I addressed this challenge by developing a simulator for seismic and aseismic sequences accelerated by Hierarchical matrices, as discussed in Chapter 2. This model efficiently handles the seismic cycle within complex fault networks, encompassing nonplanar faults and multiple fault systems governed by rate-and-state friction laws and cumulative stress from prior ruptures, all at a man-

ageable computational cost (Cheng et al., 2024b). This approach allows detailed analysis of elastic interactions across multiple faults, offering crucial insights into their collective behavior.

An effective numerical tool for analyzing complex fault networks is crucial, particularly for investigating fluid-triggered problems within a real fault system. To further enhance this model, I propose integrating pore pressure diffusion and permeability variation. This enhancement aims to provide a more comprehensive understanding of the interplay between pore fluid pressure diffusion and fault mechanics, enriching our grasp of earthquake cycles in complex geological settings.

When assuming constant permeability, pore pressure diffusion follows the analytical solution (Rudnicki, 1986). However, fluid systems can exhibit nonlinear behavior when considering spatial and temporal heterogeneous permeability. The fault zone's permeability is heterogeneous, with low permeability in the fault core and high permeability in the surrounding damage zone, decreasing with distance (Wibberley et al., 2008; Faulkner et al., 2010) from the core. In laboratory experiments, some studies indicate that permeability also changes with slip due to dilatancy (the expansion of porosity during shear deformation) and effective normal stress (Brantut, 2020; Mitchell and Faulkner, 2008; Passelègue et al., 2020).

This work package focuses on two configurations: a single rough fault and two overlapping rough faults. The objective is to investigate how stress heterogeneity, resulting from fault roughness, interaction, and far-field loading conditions, influences earthquake size-magnitude relations (the Gutenberg-Richter b-value).

Our approach integrates numerical modeling from WP1 with the experiments described here. We will utilize polymethyl methacrylate (PMMA) due to its lower shear modulus compared to rock, enabling easier observation of the nucleation process under equivalent normal stress conditions. We will begin by examining a single rough fault and then progress to a step-over fault system with two overlapping rough faults. Sandblasting or sandpaper, as well as computer numerical control (CNC) machining of the fault surface, can produce specific roughness. For step-over samples, we will cut two surfaces and glue the ends to manage fault length and overlap distance. The experimental samples will undergo uniaxial loading. Spatially varying far-field loading will be achieved by engineering a nonplanar surface. Wires will be used to initiate earthquakes, while strain gauge rosettes will measure strain in three directions.

Fault roughness, characterized by multi-scale deviations from planarity, is commonly modeled using stochastic descriptions and extensively studied for its impact

on tectonic earthquakes. It introduces natural shear and normal traction heterogeneity, influencing earthquake nucleation, propagation, and aftershock sequences (Harbord et al., 2017; Cattania and Segall, 2021; Ozawa and Ando, 2021; Goebel et al., 2023). Our approach integrates experiments and numerical methods to explore spatial-temporal changes in Gutenberg-Richter b-values. Spatial heterogeneity in b-values can offer insight into stress or slip distribution, while temporal changes can illuminate b-value evolution throughout earthquake cycles. Previous observational studies have indicated a reduction in b-values preceding large earthquakes.

Then, we build up the complexity and involve elastic interaction between two faults. The obtained results will be cross-validated with those presented in Cheng et al. (2024a): with more interaction between two faults, more slow slip events are observed in the slip catalog. The interaction intensity is controlled by a geometry factor, which is a function of overlap distance, distance between two faults, and fault width. The interaction intensity, combined with friction parameters, will determine the coexistence and dominance of slow slip events and earthquakes in the slip catalog. With numerical modeling, we can easily get a phase diagram of the laboratory scale, which will help us select parameters and prepare samples. From experiments, friction parameters can be measured with velocity step experiments and constrain the numerical model inputs (Dieterich and Kilgore, 1994; Marone, 1998).

Validating laboratory experiments helps understand local effects within the constraints of instrument size, yet natural fault processes occur on much larger scales. Numerical modeling offers a solution by simulating realistic fault geometries at the field scale, bridging the gap between experimental insights and the complex dynamics of natural fault systems. In the 2023 Turkish earthquake, two significant seismic events occurred on separate fault segments with a delay exceeding 8 hours. Preliminary results from studying this fault system reveal the reactivation of two main faults during these earthquakes (Cheng et al., 2024b). Our goal is to delve deeper into this scenario for a comprehensive understanding of interaction dynamics within this multi-fault system. **Scientific inquiries into step-over fault systems in dry conditions aim to comprehend how geometry influences earthquake and slow slip event sizes and frequencies across experimental and field scales.**

To explore fluid-fault interaction in complex fault systems, our approach integrates numerical modeling from WP1 with injection experiments based on samples in WP2. These experiments will involve injecting fluid onto a single rough fault, and two overlapped rough faults. Due to PMMA's low permeability, pore fluid pressure diffusion occurs primarily along the pre-cut fault plane during direct fluid injection. In cases where a single rough fault is subject to fluid injection, dilatancy effects and changes in permeability cannot be overlooked (Ye and Ghassemi, 2018). By studying

injection-induced events on rough faults, we aim to generate a diverse sequence of complex seismic events, replicating statistical frequency-magnitude relationships. When injecting fluid onto two overlapped rough faults, pore fluid pressure diffusion within the 2D fault plane can create spatio-temporal variations in fluid pressure. Heterogeneous effective normal traction will modify fault strength, potentially revealing unexpected phenomena compared to dry conditions. Rupture jump ability between faults may change with fluid injection, impacting earthquake size. Comparing experimental results with model outputs will elucidate whether additional physical mechanisms, such as dilatancy or variation of permeability with effective normal stress, are needed to explain fluid-triggered events. **Our research aims to understand how fluid injection influences the maximum magnitude of fluid-triggered events in a step-over system.**

Expected Results

We aim to integrate our slip sequence model with a geologically realistic fault structure, incorporating a fluid and permeability model informed by laboratory experiments. Stress heterogeneity, driven by geometrical variations such as fault roughness or multiple faults, plays a crucial role in fault slip dynamics. Furthermore, fluid injection is known to alter the stress state, affecting the magnitude and frequency of seismic events along a single fault. The scientific question is to understand mechanisms governing earthquake termination and its implications for event magnitude estimation. Specifically, we are examining how various forms of geometrical heterogeneity influence rupture expansion and arrest in injection-induced earthquakes. By elucidating these factors, we will refine seismic hazard assessment, discerning the maximum magnitude potential of fault systems. We model both laboratory experiments and hypotetical field cases using identical configurations to bridge scales and extrapolate insights gained at the lab scale. Our objective includes replicating earthquake statistics and emphasizing the understanding of maximum seismic event magnitude factors. Analyzing fault stability under fluid injection aids in mitigating seismic hazards from industrial activities, deepening fault mechanics understanding, and enhancing seismic impact prediction and management in fluid injection processes.

Chapter 5

Conclusions

As discussed in the introduction of this thesis, natural fault systems present complex geometries. It has been observed in several cases that the complex geometry of faults can control the slip dynamic sequences and can generate slow ruptures, commonly known as SSEs. Even though the geometry of fault has been widely neglected in traditional numerical models, recent studies have started to address it, in particular, using 2D models for computational reasons. Some current models allow for 3D geometrical complexity investigation. However, they are not computationally efficient.

The main purpose of this thesis is to understand the role of complex fault geometry in the earthquake cycle. To achieve this, we developed a highly efficient 3D earthquake sequence simulator, FASTDASH, from scratch using the Boundary Element Method (BEM) with Hierarchical Matrices.

In Chapter 2, we introduce a quasi-dynamic earthquake cycle model for 3D geometrically complex fault systems governed by the rate-and-state friction law. Using a boundary element method accelerated by Hierarchical Matrices, we convert force equilibrium on faults into a series of ordinary differential equations (ODEs) to simulate the evolution of slip rate, rake angle, shear and normal tractions, and moment rate on the faults. Hierarchical matrices effectively solve 3D complex faults, reducing computational complexities from $O(N^2)$ to $O(N \log N)$, where N represents the number of discretized fault elements. For a fault discretized with 10^5 elements, traditional algorithms require 10^{10} resources, whereas H-matrices reduce this to 1.16×10^6. This approach provides the feasibility to conduct large-scale three-dimensional computations universally adaptable to any fault geometry, helping us understand realistic earthquakes.

To validate our method, we benchmarked our model with static analytical solutions, such as a penny-shaped crack under constant loading and an elastic crack surrounded by a cohesive zone (Dugdale crack). We also cross-validated it with the Southern California Earthquake Center SEAS BP4-QD benchmark to ensure code accuracy during earthquake cycles. We also provide insights on selecting numerical parameters like H-matrix properties and tolerance for ODE solvers to balance computing time and result accuracy.

In Chapter 3, we explore step-over fault systems. We generated spatiotemporal complex slip events from a step-over fault system with two parallel faults, demonstrating how geometrical factors affect fault behavior. Specifically, we defined a fault interaction metric Λ, a function of geometrical parameters, and found its relation to the SSE moment release rate in the slip catalog. We observed that slow slip events occur only within a certain range of Λ. This metric can also be easily extended to other geometries. Additionally, we reproduced scaling laws, in particular, moment-duration scaling for both fast and slow ruptures, and we show that the slow rupture scaling is highly sensitive to the slip rate threshold used to detect the events. This might imply that the sensitivity of the instrumental tools might also influence the scaling for slow ruptures observed in nature.

In Chapter 4, we discuss the implications and perspectives of our work. Due to its universal applicability, our model can be applied to more realistic fault geometries. We apply our previously developed method to the 2023 Turkey earthquake and aftershocks, and we show how the geometry of the fault systems in that region control the slip dynamics of this seismic sequence. It is also straightforward to assign friction heterogeneity, depth-dependent normal stress, and different loading approaches, showcasing our code's high flexibility. Furthermore, developing this effective numerical tool for earthquake cycles lays the foundation for future work incorporating fluid injection.

Bibliography

Almakari, M., Kheirdast, N., Villafuerte, C.D., Thomas, M.Y., Bhat, H.S., Cheng, J., Dubernet, P., 2024. Full spectrum of slip dynamics of a fault zone: Source dynamics. to be submitted .

Ampuero, J.P., Rubin, A.M., 2008. Earthquake nucleation on rate and state faults–aging and slip laws. J. Geophys. Res. 113. doi:10.1029/2007JB005082.

Ando, R., Imanishi, K., Panayotopoulos, Y., Kobayashi, T., 2017. Dynamic rupture propagation on geometrically complex fault with along-strike variation of fault maturity: insights from the 2014 northern nagano earthquake. Earth, Planets and Space 69, 130. doi:10.1186/s40623-017-0715-2.

Ando, R., Ujiie, K., Nishiyama, N., Mori, Y., 2023. Depth-dependent slow earthquakes controlled by temperature dependence of brittle-ductile transitional rheology. Geophysical Research Letters 50. doi:10.1029/2022gl101388.

Andrews, D.J., 1976. Rupture velocity of plane strain shear cracks. J. Geophys. Res. 81, 5679–5689. doi:10.1029/JB081i032p05679.

Antolik, M., Abercrombie, R.E., Ekstrom, G., 2004. The 14 november 2001 kokoxili (kunlunshan), tibet, earthquake: Rupture transfer through a large extensional step-over. Bull. Seism. Soc. Am. 94, 1173–1194. doi:10.1785/012003180.

Aochi, H., Fukuyama, E., 2002. Three-dimensional nonplanar simulation of the 1992 landers earthquake. J. Geophys. Res. 107. doi:10.1029/2000JB000061.

Aochi, H., Ide, S., 2009. Complexity in earthquake sequences controlled by multiscale heterogeneity in fault fracture energy. Journal of Geophysical Research: Solid Earth 114. doi:10.1029/2008jb006034.

Avouac, J.P., 2015. From geodetic imaging of seismic and aseismic fault slip to dynamic modeling of the seismic cycle. Ann. Rev. Earth Planet. Sci. 43, 233–271. doi:10.1146/annurev-earth-060614-105302.

Bakun, W.H., Lindh, A.G., 1985. The parkfield, california, earthquake prediction experiment. Science 229, 619–624. doi:10.1126/science.229.4714.619.

Bao, X., Eaton, D.W., 2016. Fault activation by hydraulic fracturing in western canada. Science , 10.1126/science.aag2583doi:10.1126/science.aag2583.

Barbot, S., 2021. A spectral boundary-integral method for quasi-dynamic ruptures of multiple parallel faults. Bulletin of the Seismological Society of America 111, 1614–1630. doi:10.1785/0120210004.

Barbot, S., 2022. A rate-, state-, and temperature-dependent friction law with competing healing mechanisms. Journal of Geophysical Research: Solid Earth 127. doi:10.1029/2022jb025106.

Barbot, S., Moore, J.D.P., Lambert, V., 2017. Displacement and stress associated with distributed anelastic deformation in a half-space. Bulletin of the Seismological Society of America 107, 821–855. doi:10.1785/0120160237.

Barnes, P.M., Wallace, L.M., Saffer, D.M., Bell, R.E., Underwood, M.B., Fagereng, A., Meneghini, F., Savage, H.M., Rabinowitz, H.S., Morgan, J.K., Kitajima, H., Kutterolf, S., Hashimoto, Y., Engelmann de Oliveira, C.H., Noda, A., Crundwell, M.P., Shepherd, C.L., Woodhouse, A.D., Harris, R.N., Wang, M., Henrys, S., Barker, D.H., Petronotis, K.E., Bourlange, S.M., Clennell, M.B., Cook, A.E., Dugan, B.E., Elger, J., Fulton, P.M., Gamboa, D., Greve, A., Han, S., Hüpers, A., Ikari, M.J., Ito, Y., Kim, G.Y., Koge, H., Lee, H., Li, X., Luo, M., Malie, P.R., Moore, G.F., Mountjoy, J.J., McNamara, D.D., Paganoni, M., Screaton, E.J., Shankar, U., Shreedharan, S., Solomon, E.A., Wang, X., Wu, H.Y., Pecher, I.A., LeVay, L.J., 2020. Slow slip source characterized by lithological and geometric heterogeneity. Science Advances 6. doi:10.1126/sciadv.aay3314.

Ben-Zion, Y., Peng, Z., Okaya, D., Seeber, L., Armbruster, J.G., Ozer, N., Michael, A.J., Baris, S., Aktar, M., 2003. A shallow fault-zone structure illuminated by trapped waves in the Karadere–Duzce branch of the North Anatolian Fault, western Turkey. Geophys. J. Int. 152, 699–717. doi:10.1046/j.1365-246X.2003.01870.x.

Bentz, S., Kwiatek, G., Martínez-Garzón, P., Bohnhoff, M., Dresen, G., 2020. Seismic moment evolution during hydraulic stimulations. Geophysical Research Letters 47. doi:10.1029/2019gl086185.

Ben-Zion, Y., Rice, J.R., 1995. Slip patterns and earthquake populations along different classes of faults in elastic solids. Journal of Geophysical Research: Solid Earth 100, 12959–12983. doi:10.1029/94jb03037.

Ben-Zion, Y., Rice, J.R., 1997. Dynamic simulations of slip on a smooth fault in an elastic solid. Journal of Geophysical Research: Solid Earth 102, 17771–17784. doi:10.1029/97jb01341.

Bernaudin, M., Gueydan, F., 2018. Episodic tremor and slip explained by fluid-enhanced microfracturing and sealing. Geophysical Research Letters 45, 3471–3480. doi:10.1029/2018gl077586.

Bhattacharya, P., Rubin, A.M., Bayart, E., Savage, H.M., Marone, C., 2015. Critical evaluation of state evolution laws in rate and state friction: Fitting large velocity steps in simulated fault gouge with time-, slip-, and stress-dependent constitutive laws. J. Geophys. Res. 120, 6365–6385. doi:10.1002/2015JB012437.

Bhattacharya, P., Rubin, A.M., Tullis, T.E., Beeler, N.M., Okazaki, K., 2022. The evolution of rock friction is more sensitive to slip than elapsed time, even at near-zero slip rates. Proc. Natl. Acad. Sci. USA 119. doi:10.1073/pnas.2119462119.

Bhattacharya, P., Viesca, R.C., 2019. Fluid-induced aseismic fault slip outpaces pore-fluid migration. Science 364, 464–468. doi:10.1126/science.aaw7354.

Biasi, G.P., Wesnousky, S.G., 2016. Steps and gaps in ground ruptures: Empirical bounds on rupture propagation. Bulletin of the Seismological Society of America 106, 1110–1124. doi:10.1785/0120150175.

Biasi, G.P., Wesnousky, S.G., 2021. Rupture passing probabilities at fault bends and steps, with application to rupture length probabilities for earthquake early warning. Bulletin of the Seismological Society of America 111, 2235–2247. doi:10.1785/0120200370.

Blanpied, M., Marone, C., Lockner, D., Byerlee, J., King, D., 1998. Quantitative measure of the variation in fault rheology due to fluid-rock interactions. J. Geophys. Res. 103, 9691–9712.

Blanpied, M.L., Lockner, D.A., Byerlee, J.D., 1995. Frictional slip of granite at hydrothermal conditions. Journal of Geophysical Research: Solid Earth 100, 13045–13064. doi:10.1029/95jb00862.

Bletery, Q., Nocquet, J.M., 2020. Slip bursts during coalescence of slow slip events in cascadia. Nature Communications 11. doi:10.1038/s41467-020-15494-4.

Bonnet, M., 1999. Boundary Integral Equation Methods for Solids and Fluids. John Wiley & Sons Inc.

Bouchon, M., Karabulut, H., Aktar, M., Ozalaybey, S., Schmittbuhl, J., Bouin, M.P., 2011. Extended Nucleation of the 1999 Mw 7.6 Izmit Earthquake. Science 331, 877–880. doi:10.1126/science.1197341.

Brace, W.F., Byerlee, J.D., 1966. Stick-slip as a mechanism for earthquakes. Science 153, 990–992. doi:10.1126/science.153.3739.990.

Brantut, N., 2020. Dilatancy-induced fluid pressure drop during dynamic rupture: Direct experimental evidence and consequences for earthquake dynamics. Earth and Planetary Science Letters 538, 116179. doi:10.1016/j.epsl.2020.116179.

Bürgmann, R., 2018. The geophysics, geology and mechanics of slow fault slip. Earth Planet. Sc. Lett. 495, 112–134. doi:10.1016/j.epsl.2018.04.062.

Bürgmann, R., Rosen, P.A., Fielding, E.J., 2000. Synthetic aperture radar interferometry to measure earth's surface topography and its deformation. Annu. Rev. Earth Planet. Sci. 28, 169–209.

Burridge, R., Knopoff, L., 1967. Model and theoretical seismicity. B. Seismol. Soc. Am. 57, 341–371.

Byerlee, J., 1967. Frictional characteristics of granite under high confining pressure. J. Geophys. Res. 72, 3639–3648. doi:10.1029/JZ072i014p03639.

Carpenter, B.M., Collettini, C., Viti, C., Cavallo, A., 2016. The influence of normal stress and sliding velocity on the frictional behaviour of calcite at room temperature: insights from laboratory experiments and microstructural observations. Geophys. J. Int. 205, 548–561.

Cattania, C., 2019. Complex earthquake sequences on simple faults. Geophys. Res. Lett. 46, 10384—10393. doi:10.1029/2019GL083628.

Cattania, C., Segall, P., 2021. Precursory slow slip and foreshocks on rough faults. Journal of Geophysical Research: Solid Earth 126. doi:10.1029/2020jb020430.

Cebry, S.B.L., Ke, C., McLaskey, G.C., 2022. The role of background stress state in fluid-induced aseismic slip and dynamic rupture on a 3-m laboratory fault. Journal of Geophysical Research: Solid Earth 127. doi:10.1029/2022jb024371.

Cesca, S., Zhang, Y., Mouslopoulou, V., Wang, R., Saul, J., Savage, M., Heimann, S., Kufner, S.K., Oncken, O., Dahm, T., 2017. Complex rupture process of the mw 7.8, 2016, kaikoura earthquake, new zealand, and its aftershock sequence. Earth Planet. Sc. Lett. 478, 110–120. doi:10.1016/j.epsl.2017.08.024.

Chalumeau, C., Agurto-Detzel, H., Rietbrock, A., Frietsch, M., Oncken, O., Segovia, M., Galve, A., 2024. Seismological evidence for a multifault network at the subduction interface. Nature 628, 558–562. doi:10.1038/s41586-024-07245-y.

Chen, J., Niemeijer, A.R., Spiers, C.J., 2017. Microphysically derived expressions for rate-and-state friction parameters, a, b, and d_c. J. Geophys. Res. Solid Earth 122, 9627–9657.

Chen, T., Lapusta, N., 2009. Scaling of small repeating earthquakes explained by interaction of seismic and aseismic slip in a rate and state fault model. J. Geophys. Res. 114. doi:10.1029/2008JB005749.

Cheng, J., Almakari, M., Peruzzo, C., Lecampion, B., Bhat, H.S., 2024a. The effect of 3d fault interactions on slow and fast earthquakes. to be submitted for GRL .

Cheng, J., Almakari, M., Peruzzo, C., Lecampion, B., Bhat, H.S., 2024b. Fastdash, a quasi-dynamic 3d seismic cycle model by using boundary element method with h-matrices. to be submitted for GJI .

Chiaraluce, L., 2012. Unravelling the complexity of apenninic extensional fault systems: A review of the 2009 l'aquila earthquake (central apennines, italy). Journal of Structural Geology 42, 2–18. doi:10.1016/j.jsg.2012.06.007.

Ciardo, F., Lecampion, B., Fayard, F., Chaillat, S., 2020. A fast boundary element based solver for localized inelastic deformations. International Journal for Numerical Methods in Engineering 121, 5696–5718. doi:10.1002/nme.6520.

Cocco, M., Aretusini, S., Cornelio, C., Nielsen, S.B., Spagnuolo, E., Tinti, E., Toro, G.D., 2023. Fracture energy and breakdown work during earthquakes. Ann. Rev. Earth Planet. Sci. 51, 217–252. doi:10.1146/annurev-earth-071822-100304.

Cohee, B.P., Beroza, G., 1994. Slip distribution of the 1992 landers earthquake and its implications for earthquake source mechanics. doi:10.1785/BSSA0840030692.

Cruz-Atienza, V.M., Villafuerte, C.D., Bhat, H.S., 2018. Rapid tremor migration and pore-pressure waves in subduction zones. Nat. Commun. 9, 2900. doi:10.1038/s41467-018-05150-3.

Di Toro, G., Han, R., Hirose, T., De Paola, N., Nielsen, S., Mizoguchi, K., Ferri, F., Cocco, M., Shimamoto, T., 2011. Fault lubrication during earthquakes. Nature 471, 494–498. doi:10.1038/nature09838.

Dieterich, J., 1994. A constitutive law for rate of earthquake production and its application to earthquake clustering. J. Geophys. Res. 99, 2601–2618.

Dieterich, J., Kilgore, B., 1994. Direct observation of frictional contacts: New insights for state-dependent properties. Pure Appl. Geophys. 143, 283–302.

Dieterich, J.H., 1972. Time-dependent friction as a possible mechanism for aftershocks. Journal of Geophysical Research 77, 3771–3781. doi:10.1029/jb077i020p03771.

Dieterich, J.H., 1979a. Modeling of rock friction: 1. experimental results and constitutive equations. Journal of Geophysical Research: Solid Earth 84, 2161–2168. doi:10.1029/jb084ib05p02161.

Dieterich, J.H., 1979b. Modeling of rock friction: 1. experimental results and constitutive equations. J. Geophys. Res. 84, 2161–2168. doi:10.1029/JB084iB05p02161.

Dieterich, J.H., 1992. Earthquake nucleation on faults with rate-and state-dependent strength. Tectonophysics 211, 115–134.

Dieterich, J.H., Kilgore, B., 1996. Implications of fault constitutive properties for earthquake prediction. Proc. Natl. Acad. Sci. USA 93, 3787–3794.

Dragert, H., Wang, K., James, T.S., 2001. A silent slip event on the deeper cascadia subduction interface. Science 292, 1525–1528.

Duan, B., 2012. Dynamic rupture of the 2011 mw 9.0 tohoku-oki earthquake: Roles of a possible subducting seamount. J. Geophys. Res. 117, B05311. doi:10.1029/2011JB009124.

Dublanchet, P., Bernard, P., Favreau, P., 2013. Interactions and triggering in a 3-d rate-and-state asperity model. J. Geophys. Res. 118, 2225–2245. doi:10.1002/jgrb.50187.

Dugdale, D., 1960. Yielding of steel sheets containing slits. J. Mech. Phys. Solids 8, 66–75.

Ellsworth, W.L., 2013. Injection-induced earthquakes. Science 341. doi:10.1126/science.1225942.

Emre, Ö., Duman, T.Y., Özalp, S., Şaroğlu, F., Olgun, Ş., Elmacı, H., Çan, T., 2018. Active fault database of turkey. Bulletin of Earthquake Engineering 16, 3229–3275.

Erickson, B.A., Birnir, B., Lavallée, D., 2011. Periodicity, chaos and localization in a burridge-knopoff model of an earthquake with rate-and-state friction: Burridge-knopoff model of an earthquake. Geophysical Journal International 187, 178–198. doi:10.1111/j.1365-246x.2011.05123.x.

Fata, S.N., 2011. Explicit expressions for three-dimensional boundary integrals in linear elasticity. Journal of Computational and Applied Mathematics 235, 4480–4495. doi:10.1016/j.cam.2011.04.017.

Faulkner, D., Jackson, C., Lunn, R., Schlische, R., Shipton, Z., Wibberley, C., Withjack, M., 2010. A review of recent developments concerning the structure, mechanics and fluid flow properties of fault zones. Journal of Structural Geology 32, 1557–1575. doi:10.1016/j.jsg.2010.06.009.

Faure Walker, J., Boncio, P., Pace, B., Roberts, G., Benedetti, L., Scotti, O., Visini, F., Peruzza, L., 2021. Fault2sha central apennines database and structuring active fault data for seismic hazard assessment. Scientific Data 8. doi:10.1038/s41597-021-00868-0.

Feblberg, E., 1969. Low-order classical runge-kutta formulas with stepsize control and their application to some heat transfer problems.

Frank, W.B., Brodsky, E.E., 2019. Daily measurement of slow slip from low-frequency earthquakes is consistent with ordinary earthquake scaling. Science Advances 5. doi:10.1126/sciadv.aaw9386.

Galis, M., Ampuero, J.P., Mai, P.M., Cappa, F., 2017. Induced seismicity provides insight into why earthquake ruptures stop. Science Advances 3. doi:10.1126/sciadv.aap7528.

Gao, X., Wang, K., 2017. Rheological separation of the megathrust seismogenic zone and episodic tremor and slip. Nature 543, 416–419. doi:10.1038/nature21389.

Garagash, D.I., Germanovich, L.N., 2012. Nucleation and arrest of dynamic slip on a pressurized fault. J. Geophys. Res. 117. doi:10.1029/2012JB009209.

Geuzaine, C., Remacle, J., 2009. Gmsh: A 3-d finite element mesh generator with built-in pre- and post-processing facilities. International Journal for Numerical Methods in Engineering 79, 1309–1331. doi:10.1002/nme.2579.

Gilbert, G.K., 1884. A theory of the earthquakes of the great basin, with a practical application. American Journal of Science 27, 49–53.

Goebel, T.H., Kwiatek, G., Becker, T.W., Brodsky, E.E., Dresen, G., 2017. What allows seismic events to grow big?: Insights from b-value and fault roughness analysis in laboratory stick-slip experiments. Geology 45, 815–818. doi:10.1130/g39147.1.

Goebel, T.H.W., Brodsky, E.E., Dresen, G., 2023. Fault roughness promotes earthquake-like aftershock clustering in the lab. Geophysical Research Letters 50. doi:10.1029/2022gl101241.

Greengard, L., Rokhlin, V., 1987. A fast algorithm for particle simulations. J. Comput. Phys. 73, 325–348.

Gu, J.C., Rice, J.R., Ruina, A.L., Simon, T.T., 1984. Slip motion and stability of a single degree of freedom elastic system with rate and state dependent friction. J. Mech. Phys. Solids 32, 167–196.

Guglielmi, Y., Cappa, F., Avouac, J.P., Henry, P., Elsworth, D., 2015. Seismicity triggered by fluid injection–induced aseismic slip. Science 348, 1224–1226. doi:10.1126/science.aab0476.

Gutenberg, B., Richter, C.F., 1944. Frequency of earthquakes in california. Bull. Seism. Soc. Am. 34, 185–188.

Hackbusch, W., 2015. Hierarchical matrices: algorithms and analysis. volume 49. Springer.

Hall, K., Houston, H., Schmidt, D., 2018. Spatial comparisons of tremor and slow slip as a constraint on fault strength in the northern cascadia subduction zone. Geochemistry, Geophysics, Geosystems 19, 2706–2718. doi:10.1029/2018gc007694.

Hamling, I.J., Hreinsdóttir, S., Clark, K., Elliott, J., Liang, C., Fielding, E., Litchfield, N., Villamor, P., Wallace, L., Wright, T.J., D'Anastasio, E., Bannister, S., Burbidge, D., Denys, P., Gentle, P., Howarth, J., Mueller, C., Palmer, N., Pearson, C., Power, W., Barnes, P., Barrell, D.J.A., Van Dissen, R., Langridge, R., Little, T., Nicol, A., Pettinga, J., Rowland, J., Stirling, M., 2017. Complex multifault rupture during the 2016 mw 7.8 kaikōura earthquake, new zealand. Science doi:10.1126/science.aam7194.

Hanks, T.C., Kanamori, H., 1979. A moment magnitude scale. Journal of Geophysical Research: Solid Earth 84, 2348–2350. doi:10.1029/jb084ib05p02348.

Harbord, C.W.A., Nielsen, S.B., De Paola, N., Holdsworth, R.E., 2017. Earthquake nucleation on rough faults. Geology 45, 931–934. doi:10.1130/G39181.1.

Harris, C.R., Millman, K.J., van der Walt, S.J., Gommers, R., Virtanen, P., Cournapeau, D., Wieser, E., Taylor, J., Berg, S., Smith, N.J., Kern, R., Picus, M., Hoyer, S., van Kerkwijk, M.H., Brett, M., Haldane, A., del Río, J.F., Wiebe, M., Peterson, P., Gérard-Marchant, P., Sheppard, K., Reddy, T., Weckesser, W., Abbasi, H., Gohlke, C., Oliphant, T.E., 2020. Array programming with NumPy. URL: https://numpy.org, doi:10.1038/s41586-020-2649-2, arXiv:2006.10256.

Haugene, T.H., 2016. pyodesys: Python package for solving systems of odes and daes. https://github.com/bjodah/pyodesys. Accessed: 2024-07-29.

Hauksson, E., Jones, L.M., Hutton, K., Eberhart-Phillips, D., 1993. The 1992 landers earthquake sequence: Seismological observations. Journal of Geophysical Research: Solid Earth 98, 19835–19858. doi:10.1029/93jb02384.

Heimisson, E.R., 2020. Crack to pulse transition and magnitude statistics during earthquake cycles on a self-similar rough fault. Earth and Planetary Science Letters 537, 116202. doi:10.1016/j.epsl.2020.116202.

Hillers, G., Ben-Zion, Y., Mai, P.M., 2006. Seismicity on a fault controlled by rate- and state-dependent friction with spatial variations of the critical slip distance. Journal of Geophysical Research: Solid Earth 111. doi:10.1029/2005jb003859.

Hills, D.A., Kelly, P., Dai, D., Korsunsky, A., 2013. Solution of crack problems: the distributed dislocation technique. Springer Science & Business Media.

Hirose, H., Hirahara, K., Kimata, F., Fujii, N., Miyazaki, S., 1999. A slow thrust slip event following the two 1996 hyuganada earthquakes beneath the bungo channel, southwest japan. Geophys. Res. Lett. 26, 3237–3240.

Hirose, H., Obara, K., 2006. Short-term slow slip and correlated tremor episodes in the tokai region, central japan. Geophys. Res. Lett. 33. doi:10.1029/2006GL026579.

Hok, S., Fukuyama, E., 2010. A new biem for rupture dynamics in half-space and its application to the 2008 iwate-miyagi nairiku earthquake: A new biem for rupture dynamics in half-space. Geophysical Journal International 184, 301–324. doi:10.1111/j.1365-246x.2010.04835.x.

Huang, H., Hawthorne, J.C., 2022. Linking the scaling of tremor and slow slip near parkfield, ca. Nature Communications 13. URL: http://dx.doi.org/10.1038/s41467-022-33158-3, doi:10.1038/s41467-022-33158-3.

Hubbard, J., Almeida, R., Foster, A., Sapkota, S.N., Bürgi, P., Tapponnier, P., 2016. Structural segmentation controlled the 2015 mw 7.8 gorkha earthquake rupture in nepal. Geology 44, 639–642. doi:10.1130/g38077.1.

Ida, Y., 1972. Cohesive force across tip of a longitudinal-shear crack and griffiths specific surface-energy. J. Geophys. Res. 77, 3796–3805. doi:10.1029/JB077i020p03796.

Ide, S., Beroza, G.C., 2023. Slow earthquake scaling reconsidered as a boundary between distinct modes of rupture propagation. Proc. Natl. Acad. Sci. USA 120. doi:10.1073/pnas.2222102120.

Ide, S., Beroza, G.C., Shelly, D.R., Uchide, T., 2007. A scaling law for slow earthquakes. Nature 447, 76–79. doi:10.1038/nature05780.

Im, K., Avouac, J.P., 2021. On the role of thermal stress and fluid pressure in triggering seismic and aseismic faulting at the brawley geothermal field, california. Geothermics 97, 102238. doi:10.1016/j.geothermics.2021.102238.

Ito, Y., Obara, K., Shiomi, K., Sekine, S., Hirose, H., 2007. Slow earthquakes coincident with episodic tremors and slow slip events. Science 315, 503–506. doi:10.1126/science.1134454.

Jiang, J., Erickson, B.A., Lambert, V.R., Ampuero, J.P., Ando, R., Barbot, S.D., Cattania, C., Zilio, L.D., Duan, B., Dunham, E.M., Gabriel, A.A., Lapusta, N., Li, D., Li, M., Liu, D., Liu, Y., Ozawa, S., Pranger, C., van Dinther, Y., 2022. Community-driven code comparisons for three-dimensional dynamic modeling of sequences of earthquakes and aseismic slip. Journal of Geophysical Research: Solid Earth 127. doi:10.1029/2021jb023519.

Johnson, L.R., 2010. An earthquake model with interacting asperities. Geophys. J. Int. 182, 1339–1373.

Jolivet, R., Lasserre, C., Doin, M.P., Peltzer, G., Avouac, J.P., Sun, J., Dailu, R., 2013. Spatio-temporal evolution of aseismic slip along the haiyuan fault, china: Implications for fault frictional properties. Earth Planet. Sc. Lett. 377, 23–33. doi:10.1016/j.epsl.2013.07.020.

Kanamori, H., 1977. The energy release in great earthquakes. J. Geophys. Res. 82, 2981–2987.

Kanamori, H., Anderson, D.L., 1975. Theoretical basis of some empirical relations in seismology. Bull. Seism. Soc. Am. 65, 1073–1095.

Kaneko, Y., Avouac, J.P., Lapusta, N., 2010. Towards inferring earthquake patterns from geodetic observations of interseismic coupling. Nature Geoscience 3, 363–369. doi:10.1038/ngeo843.

Kato, A., Obara, K., Igarashi, T., Tsuruoka, H., Nakagawa, S., Hirata, N., 2012. Propagation of Slow Slip Leading Up to the 2011 Mw 9.0 Tohoku-Oki Earthquake. Science 335, 705–708. doi:10.1126/science.1215141.

Kato, N., 2003. Repeating slip events at a circular asperity: numerical simulation with a rate- and state-dependent friction law. Bull. Earthq. Res. Inst. 78, 151–166.

Kato, N., 2004. Interaction of slip on asperities: Numerical simulation of seismic cycles on a two-dimensional planar fault with nonuniform frictional property. Journal of Geophysical Research: Solid Earth 109. doi:10.1029/2004jb003001.

Keranen, K.M., Weingarten, M., 2018. Induced seismicity. Annual Review of Earth and Planetary Sciences 46, 149–174. doi:10.1146/annurev-earth-082517-010054.

King, G., Nábělek, J., 1985. Role of fault bends in the initiation and termination of earthquake rupture. Science 228, 984–987. doi:10.1126/science.228.4702.984.

Kirkpatrick, J.D., Fagereng, Å., Shelly, D.R., 2021. Geological constraints on the mechanisms of slow earthquakes. Nature Reviews Earth Environment 2, 285–301. doi:10.1038/s43017-021-00148-w.

Klinger, Y., Okubo, K., Vallage, A., Champenois, J., Delorme, A., Rougier, E., Lei, Z., Knight, E.E., Munjiza, A., Satriano, C., Baize, S., Langridge, R., Bhat, H.S., 2018. Earthquake damage patterns resolve complex rupture processes. Geophys. Res. Lett. doi:10.1029/2018GL078842.

Kostrov, B.V., 1964. Selfsimilar problems of propagation of shear cracks. J. Appl. Math. Mech.-USS. 28, 1077–1087. doi:10.1016/0021-8928(64)90010-3.

Kwiatek, G., Martínez-Garzón, P., Goebel, T., Bohnhoff, M., Ben-Zion, Y., Dresen, G., 2024. Intermittent criticality multi-scale processes leading to large slip events on rough laboratory faults. Journal of Geophysical Research: Solid Earth 129. doi:10.1029/2023jb028411.

Lapusta, N., Liu, Y., 2009. Three-dimensional boundary integral modeling of spontaneous earthquake sequences and aseismic slip. J. Geophys. Res. 114. doi:10.1029/2008JB005934.

Lapusta, N., Rice, J.R., Ben-Zion, Y., Zheng, G., 2000. Elastodynamic analysis for slow tectonic loading with spontaneous rupture episodes on faults with rate-and-state-dependent friction. J. Geophys. Res. 105, 23675–23789. doi:10.1029/2000JB900250.

Lay, T., Kanamori, H., Ammon, C.J., Koper, K.D., Hutko, A.R., Ye, L., Yue, H., Rushing, T.M., 2012. Depth-varying rupture properties of subduction zone megathrust faults. Journal of Geophysical Research: Solid Earth 117. doi:10.1029/2011jb009133.

Lee, J., Tsai, V.C., Hirth, G., Chatterjee, A., Trugman, D.T., 2024. Fault-network geometry influences earthquake frictional behaviour. Nature doi:10.1038/s41586-024-07518-6.

Leeman, J.R., Saffer, D.M., Scuderi, M.M., Marone, C., 2016. Laboratory observations of slow earthquakes and the spectrum of tectonic fault slip modes. Nature Communications 7. doi:10.1038/ncomms11104.

Li, D., Liu, Y., 2016. Spatiotemporal evolution of slow slip events in a nonplanar fault model for northern cascadia subduction zone. J. Geophys. Res. 121, 6828–6845. doi:10.1002/2016JB012857.

Li, M., Pranger, C., van Dinther, Y., 2022. Characteristics of earthquake cycles: A cross-dimensional comparison of 0d to 3d numerical models. Journal of Geophysical Research: Solid Earth 127. doi:10.1029/2021jb023726.

Linker, M., Dieterich, J., 1992. Effects of variable normal stress on rock friction: Observations and constitutive equations. J. Geophys. Res. 97, 4923–4940.

Liu, D., Duan, B., Luo, B., 2019. EQsimu: a 3-d finite element dynamic earthquake simulator for multicycle dynamics of geometrically complex faults governed by rate- and state-dependent friction. Geophysical Journal International 220, 598–609. doi:10.1093/gji/ggz475.

Liu, Y., Rice, J.R., 2005. Aseismic slip transients emerge spontaneously in 3d rate and state modeling of subduction earthquake sequences. J. Geophys. Res. 110, B08307. doi:10.1029/2004JB003424.

Liu, Y., Rice, J.R., 2007. Spontaneous and triggered aseismic deformation transients in a subduction fault model. J. Geophys. Res. 112, B09404. doi:10.1029/2007JB004930.

Liu, Y., Rubin, A.M., 2010. Role of fault gouge dilatancy on aseismic deformation transients. J. Geophys. Res. 115. doi:10.1029/2010JB007522.

Liu-Zeng, J., Yao, W., Liu, X., Shao, Y., Wang, W., Han, L., Wang, Y., Zeng, X., Li, J., Wang, Z., Liu, Z., Tu, H., 2022. High resolution structure from motion models covering 160 km long surface ruptures of the 2021 mw 7.4 madoi earthquake in northern qinghai tibetan plateau. Earthquake Research Advances 2, 100140. doi:10.1016/j.eqrea.2022.100140.

Luo, Y., Ampuero, J.P., 2017. Stability of faults with heterogeneous friction properties and effective normal stress. Tectonophysics doi:10.1016/j.tecto.2017.11.006.

Luo, Y., Ampuero, J.P., 2018. Stability of faults with heterogeneous friction properties and effective normal stress. Tectonophysics 733, 257–272. doi:10.1016/j.tecto.2017.11.006.

Luo, Y., Ampuero, J.P., Galvez, P., Van Den Ende, M., Idini, B., 2017. Qdyn: a quasi-dynamic earthquake simulator (v1.1). URL: https://zenodo.org/record/322459, doi:10.5281/ZENODO.322459.

Ma, S., Andrews, D., 2010. Inelastic off-fault response and three-dimensional dynamics of earthquake rupture on a strike-slip fault. J. Geophys. Res. 115. doi:10.1029/2009JB006382.

Marone, C., 1998. Laboratory-derived friction laws and their application to seismic faulting. Ann. Rev. Earth Planet. Sci. 26, 643–696. doi:10.1146/annurev.earth.26.1.643.

Martínez-Garzón, P., Poli, P., 2024. Cascade and pre-slip models oversimplify the complexity of earthquake preparation in nature. Communications Earth & Environment 5. doi:10.1038/s43247-024-01285-y.

Massonnet, D., Feigl, K.L., 1998. Radar interferometry and its application to changes in the earth's surface. Rev. Geophys. 36, 441–500.

McGarr, A., 2014. Maximum magnitude earthquakes induced by fluid injection: Limits on fluid injection earthquakes. Journal of Geophysical Research: Solid Earth 119, 1008–1019. doi:10.1002/2013jb010597.

Michel, S., Avouac, J.P., Lapusta, N., Jiang, J., 2017. Pulse-like partial ruptures and high-frequency radiation at creeping-locked transition during megathrust earthquakes. Geophys. Res. Lett. doi:10.1002/2017GL074725.

Michel, S., Gualandi, A., Avouac, J.P., 2018. Interseismic coupling and slow slip events on the cascadia megathrust. Pure and Applied Geophysics 176, 3867–3891. doi:10.1007/s00024-018-1991-x.

Michel, S., Gualandi, A., Avouac, J.P., 2019. Similar scaling laws for earthquakes and cascadia slow-slip events. Nature 574, 522–526. doi:10.1038/s41586-019-1673-6.

Mitchell, T.M., Faulkner, D.R., 2008. Experimental measurements of permeability evolution during triaxial compression of initially intact crystalline rocks and implications for fluid flow in fault zones. J. Geophys. Res. 113. doi:10.1029/2008JB005588.

Mitchell, T.M., Faulkner, D.R., 2009. The nature and origin of off-fault damage surrounding strike-slip fault zones with a wide range of displacements: a field study from the Atacama fault system, northern Chile. J. Struct. Geol. 31, 802–816. doi:10.1016/j.jsg.2009.05.002.

Mitsui, N., Hirahara, K., 2006. Slow slip events controlled by the slab dip and its lateral change along a trench. Earth Planet. Sc. Lett. 245, 344–358. doi:10.1016/j.epsl.2006.03.001.

Mogilevskaya, S.G., 2014. Lost in translation: Crack problems in different languages. International Journal of Solids and Structures 51, 4492–4503. URL: http://dx.doi.org/10.1016/j.ijsolstr.2014.08.025, doi:10.1016/j.ijsolstr.2014.08.025.

Moore, J.D.P., Barbot, S., Feng, L., Hang, Y., Lambert, V., Lindsey, E., Masuti, S., Matsuzawa, T., Muto, J., Priyamvada Nanjundiah, Salman, R., Sharadha Sathiakumar, Sethi, H., 2019. jdpmoore/unicycle: Unicycle. URL: https://zenodo.org/record/5688288, doi:10.5281/ZENODO.5688288.

Murray, J., 2006. Slip on the san andreas fault at parkfield, california, over two earthquake cycles, and the implications for seismic hazard. Bulletin of the Seismological Society of America 96, S283–S303. URL: http://dx.doi.org/10.1785/0120050820, doi:10.1785/0120050820.

Muskhelishvili, N.I., et al., 1953. Some basic problems of the mathematical theory of elasticity. volume 15. Noordhoff Groningen.

Nagata, K., Nakatani, M., Yoshida, S., 2012. A revised rate- and state-dependent friction law obtained by constraining constitutive and evolution laws separately with laboratory data. Journal of Geophysical Research: Solid Earth 117. doi:10.1029/2011jb008818.

Nakata, R., Ando, R., Hori, T., Ide, S., 2011. Generation mechanism of slow earthquakes: Numerical analysis based on a dynamic model with brittle-ductile mixed fault heterogeneity. J. Geophys. Res. 116, B08308. doi:10.1029/2010JB008188.

Nakata, T., Shimazaki, K., Suzuki, Y., Tsukuda, E., 1998. Fault branching and directivity of rupture propagation (in japanese). J. Geogr. 107, 512–528.

Nakatani, M., 2001. Conceptual and physical clarification of rate and state friction: Frictional sliding as a thermally activated rheology. Journal of Geophysical Research: Solid Earth 106, 13347–13380. doi:10.1029/2000jb900453.

Nevitt, J.M., Brooks, B.A., Hardebeck, J.L., Aagaard, B.T., 2023. 2019 m7.1 ridgecrest earthquake slip distribution controlled by fault geometry inherited from independence dike swarm. Nature Communications 14. doi:10.1038/s41467-023-36840-2.

Nie, S., Barbot, S., 2021. Seismogenic and tremorgenic slow slip near the stability transition of frictional sliding. Earth and Planetary Science Letters 569, 117037. doi:10.1016/j.epsl.2021.117037.

Nikkhoo, M., Walter, T.R., 2015. Triangular dislocation: an analytical, artefact-free solution. Geophys. J. Int. 201, 1117–1139. doi:10.1093/gji/ggv035.

Obara, K., Hirose, H., Yamamizu, F., Kasahara, K., 2004. Episodic slow slip events accompanied by non-volcanic tremors in southwest japan subduction zone. Geophys. Res. Lett. 31. doi:10.1029/2004GL020848.

Obara, K., Kato, A., 2016. Connecting slow earthquakes to huge earthquakes. Science 353, 253–257. doi:10.1126/science.aaf1512.

Ogata, Y., 1988. Statistical models for earthquake occurrences and residual analysis for point processes. Journal of the American Statistical Association 83, 9–27. doi:10.1080/01621459.1988.10478560.

Ohtani, M., Hirahara, K., Takahashi, Y., Hori, T., Hyodo, M., Nakashima, H., Iwashita, T., 2011. Fast computation of quasi-dynamic earthquake cycle simulation with hierarchical matrices. Procedia Comput. Sci. 4, 1456–1465. doi:10.1016/j.procs.2011.04.158.

Okada, Y., 1992. Internal deformation due to shear and tensile faults in a half-space. Bull. Seismol. Soc. Am. 82, 1018.

Okubo, K., Bhat, H.S., Rougier, E., Marty, S., Schubnel, A., Lei, Z., Knight, E.E., Klinger, Y., 2019. Dynamics, radiation and overall energy budget of earthquake rupture with coseismic off-fault damage. J. Geophys. Res. 124. doi:10.1029/2019JB017304.

Olesiak, Z., Wnuk, M., 1968. Plastic energy dissipation due to a penny-shaped crack. International Journal of Fracture Mechanics 4, 383–396. doi:10.1007/bf00186804.

Omori, F., 1894. On after-shocks of earthquakes,. J. Coll. Sci. Imp. Univ. Tokyo 7, 111–200.

Ozawa, S., Ando, R., 2021. Mainshock and aftershock sequence simulation in geometrically complex fault zones. J. Geophys. Res. 126. doi:10.1029/2020jb020865.

Ozawa, S., Ando, R., Dunham, E.M., 2023. Quantifying the probability of rupture arrest at restraining and releasing bends using earthquake sequence simulations. Earth and Planetary Science Letters 617, 118276. doi:10.1016/j.epsl.2023.118276.

Ozawa, S., Ida, A., Hoshino, T., Ando, R., 2022. Large-scale earthquake sequence simulations on 3-d non-planar faults using the boundary element method accelerated by lattice h-matrices. Geophysical Journal International 232, 1471–1481. doi:10.1093/gji/ggac386.

Ozawa, S., Murakami, M., Tada, T., 2001. Time-dependent inversion study of the slow thrust event in the nankai trough subduction zone, southwestern japan. Journal of Geophysical Research: Solid Earth 106, 787–802. doi:10.1029/2000jb900317.

Palgunadi, K.H., Gabriel, A.A., Ulrich, T., López-Comino, J.Á., Mai, P.M., 2020. Dynamic fault interaction during a fluid-injection-induced earthquake: The 2017 mw 5.5 pohang event. Bulletin of the Seismological Society of America 110, 2328–2349. URL: http://dx.doi.org/10.1785/0120200106, doi:10.1785/0120200106.

Palmer, A.C., Rice, J.R., 1973. Growth of slip surfaces in progressive failure of over-consolidated clay. Proc. R. Soc. Lond. Ser-A 332, 527–548. doi:10.1098/rspa.1973.0040.

Passelègue, F.X., Almakari, M., Dublanchet, P., Barras, F., Fortin, J., Violay, M., 2020. Initial effective stress controls the nature of earthquakes. Nat. Commun. 11. URL: https://doi.org/10.1038/s41467-020-18937-0, doi:10.1038/s41467-020-18937-0.

Peng, Z., Gomberg, J., 2010. An integrated perspective of the continuum between earthquakes and slow-slip phenomena. Nature Geoscience 3, 599–607. doi:10.1038/ngeo940.

Perez-Silva, A., Li, D., Gabriel, A., Kaneko, Y., 2021. 3d modeling of long-term slow slip events along the flat-slab segment in the guerrero seismic gap, mexico. Geophysical Research Letters 48. doi:10.1029/2021gl092968.

Perfettini, H., Molinari, A., 2017. A micromechanical model of rate and state friction: 1. static and dynamic sliding. Journal of Geophysical Research: Solid Earth 122, 2590–2637. doi:10.1002/2016jb013302.

Plesch, A., Shaw, J.H., Benson, C., Bryant, W.A., Carena, S., Cooke, M., Dolan, J., Fuis, G., Gath, E., Grant, L., Hauksson, E., Jordan, T., Kamerling, M., Legg, M., Lindvall, S., Magistrale, H., Nicholson, C., Niemi, N., Oskin, M., Perry, S., Planansky, G., Rockwell, T., Shearer, P., Sorlien, C., Suss, M.P., Suppe, J., Treiman, J., Yeats, R., 2007. Community fault model (CFM) for southern california. Bulletin of the Seismological Society of America 97, 1793–1802. doi:10.1785/0120050211.

Quin, H., 1990. Dynamic stress drop and rupture dynamics of the october 15, 1979 imperial valley, california, earthquake. Tectonophysics 175, 93–117. doi:10.1016/0040-1951(90)90132-r.

Rabinowicz, E., 1958. The intrinsic variables affecting the stick-slip process. Proc. Phys. Soc. 71, 668.

Radiguet, M., Perfettini, H., Cotte, N., Gualandi, A., Valette, B., Kostoglodov, V., Lhomme, T., Walpersdorf, A., Cabral Cano, E., Campillo, M., 2016. Triggering of the 2014 mw7.3 papanoa earthquake by a slow slip event in guerrero, mexico. Nature Geoscience 9, 829–833. doi:10.1038/NGEO2817.

Ranjith, K., Rice, J.R., 1999. Stability of quasi-static slip in a single degree of freedom elastic system with rate and state dependent friction. J. Mech. Phys. Solids 47, 1207–1218.

Reid, H.F., 1910. The mechanics of earthquake, the california earthquake of april 18, 1906. Lawson Report , 16–18.

Rice, J.R., 1992. Fault stress states, pore pressure distributions, and the weakness of the san andreas fault, in: Evans, B., Wong, T.F. (Eds.), Fault Mechanics and Transport Properties in Rocks. Academic Press, pp. 475–503.

Rice, J.R., 1993. Spatio-temporal complexity of slip on a fault. J. Geophys. Res. 98, 9885–9907. doi:10.1029/93JB00191.

Rice, J.R., 2001. New perspectives on crack and fault dynamics, in: Aref, H., Phillips, J.W. (Eds.), Mechanics for a New Mellennium (Proceedings of the 20th International Congress of Theoretical and Applied Mechanics, 27 Aug - 2 Sept 2000, Chicago). Kluwer Academic Publishers, pp. 1–24.

Rice, J.R., 2006. Heating and weakening of faults during earthquake slip. J. Geophys. Res. 111. doi:10.1029/2005JB004006.

Rice, J.R., Ben-Zion, Y., 1996. Slip complexity in earthquake fault models. Proc. Natl. Acad. Sci. USA 93, 3811–3818.

Rice, J.R., Lapusta, N., Ranjith, K., 2001. Rate and state dependent friction and the stability of sliding between elastically deformable solids. J. Mech. Phys. Solids 49, 1865–1898.

Rogers, G., Dragert, H., 2003. Episodic tremor and slip on the Cascadia subduction zone: The chatter of silent slip. Science 300, 1942–1943.

Romanet, P., 2017. Fast algorithms to model quasi-dynamic earthquake cycles in complex fault networks. Ph.D. thesis. INSTITUT DE PHYSIQUE DU GLOBE DE PARIS.

Romanet, P., Bhat, H.S., Chaillat, S., Madariaga, R., 2021. Fast algorithms to model quasi-dynamic earthquake cycles in complex fault networks. to be subm. J. Geophys. Res. .

Romanet, P., Bhat, H.S., Jolivet, R., Madariaga, R., 2018. Fast and slow earthquakes emerge due to fault geometrical complexity. Geophys. Res. Lett. doi:10.1029/2018GL077579.

Romanowicz, B., Rundle, J.B., 1993. On scaling relations for large earthquakes. Bulletin of the Seismological Society of America 83, 1294–1297. doi:10.1785/bssa0830041294.

Ross, Z.E., Ben-Zion, Y., Zaliapin, I., 2022. Geometrical properties of seismicity in california. Geophysical Journal International 231, 493–504. doi:10.1093/gji/ggac189.

Ross, Z.E., Cochran, E.S., Trugman, D.T., Smith, J.D., 2020. 3d fault architecture controls the dynamism of earthquake swarms. Science 368, 1357–1361. doi:10.1126/science.abb0779.

Rousset, B., Bürgmann, R., Campillo, M., 2019. Slow slip events in the roots of the san andreas fault. Science Advances 5. doi:10.1126/sciadv.aav3274.

Rowe, C.D., Griffith, W.A., 2015. Do faults preserve a record of seismic slip: A second opinion. Journal of Structural Geology 78, 1–26. doi:10.1016/j.jsg.2015.06.006.

Rubin, A., Ampuero, J.P., 2005. Earthquake nucleation on (aging) rate and state faults. J. Geophys. Res. 110, B11312. doi:10.1029/2005JB003686.

Rubin, A.M., 2008. Episodic slow slip events and rate-and-state friction. J. Geophys. Res. 113, B11414. doi:10.1029/2008JB005642.

Rudnicki, J.W., 1986. Fluid mass sources and point forces in linear elastic diffusive solids. Mechanics of Materials 5, 383–393. URL: http://dx.doi.org/10.1016/0167-6636(86)90042-6, doi:10.1016/0167-6636(86)90042-6.

Ruina, A., 1983. Slip instability and state variable friction laws. J. Geophys. Res. 88, 359–370. doi:10.1029/JB088iB12p10359.

Sáez, A., 2023. Three-dimensional fluid-driven frictional ruptures: theory and applications. Ph.D. thesis. EPFL.

Sáez, A., Lecampion, B., 2024. Fluid-driven slow slip and earthquake nucleation on a slip-weakening circular fault. Journal of the Mechanics and Physics of Solids 183, 105506. URL: http://dx.doi.org/10.1016/j.jmps.2023.105506, doi:10.1016/j.jmps.2023.105506.

Scheel, J., Wallenta, D., Ricoeur, A., 2021. A critical review on the complex potentials in linear elastic fracture mechanics. J. Elasticity 147, 291–308. doi:10.1007/s10659-021-09873-1.

Schmitt, S., Segall, P., Matsuzawa, T., 2011. Shear heating-induced thermal pressurization during earthquake nucleation. J. Geophys. Res. 116. doi:10.1029/2010JB008035.

Scholz, C.H., 1998. Earthquakes and friction laws. Nature 391, 37–42. doi:10.1038/34097.

Scholz, C.H., 2002. The mechanics of earthquakes and faulting. Cambridge Univ Press.

Scholz, C.H., 2019. The mechanics of earthquakes and faulting. Cambridge Univ Press. doi:10.1017/9781316681473.

Scuderi, M.M., Collettini, C., 2016. The role of fluid pressure in induced vs. triggered seismicity: insights from rock deformation experiments on carbonates. Scientific Reports 6. doi:10.1038/srep24852.

Seebeck, H., Dissen, R.V., Litchfield, N., Barnes, P.M., Nicol, A., Langridge, R., Barrell, D.J.A., Villamor, P., Ellis, S., Rattenbury, M., Bannister, S., Gerstenberger, M., Ghisetti, F., Sutherland, R., Hirschberg, H., Fraser, J., Nodder, S.D., Stirling, M., Humphrey, J., Bland, K.J., Howell, A., Mountjoy, J., Moon, V., Stahl, T., Spinardi, F., Townsend, D., Clark, K., Hamling, I., Cox, S., de Lange, W., Wopereis, P., Johnston, M., Morgenstern, R., Coffey, G., Eccles, J.D., Little, T., Fry, B., Griffin, J., Townend, J., Mortimer, N., Alcaraz, S., Massiot, C., Rowland, J.V., Muirhead, J., Upton, P., Lee, J., 2023. The new zealand community fault model – version 1.0: an improved geological foundation for seismic hazard modelling. New Zealand Journal of Geology and Geophysics , 1–21doi:10.1080/00288306.2023.2181362.

Segall, P., 2010. Earthquake and volcano deformation. Princeton University Press.

Segall, P., Lu, S., 2015. Injection-induced seismicity: Poroelastic and earthquake nucleation effects. J. Geophys. Res. 120, 5082–5103. doi:10.1002/2015jb012060.

Segall, P., Pollard, D.D., 1980. Mechanics of discontinuous faults. J. Geophys. Res. 85, 4337–4350. doi:10.1029/JB085iB08p04337.

Segall, P., Rice, J.R., 1995. Dilatancy, compaction, and slip instability of a fluid-infiltrated fault. J. Geophys. Res. 100, 22155–22171.

Segall, P., Rubin, A.M., Bradley, A.M., Rice, J.R., 2010. Dilatant strengthening as a mechanism for slow slip events. J. Geophys. Res. 115, B12305. doi:10.1029/2010JB007449,.

Segedin, C.M., 1951. Note on a penny-shaped crack under shear. Mathematical Proceedings of the Cambridge Philosophical Society 47, 396–400. doi:10.1017/s0305004100026736.

Shapiro, S.A., Krüger, O.S., Dinske, C., Langenbruch, C., 2011. Magnitudes of induced earthquakes and geometric scales of fluid-stimulated rock volumes. GEOPHYSICS 76, WC55–WC63. doi:10.1190/geo2010-0349.1.

Shelly, D.R., 2009. Possible deep fault slip preceding the 2004 parkfield earthquake, inferred from detailed observations of tectonic tremor. Geophysical Research Letters 36. doi:10.1029/2009gl039589.

Shelly, D.R., Beroza, G.C., Ide, S., 2007. Non-volcanic tremor and low-frequency earthquake swarms. Nature 446, 305–307. doi:10.1038/nature05666.

Shelly, D.R., Beroza, G.C., Ide, S., Nakamula, S., 2006. Low-frequency earthquakes in Shikoku, Japan, and their relationship to episodic tremor and slip. Nature 442, 188–191. doi:10.1038/nature04931.

Shibazaki, B., Shimamoto, T., 2007. Modelling of short-interval silent slip events in deeper subduction interfaces considering the frictional properties at the unstable–stable transition regime. Geophys. J. Int. 171, 191–205. doi:10.1111/j.1365-246X.2007.03434.x.

Sieh, K., Jones, L., Hauksson, E., Hudnut, K., Eberhart-Phillips, D., Heaton, T., Hough, S., Hutton, K., Kanamori, H., Lilje, A., Lindvall, S., McGill, S.F., Mori, J., Rubin, C., Spotila, J.A., Stock, J., Thio, H.K., Treiman, J., Wernicke, B., Zachariasen, J., 1993. Near-field investigations of the landers earthquake sequence, april to july 1992. Science 260, 171–176.

Skarbek, R., Rempel, A., Schmidt, D., 2012. Geologic heterogeneity can produce aseismic slip transients. Geophys. Res. Lett. 39. doi:10.1029/2012GL053762.

Sneddon, I.N., 1946. The distribution of stress in the neighbourhood of a crack in an elastic solid. Proc. R. Soc. Lond. Ser-A 187, 229–260.

Sowers, J.M., Unruh, J.R., Lettis, W.R., Rubin, T.D., 1994. Relationship of the Kickapoo fault to the Johnson Valley and Homestead Valley faults, San Bernardino county, California. Bull. Seism. Soc. Am. 84, 528–536.

Tada, T., Yamashita, T., 1997. Non-hypersingular boundary integral equations for two dimensional non-planar crack analysis. Geophys. J. Int. 130, 269–282.

Taufiqurrahman, T., Gabriel, A.A., Li, D., Ulrich, T., Li, B., Carena, S., Verdecchia, A., Gallovič, F., 2023. Dynamics, interactions and delays of the 2019 ridgecrest rupture sequence. Nature 618, 308–315. URL: http://dx.doi.org/10.1038/s41586-023-05985-x, doi:10.1038/s41586-023-05985-x.

Thomas, M.Y., Avouac, J., Lapusta, N., 2017. Rate-and-state friction properties of the longitudinal valley fault from kinematic and dynamic modeling of seismic and aseismic slip. Journal of Geophysical Research: Solid Earth 122, 3115–3137. doi:10.1002/2016jb013615.

Thomas, M.Y., Lapusta, N., Noda, H., Avouac, J.P., 2014. Quasi-dynamic versus fully dynamic simulations of earthquakes and aseismic slip with and without enhanced coseismic weakening. J. Geophys. Res. 119, 1986–2004. doi:10.1002/2013JB010615.

Thompson, T., Meade, B., 2019. Boundary element methods for earthquake modeling with realistic 3d geometries. arXiv doi:10.31223/osf.io/xzhuk.

Tse, S.T., Rice, J.R., 1986. Crustal earthquake instability in relation to the depth variation of frictional slip properties. J. Geophys. Res. 91, 9452–9472. doi:10.1029/JB091iB09p09452.

Tymofyeyeva, E., Fialko, Y., Jiang, J., Xu, X., Sandwell, D., Bilham, R., Rockwell, T.K., Blanton, C., Burkett, F., Gontz, A., Moafipoor, S., 2019. Slow slip event on the southern san andreas fault triggered by the 2017 mw8.2 chiapas (mexico) earthquake. Journal of Geophysical Research: Solid Earth 124, 9956–9975. doi:10.1029/2018jb016765.

Uchida, N., 2019. Detection of repeating earthquakes and their application in characterizing slow fault slip. Progress in Earth and Planetary Science 6. doi:10.1186/s40645-019-0284-z.

Uphoff, C., May, D.A., Gabriel, A.A., 2022. A discontinuous galerkin method for sequences of earthquakes and aseismic slip on multiple faults using unstructured curvilinear grids. Geophysical Journal International 233, 586–626. doi:10.1093/gji/ggac467.

Utsu, T., Ogata, Y., Matsu'ura, R.S., 1995. The centenary of the omori formula for a decay law of aftershock activity. J. Phys. Earth 43, 1–33.

Vallage, A., Klinger, Y., Grandin, R., Bhat, H.S., Pierrot-Deseilligny, M., 2015. Inelastic surface deformation during the 2013 mw 7.7 balochistan, pakistan, earthquake. Geology 43, 1079–1082. doi:10.1130/G37290.1.

Veedu, D.M., Barbot, S., 2016. The parkfield tremors reveal slow and fast ruptures on the same asperity. Nature 532, 361–365. doi:10.1038/nature17190.

Viesca, R.C., 2016. Self-similar slip instability on interfaces with rate- and state-dependent friction. Proc. R. Soc. A doi:10.1098/rspa.2016.0254.

Wallace, L.M., Eberhart-Phillips, D., 2013. Newly observed, deep slow slip events at the central hikurangi margin, new zealand: Implications for downdip variability of slow slip and tremor, and relationship to seismic structure. Geophys. Res. Lett. 40, 5393–5398. doi:10.1002/2013GL057682.

Wallace, L.M., Hreinsdóttir, S., Ellis, S., Hamling, I., D'Anastasio, E., Denys, P., 2018. Triggered slow slip and afterslip on the southern hikurangi subduction zone following the kaikōura earthquake. Geophysical Research Letters 45, 4710–4718. doi:10.1002/2018gl077385.

Wallace, L.M., Webb, S.C., Ito, Y., Mochizuki, K., Hino, R., Henrys, S., Schwartz, S.Y., Sheehan, A.F., 2016. Slow slip near the trench at the hikurangi subduction zone, new zealand. Science 352, 701–704.

Wang, L., Barbot, S., 2020. Excitation of san andreas tremors by thermal instabilities below the seismogenic zone. Science Advances 6. doi:10.1126/sciadv.abb2057.

Wei, S., Avouac, J.P., Hudnut, K.W., Donnellan, A., Parker, J.W., Graves, R.W., Helmberger, D., Fielding, E., Liu, Z., Cappa, F., Eneva, M., 2015. The 2012 brawley swarm triggered by injection-induced aseismic slip. Earth and Planetary Science Letters 422, 115–125. doi:10.1016/j.epsl.2015.03.054.

Wesnousky, S.G., 2006. Predicting the endpoints of earthquake ruptures. Nature 444, 358–360.

Wibberley, C.A., Yielding, G., Di Toro, G., 2008. Recent advances in the understanding of fault zone internal structure: a review. Geol. Soc. Spec. Publ. 299, 5–33. doi:10.1144/SP299.2.

Wilkinson, M., McCaffrey, K.J.W., Roberts, G., Cowie, P.A., Phillips, R.J., Michetti, A.M., Vittori, E., Guerrieri, L., Blumetti, A.M., Bubeck, A., Yates, A., Sileo, G.,

2010. Partitioned postseismic deformation associated with the 2009 mw 6.3 l'aquila earthquake surface rupture measured using a terrestrial laser scanner. Geophysical Research Letters 37. doi:10.1029/2010gl043099.

Winkler, J.R., 1993. Numerical recipes in c: The art of scientific computing, second edition. Endeavour 17, 201. doi:10.1016/0160-9327(93)90069-f.

Wu, Y., Chen, X., 2014. The scale-dependent slip pattern for a uniform fault model obeying the rate- and state-dependent friction law. Journal of Geophysical Research: Solid Earth 119, 4890–4906. doi:10.1002/2013jb010779.

Xu, X., Chen, W., Ma, W., Yu, G., Chen, G., 2002. Surface rupture of the kunlunshan earthquake (m_s 8.1), northern tibetan plateau, china. Seismol. Res. Lett. 73, 884–892. doi:10.1785/gssrl.73.6.884.

Yalamanchili, P., Arshad, U., Mohammed, Z., Garigipati, P., Entschev, P., Kloppenborg, B., Malcolm, J., Melonakos, J., 2015. ArrayFire - A high performance software library for parallel computing with an easy-to-use API. URL: https://github.com/arrayfire/arrayfire.

Ye, Z., Ghassemi, A., 2018. Injection-induced shear slip and permeability enhancement in granite fractures. J. Geophys. Res. Solid Earth 123, 9009–9032.

Zhang, H., Chen, X., 2006. Dynamic rupture on a planar fault in three-dimensional half space - i. theory. Geophysical Journal International 164, 633–652. doi:10.1111/j.1365-246x.2006.02887.x.

RÉSUMÉ

Les systèmes de failles majeures présentent des propriétés géométriques complexes, telles que des directions de glissement variées, des discontinuités et des variations en profondeur. Ces géométries, reconstruites à travers des méthodes géologiques et géophysiques, influencent significativement les événements sismiques. Les failles non planes introduisent une hétérogénéité de contrainte, influençant la taille des séismes et le comportement de rupture. Les sauts de rupture à travers les relais de failles peuvent augmenter la taille des séismes, augmentant ainsi les risques et les dommages potentiels.

Nous présentons un modèle tridimensionnel quasi-dynamique du cycle sismique utilisant la méthode des éléments de frontière, accéléré par des matrices hiérarchiques. Cette approche capture les interactions élastiques entre plusieurs segments de failles et les champs de contrainte hétérogènes, réduisant la complexité de calcul de $O(N^2)$ à $O(N \log N)$. Validé contre des solutions analytiques et des benchmarks numériques, notre modèle traite des configurations telles que deux failles planes parallèles. Les interactions entre les failles créent des événements de glissement complexes, y compris des événements de glissement lent et des ruptures partielles ou complètes. En incorporant les interactions 3D, notre modèle supporte une gamme plus large de paramètres pour la coexistence des séismes et des événements de glissement lent comparé aux modèles 2D. Nos résultats suggèrent que les divergences de mise à l'échelle moment-durée dans les événements de glissement lent dépendent du seuil de taux de glissement utilisé.

Appliqué aux séismes de Kahramanmaraş en Turquie en 2023, notre modèle, avec une géométrie de faille réaliste et des champs de contrainte lissés, reproduit avec succès la rupture bilatérale observée sur la faille anatolienne orientale et le déclenchement retardé sur la faille de Cardak.

MOTS CLÉS

Matrice hiérarchique, Géométrie des failles 3D, Cycle sismique

ABSTRACT

Major fault systems exhibit complex geometrical properties such as varying strike directions, discontinuities, and depth variations. These geometries, reconstructed through geological and geophysical methods, significantly impact seismic events. Nonplanar faults introduce stress heterogeneity, influencing earthquake size and rupture behavior. Rupture jumps across fault step-overs can increase earthquake size, heightening risk and damage potential.

We introduce a 3D quasi-dynamic earthquake cycle model using the boundary element method, accelerated by Hierarchical matrices. This approach captures elastic interactions among multiple fault segments and heterogeneous stress fields, reducing computational complexity from $O(N^2)$ to $O(N \log N)$.

Validated against analytical solutions and numerical benchmarks, our model handles configurations such as two parallel planar faults. Interactions between faults create complex slip events, including slow slip events and partial or full ruptures. By incorporating 3D interactions, our model supports a broader range of parameters for coexisting earthquakes and slow slip events compared to 2D models. Our findings suggest that moment-duration scaling discrepancies in slow slip events depend on the slip rate threshold used.

Applied to the 2023 Kahramanmaraş earthquakes in Turkey, our model, with realistic fault geometry and smoothed stress fields, successfully reproduces the observed bilateral rupture on the Eastern Anatolian Fault and delayed triggering on the Cardak fault.

KEYWORDS

Hierarchical Matrices, 3D fault geometries, Earthquake cycle